Photonic techniques for indoor spatially-multiplexed wireless communication

Photonic techniques for indoor spatially-multiplexed wireless communication

THESIS

ter verkrijging van de graad van doctor aan de Technische Universiteit Eindhoven, op gezag van de rector magnificus prof.dr.ir. F.P.T. Baaijens, voor een commissie aangewezen door het College voor Promoties, in het openbaar te verdedigen op vrijdag 25 maart 2022 om 13:30 uur

door

Jianou Huang

geboren te Yuxi, China

Dit proefschrift is goedgekeurd door de promotoren en de samenstelling van de promotiecommissie is als volgt:

Voorzitter:	prof.dr.ir. M. Bentum
Promotor:	prof.ir. A.M.J. Koonen
Co-promotor:	dr.ir. Z. Cao
Leden:	prof.dr. H. Liu (University College London)
	prof.dr. O. Hess (Imperial College London)
	prof.dr.ir. P.G.M. Baltus
	dr. J.J.G.M. van der Tol
	dr. A. González Curto

Het onderzoek of ontwerp dat in dit thesis wordt beschreven is uitgevoerd in overeenstemming met de TU/e Gedragscode Wetenschapsbeoefening.

A catalogue record is available from the Eindhoven University of Technology Library

ISBN: 978-90-386-5476-8
NUR: 959
Title: Photonic techniques for indoor spatially-multiplexed wireless communication
Author: Jianou Huang
Eindhoven University of Technology, 2022.

Keywords: Fiber-wireless indoor network / Wireless communication / Spatial multiplexing / Beam steering / Orbital angular momentum / Metasurface / Mode-locked laser

Typeset using LaTeX, printed in The Netherlands.

Wish us Fun Young.

Abstract

In response to the exponentially increasing data traffic volumes from emerging data-rate-hungry wireless applications and growing number of wireless devices, the delivery of wireless services is evolving along two main paths of the physical layer: seeking more bandwidth and exploiting advanced spatial multiplexing, which is a multiplexing technique used to transmit independent channels separated in space, providing a new multiplexing dimension in addition to other widely used multiplexing techniques such as frequency-division multiplexing, time-division multiplexing, and code-division multiplexing. The former path leads to millimeter-wave (mmWave) communications in fifth-generation (5G and beyond) cellular and wireless fidelity (Wi-Fi) networks, and to optical wireless communication (OWC) techniques. The latter path leads to advanced wireless spatial multiplexing access techniques such as optical beam steering in OWC systems; and multiple-input multiple-output (MIMO), massive MIMO, and radio frequency (RF) beam steering in 5G cellular and Wi-Fi networks, and also leads to spatial multiplexing at the system architecture level, such as densely deployed 5G small cells and Wi-Fi hot spots. Moreover, orbital angular momentum (OAM) as a new spatial multiplexing degree of freedom is considered one of the enablers of next-generation wireless networks. These two paths enhance each other from the following aspects: 1) the short wavelength of mmWave enables compact antenna size, greatly increasing the number of antennas in an access point, which makes massive MIMO, beam steering, and OAM modes multiplexing feasible. 2) The weak penetration of mmWave and light enhances the dense deployment of small cells.

Because a major portion (nearly 80%) of wireless data traffic volume is gen-

erated indoors, more and more access points of 5G cellular, Wi-Fi, and OWC networks will be densely deployed in indoor scenarios. These trends are asking for a converged wired-wireless indoor network compatible with all the wireless services and techniques to increase cost efficiency, energy efficiency, and system scalability while reducing system complexity. Such a network has been developed with the excellent works of the Electro-Optical Communication Group of Eindhoven University of Technology, which is characterized by: 1) Optical fiber is used as the network medium to connect all the access points of different wireless networks into a converged network. 2) RF access in this optical fiber network is provided by the revolutionary radio-over-fiber (RoF) technology. 3) All the signal processing is performed in the residential gateway centrally. In this converged fiber-wireless indoor network, all signals are modulated onto optical carriers and transmitted to access points through the optical fiber. Therefore, to realize the network, high-performance optoelectronic devices for the RoF system and photonic techniques for spatial multiplexing as key enablers are essential.

My research has been exploring high-efficiency, low-cost photonic techniques to enhance the RoF system and the spatial multiplexing in the converged fiber-wireless indoor network to boost the network capacity and user density further. Optical frequency comb source for indoor RoF systems, optical beam steering techniques for OWC systems, and OAM modes multiplexing/demultiplexing techniques for both RF and OWC systems have been explored in this thesis:

- **Low-cost high-performance optical frequency comb source for indoor RoF system**

  Low-cost broad-bandwidth optoelectronic devices with excellent linearity and low phase noise are key enablers for the RoF system of the converged fiber-wireless indoor network. Among them, the optical frequency comb source is a key element because it plays an important role in both RF carrier generation and phase-coherent dense wavelength-division multiplexing (DWDM). Therefore, we developed an O-band frequency comb source based on a passively mode-locked InAs quantum dot laser that has achieved an ultra-stable repetition rate of 25.5 GHz with 0.07 GHz deviation (corresponding to mode spacing between adjacent tones in the frequency domain) over the widest temperature range (from 20°C to 120°C) yet reported for any type of mode-locked laser. These achievements are enabled by the high dot density and engineered quantized energy difference between the ground state and the first excited state, which is realized by the optimized self-assembled InAs quantum dot growth method. The fabricated device shows a relatively broad -6 dB coherent comb bandwidth of 4.81 nm at 100°C with a low average relative intensity noise of less than -146 dBc/Hz, offering a maximum of 31 optical channels. The findings pave the way for utilizing ultra-stable, easy-operating, uncooled quantum dot mode-locked lasers as efficient frequency comb sources for broad-bandwidth, large-scale, low-cost phase-coherent DWDM multi-channel indoor RoF systems.

- **Photonics techniques for spatial multiplexing in the converged fiber-wireless indoor network**

  - **Photonics techniques for RF-OAM modes generation/detection**

    A novel electrically-controlled optical broadband phase shifter (ECO-BPS) for circular antenna array (CAA)-based RF-OAM modes generation and detection is proposed. The fabricated device is measured to provide 0-2π constant phase shifts with a low phase deviation of 3.44° over a broad frequency band from 12 GHz to 20 GHz. 17 equally spaced phase shifts covering 2π are generated by applying 16 direct-current levels to the ECO-BPS (the 17^{th} phase shift is synthesized by fitting the measured data to avoid the phase jump in the measurement when the phases are close to π or -π). With the obtained 17 phase shifts and a 17-element CAA, the generation/detection of 16 RF-OAM modes (up to ±8) can be supported. By using the 17-element CAA and a novel Dammann vortex grating-based crosstalk investigation method, the performance of the ECO-BPS is carefully analyzed, including the crosstalk at the demultiplexer side between the OAM channels. Here, Dammann vortex grating is chosen because it is capable of encoding orbital angular momentum topological charges in its diffraction orders with high energy efficiency, which can be used to simultaneously multiplex/demultiplex massive orbital angular momentum modes with independent modulation. Besides, as a 0-π binary-phase grating, Dammann vortex grating is easy to fabricate, making it more practical. Through comprehensive numerical analysis as well as experimental broadband demonstration from 12 to 20 GHz, it is convincingly shown that RF-OAM modes can be readily generated and transmitted with high purity and little crosstalk by using the proposed ECO-BPS.

- **Photonics techniques for optical beam steering**

  A novel small-phase-gradient (45°) gap-surface plasmon metasurface-based polarization beam splitter is designed, fabricated, and measured for performing polarization-controlled optical beam steering in C-band. The fabricated polarization beam splitter has high energy efficiency (>80% for normal incidence and >50% for incident polar angles of up to 35°). The measured overall polarization isolation is around 15 dB for all the incident directions. Enabled by the proposed metasurface polarization beam splitter, a centrally wavelength-polarization-controlled two-dimensional (2D) beam steering system with full-area coverage capability is proposed. In the system example, a large coverage area of 1.2×2.9 m^2 with room height 2.4488 m (equivalent with a 2D beam-steering angle range of $\pm 13.8° \times 49.8°$) is achieved with fewer arrayed waveguide grating router ports and a smaller wavelength tuning range (only C-band). The proposed system keeps high scalability to support multiple beams, flexibility to steer the beam, high optical efficiency, simple and cheap devices on remote sides, and centralized control to lower maintenance costs. Finally, a 1.2-m 20-Gbps beam-steered infrared wireless link is demonstrated as a proof-of-concept.

- **Photonics techniques for optical OAM modes multiplexing/demultiplexing**

  In addition to OAM for RF systems, optical OAM modes multiplexing/demultiplexing technique for OWC systems is also explored. Dammann vortex grating-based optical OAM modes multiplexing/demultiplexing techniques show a practical path toward an OWC capacity of Pbps level due to their capabilities of simultaneously multiplexing/demultiplexing massive OAM beams with independent modulation. Here, by combining the Dammann vortex grating approach and the metasurface techniques developed previously, a metasurface-based 1×2 Dammann vortex grating, which has an intrinsic topological charge of +3, is designed, fabricated, and measured for optical $l = \pm 3$ OAM modes multiplexing/demultiplexing. The 0-π binary-phase Dammann vortex grating is realized by filling the desired grating phase patterns with the designed sub-wavelength metasurface 0 and π phase units. Such pixel-filling method can also be used to easily realize Dammann vortex gratings for multiplexing/demultiplexing other OAM modes, bringing advantages of flexibility, stability, and low cost (one set of phase units and fabrication process for different Dammann vortex gratings). The fabricated grating is demonstrated to have high efficiency (about 60%), broadband operation (C-band), and a large incident angle range (at least 25°). Besides, clear intensity profiles and interference patterns of $l = \pm 3$ OAM modes are observed over the broad bandwidth at a large incident range of 25°. Therefore, the feasibility of the fabricated device for optical $l = \pm 3$ OAM modes multiplexing/demultiplexing is demonstrated. With the fabricated grating, a 0.2-m 40-Gbps OAM beam transmission experiment is performed successfully. The obtained results demonstrate metasurface as a highly efficient, flexible, and low-cost approach for Dammann vortex grating implementation, providing a new powerful device for Dammann vortex grating-based optical OAM modes multiplexing/demultiplexing.

Contents

Chapter 1

Introduction

In this chapter, first the future indoor wireless network architecture is depicted, which should support the evolution of wireless communication services. Then, the key research points are outlined. Following these points are summaries of the proposed solutions, which are the main topics of this thesis.

1.1 Evolution of wireless communication services

1.1.1 Emerging wireless applications and their requirements

Since James Clerk Maxwell theoretically proved the existence of electromagnetic (EM) waves in 1864 and Heinrich Hertz experimentally verified the theory of Maxwell in 1887, the world has been connected by EM waves. Wireless communication has penetrated into everyone's daily life and has become an indispensable infrastructure in today's society. The wireless applications and transmission capacity today have increased tremendously compared with the first radio communication performed by Guglielmo Marconi in 1895. The message "s" sent across the Atlantic and received by Marconi has evolved into high-speed data streams of video, voice, and so on today. If one looks back on the development of wireless communication technology in the past few decades, it can be found that wireless technology is going through a revolutionary enhancement about every ten years, which is driven by the continuously growing capacity demands coming from the emerging wireless applications. Therefore, emerging wireless applications as the core drivers will be discussed in this section in order to outline the direction of wireless communication evolution.

Based on users, emerging wireless applications can be categorized into mobile internet and internet of things (IoT) [1]. Mobile Internet contains people-oriented wireless applications, including but not limited to: ultra-high-definition (UHD) video services (4k video and even 8k three-dimensional video), augmented reality, virtual reality (VR), large file sharing, online gaming, mobile/desktop cloud, self-media broadcasting, and smart office. These immersive wireless services provide people with unprecedented user experiences and will positively impact the way we live and work. On the other hand, IoT focuses on wireless communication between things and between things and people. It is a vast matrix of numerous non-standard devices and endpoints connected wirelessly over the internet. Those IoT devices are capable of collecting information, generating and transmitting real-time data from each point of the network. The data can be monitored, managed, and analyzed to achieve desired business or private outcomes. Therefore, IoT is considered the smart infrastructure of the future society, offering numerous advantages bringing significant cost savings and efficiencies in various applications, including but not limited to: critical infrastructure monitoring, environmental monitoring, smart cities, smart transportation, smart home, smart wearables, industrial control, automotive driving, and eHealth services.

The many wireless applications discussed above have different characteristics and requirements, and they can be grouped into three usage scenarios [2] based on their characteristics:

- Enhanced mobile broadband (eMBB): eMBB is the evolution of mobile broadband which addresses human-centric multi-media applications. Due to the emergence of new applications such as augmented reality, virtual reality, and UHD videos, much improved performance and an increasingly seamless user experience are demanded. In eMBB, a much higher user data rate and traffic capacity are needed for the hotspot case (for example, watching UHD videos), where the user density is high while the mobility requirement is low. As for the wide-area coverage case (augmented reality applications, for example), medium to high mobility and seamless coverage are needed, and a higher user data rate compared to the existing one is also desired.

- Ultra-reliable and low latency communications (URLLC): This use scenario has stringent requirements for reliability, latency and availability. Typical examples include industrial control, automotive driving, vehicle-

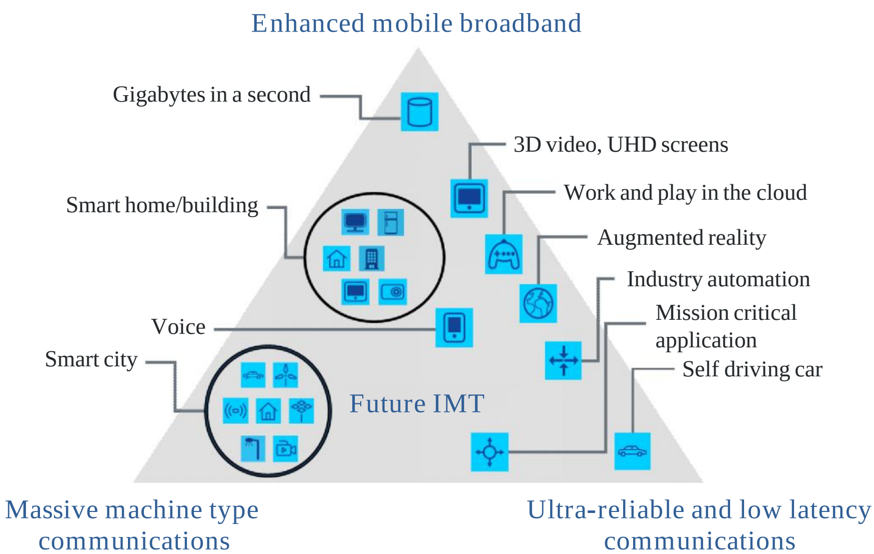

Figure 1.1: Usage scenarios of IMT for 2020 and beyond [2].

to-everything, remote medical surgery, patient monitoring, transportation safety, critical infrastructure monitoring, etc.

- Massive machine type communications (mMTC): This family of applications is characterized by a very large number of connected devices with a relatively low volume of non-delay-sensitive data. Devices are required to be low cost, and have a very long battery life (or even self-powering).

Some application examples of the above three usage scenarios are shown in Figure 1.1. These emerging wireless applications will bring people into an everything-connected society in the near future. As a result, a tremendous amount of growth in data traffic, connected devices, and data rate will occur. The following development trends can be foreseen:

- A huge increase in data traffic and data rate: The data-rate-hungry applications such as UHD video and VR require a data rate of more than 1 Gbps, bringing explosive growth in data traffic. The global data traffic is predicted to be 3 Zetabyte (10^{21} Byte)/year by 2030 [3], which is 10 times as much as in 2020.

- A huge increase in the number of connected devices: With the rapid increase in the number of smart terminals such as smartphones, laptops, tablets, smartwatches, VR glasses, etc., and IoT devices such as smart appliances, smart industrial robots, etc., the number of connected devices around the world is predicted to reach 100 billion by 2025 [4].

- A huge increase in the demands on energy efficiency: With the greatly increased data traffic and the number of connected devices, the energy consumption of future wireless networks should not be larger than networks today. Therefore, the energy efficiency is desired to be 100× enhanced [2].

Taking into account the trends above, International Mobile Telecommunications (IMT) approved the minimum technical performance requirements for the next generation mobile communication [5], as listed in Table 1.1.

Table 1.1: Minimum technical performance requirements of IMT 2020 [5, 6]

KPI	**Key Use Case**	**Values**
Peak Data Rate	eMBB	DL: 20 Gbps, UL: 10 Gbps
User Experienced Data Rate	eMBB	DL: 100 Mbps, UL: 50 Mbps (Dense Urban)
Peak Spectral Efficiency	eMBB	DL: 30 bps/Hz, UL: 15 bps/Hz
5% User Spectral Efficiency	eMBB	DL: 0.3 bps/Hz, UL: 0.21 bps/Hz (Indoor Hotspot) DL: 0.225 bps/Hz, UL: 0.15 bps/Hz (Dense Urban) DL: 0.12 bps/Hz, UL: 0.045 bps/Hz (Rural)
Average Spectral Efficiency	eMBB	DL: 9 bps/Hz/TRxP, UL: 6.75 bps/Hz/TRxP (Indoor Hotspot) DL: 7.8 bps/Hz/TRxP, UL: 5.4 bps/Hz/TRxP (Dense Urban) DL: 3.3 bps/Hz/TRxP, UL: 1.6 bps/Hz/TRxP (Rural)
Area Traffic Capacity	eMBB	DL: 10 Mbps/m^2 (Indoor Hotspot)
User Plane Latency	eMBB, URLLC	4 ms for eMBB and 1 ms for URLLC
Control Plane Latency	eMBB, URLLC	20 ms for eMBB and URLLC
Connection Density	mMTC	1,000,000 devices/km^2
Energy Efficiency	eMBB	Capability to support high sleep ratio and long sleep duration to enble low energy consumption when there is no data

Table 1.1 continued from previous page

KPI	Key Use Case	Values
Reliability	URLLC	1-10^{-5} success probability of transmitting a layer 2 protocol data unit of 32 bytes within 1 ms in channel quality of coverage edge
Mobility	mMBB	Up to 500 km/h
Mobility Interruption Time	mMBB, URLLC	0 ms
Bandwidth	eMBB	At least 100 MHz; Up to 1 GHz for operation in higher frequency bands (e.g., above 6 GHz)

1.1.2 Evelotion of mobile cellular networks

In response to the requirements discussed in the previous section, the fifth-generation (5G) mobile cellular network is fast emerging and initially deployed today. A brief comparison of mobiles generations is shown in Table 1.2. Two main evolution paths can be noticed: access technology and bandwidth. Here, we highlight these two core aspects that distinguish 5G from previous generations of mobile networks (from 1G to 4G):

- **Seeking more bandwidth**. According to Shannon's Theorem, The most direct way to increase capacity is to increase channel bandwidth. Therefore, seeking more bandwidth in the already overcrowded communication spectrum is one of the most important issues to meet the large capacity requirements of 5G. The frequency bands of 5G include the bands below 6 GHz and above. The bands below 6 GHz consist of the re-farmed 2G/3G spectrum, the identified spectrum for IMT, and the new frequency bands after WRC-15 [7]. These bands have the available bandwidth of up to several hundred MHz, and they are mainly applied to guarantee wide-area coverage and outdoor-to-indoor coverage. However, because of the scarcity and the limited bandwidth, seeking spectrums above 6 GHz is needed. Millimeter-wave (mmWave) is widely considered because its GHz-level bandwidth guarantees the desired ultra-high data rates [8]. Many mmWave frequency bands were studied for mobile communications, especially at 27.0-29.5 GHz, 38.0-39.5 GHz, 60 GHz, and E-Band (71-76 GHz/81-86 GHz) [9–12]. It is obvious that mmWave communication as an enabling technology of 5G has attracted a lot of attention around the world. Because the propagation loss of mmWave is large, mmWave communication is more suitable for short-reach scenarios with dense user and high data rate requirements, such as indoor hotspots.

- **Applying advanced spatial division multiple access (SDMA)**. Access technologies of mobile cellular networks are typically characterized by multiple access schemes, such as frequency division multiple access (FDMA), time division multiple access (TDMA), code division multiple access (CDMA), and orthogonal frequency division multiple access (OFDMA) used in pioneering generations of mobile cellular networks (1G to 4G). For 5G, in order to meet the demands of significantly increased mobile traffic, high energy efficiency, and high-density connection, advanced spatial multiplexing techniques are introduced to exploit the spatial domain. SDMA is enabled by multi-beam smart antenna arrays, with which signals can be received and sent directionally, following the directional nature of multipath. In SDMA systems, spatially separated users connected to the same base station are allowed to use the same time, frequency, and code resources [13]. SDMA provides extra degrees of freedom; therefore, the system capacity can be significantly increased. Moreover, the coverage and the energy efficiency can also be improved due to directional transmission/reception. An advanced FDMA technique is beam steering/forming, based on which a novel access method for 5G is developed known as beam division multiple access (BDMA) [14]. In the BDMA technique, by using a phased antenna array, the base station generates three-dimensionally divided antenna beams according to the location of mobile stations, then allocates a separate beam to each mobile station to give multiple accesses to the mobile stations. Another advanced SDMA technique is massive multiple-input multiple-output (MIMO) [15], which is a multi-user MIMO system with M antennas and K users per base station, where $M \gg K$. The antenna array of the base station can have any geometry, as described in [15]. Hundreds of antennas equipped on the base station enable spatial multiplexing of tens of users, bringing at least ten-fold improvement in area throughput. Therefore, massive MIMO is believed to be an essential enabler of 5G.

Table 1.2: Evolution of mobile technologies [16]

Generations	Access Technology	Data Rate	Frequency Band	Bandwidth
1G	Advanced Mobile Phone Service (AMPS) (Frequency Division Multiple Access (FDMA))	2.4 kbps	800 MHz	30 kHz
2G	Global Systems for Mobil communications (GSM) (Time Division Multiple Access (TDMA))	10 kbps	850/900/ 1800/1900 MHz	200 kHz
	Code Division Multiple Access (CDMA)	10 kbps		1.25 MHz
2.5 G	General Packet Radio Service (GPRS)	50 kbps		200 kHz
	Enhanced Data Rate for GSM Evolution (EDGE)	200 kbps		200 kHz
3G	Wideband Code Division Multiple Access (WCDMA)/ Universal Mobile Telecommunications Systems (UMTS)	384 kbps	800/850/ 900/1800/ 1900/2100 MHz	5 MHz
	Code Division Multiple Access 2000 (CDMA2000)	384 kbps		1.25 MHz
3.5G	High Speed Uplink/ Downlink Packet Access (HSUPA/HSDPA)	5-30 Mbps		5 MHz
	Evolution-Data Optimized (EVDO)	5-30 Mbps		1.25 MHz
3.75G	Long Term Evolution (LTE) (Orthogonal/Single Carier Frequency Division Multiple Access (OFDMA/SC-FDMA))	100-200 Mbps	1.8/ 2.6 GHz	1.4 to 20 MHz
	Worldwide Interoperability for Microwave Access (WIMAX) (Scalable Orthogonal Frequency Division Multiple Access (SOFDMA)) *Fixed WIMAX	100-200 Mbps	3.5/5.8 GHz initially	3.5 and 7 MHz (3.5 GHz band); 10 MHz (5.8 GHz band)
4G	Long Term Evolution Advanced (LTEA) (OFDMA/SC-FDMA)	3 Gbps (DL) 1.5 Gbps (UL)	1.8/2.6 GHz	1.4 to 20 MHz

Table 1.2 continued from previous page

Generations	Access Technology	Data Rate	Frequency Band	Bandwidth
	Mobile WIMAX (SOFDMA)	100-200 Mbps	2.3/2.5/ 3.5 GHz Initially	3.5/7/5/ 10/8.75 MHz initially
5G	Beam Division Multiple Access (BDMA) and Non- and quasi-orthogonal or Filter Band Multicarrier (FBMC) Multiple Access	10-50 Gbps	1.8/2.6 GHz and expected 30-300 GHz	60 GHz

1.1.3 Evelotion of wireless local area networks

Wireless local area network (WLAN) plays an essential role in today's wireless networks as it carries a considerable portion of the global Internet traffic, therefore greatly offloading the cellular network. As the most successful type of WLAN, IEEE 802.11 standards family-based wireless fidelity (Wi-Fi) has been deployed worldwide due to its advantages such as low system complexity, high data rate, and low cost. Technology standards of Wi-Fi have undergone tremendous evolution. The first standard IEEE802.11a-1999 [17] enables up to 54 Mbps data rate with a channel bandwidth of 20 MHz at 5 GHz unlicensed frequency band by applying the OFDM modulation method. In IEEE 802.11n-2009 [18], single-user MIMO (SU-MIMO) is applied to improve the spectrum efficiency, and an aggregate data rate of up to 600 Mbps can be supported. Furthermore, in IEEE 802.11ac-2013 [19] standard, the channel bandwidth is extended to 160 MHz, and multi-user MIMO (MU-MIMO) is applied, resulting in higher spectrum efficiency and up to 866.7 Mbps single-channel data rate. However, Gbps-level data rate requirements from emerging wireless applications are still a big challenge for current Wi-Fi networks. As a response, the IEEE 802.11ad-2012 [20] aims to operate in the 60-GHz mmWave frequency band, obtaining an ultra-broad channel bandwidth of >1.88 GHz. Up to 4.6 Gbps ultra-high single-channel data rate can be supported [16]. However, such a 60-GHz Wi-Fi technique is suitable for short-reach and direct line-of-sight scenarios because of the high propagation loss caused by oxygen absorption of the 60 GHz band, which asks for more hotspots for the coverage of a certain area. The technical specifications of the main IEEE 802.11 standards are shown in Table 1.3.

On the other hand, with the exponential increase of mobile data traffic, the number of Wi-Fi hotspots is expected to increase explosively, resulting in ultra-dense Wi-Fi networks. To efficiently manage the massive amount of data transmitted in these networks, high-efficiency WLAN, where there is a large number of access points and a large number of stations associated with each access point, is proposed in IEEE 802.11ax-2019, which will be the successor of IEEE 802.11n-2009 and IEEE 802.11ac-2013 [21]. The scope of IEEE 802.11ax is [22]: "The IEEE 802.11ax standard scope defines standardized modifications to both the IEEE 802.11 physical layers and the IEEE 802.11 Medium Access Control (MAC) layer that enable at least one mode of operation capable of supporting at least four times improvement in the average throughput per station (measured at the MAC data service access point) in a dense deployment scenario, while maintaining or improving the power efficiency per station. This amendment defines operations in frequency bands between 1 GHz and 7.125 GHz. The new amendment shall enable backward compatibility and coexistence with legacy IEEE 802.11 devices operating in the same band".

Table 1.3: Technical specifications of the main IEEE 802.11 standards

Standards	IEEE 802.11a -1999	IEEE 802.11n -2009	IEEE 802.11ac -2013	IEEE 802.11ad -2012
Frequency	5 GHz	2.4/5 GHz	2.4/5 GHz	60 GHz
Channel Bandwidth	20 MHz	20/40 MHz	20/40/ 80/160 MHz	>1.88 GHz
Modulation Scheme	OFDM	OFDM	OFDM	OFDM, single carrier
Data Rate (single stream)	54 Mbps	150 Mbps (1×1, 40 MHz)	866.7 Mbps (1×1, 160 MHz)	4.6 Gbps
Aggregate Date Rate (multiple streams)	-	600 Mbps (4×4, 40 MHz)	3.47 Gbps (4×4, 160 MHz)	7 Gbps
Remark	Apply OFDM	Apply SU-MIMO	Apply MU-MIMO, high-density modulation (up to 256-QAM)	60 GHz mmWave

1.1.4 The emerging optical wireless communication networks

Following the path of seeking more bandwidth as adopted by the cellular and WLAN networks discussed in previous sections, one may notice a tremendous number of spectrum resources in the optical regime. This license-free treasure of spectrum resources is disclosed by emerging optical wireless communication (OWC) techniques [23], which mainly are visible light communication (VLC) [24] and beam-steered infrared (IR) light communication (BS-ILC) [25]. The visible light spectrum (roughly from 400 to 700 nm) contains about 320 THz of bandwidth. As for IR light, considering the spectrum used for high-speed optical fiber communication (O+S+C+L bands), where a large number of mature high-speed optical devices are available (modulators, optical sources, photodiodes, etc.), an ultra-broad bandwidth of no less than 38 THz can be exploited. These spectrum resources are far more than that of radio frequencies (RFs). Therefore, OWC is considered the ultimate approach to solve the problem of spectrum scarcity and meet the demand for higher-volume wireless communication. In a wide-coverage VLC system that shares capacity among multiple devices, besides providing illumination, light-emitting diodes (LEDs) are also used to transmit data through intensity modulation. On the receiving end, the signal is detected by a photodiode through a direct detection scheme. Beyond 10-Gbps data rate has been realized using LED-based wavelength division multiplexing [26]. The networked version of VLC is known as light fidelity (Li-Fi) [27], for which standardization has been started by IEEE 802.11 LC study group, aiming to provide higher data rate and capacity. Contrary to VLC, BS-ILC uses narrow two-dimensional (2D) steered IR beams to establish unshared high-speed wireless links with user devices individually. Therefore, it can offer a much higher data rate (hundreds of gigabits per second) [28–31].

Because of the particle nature of light, the coverage area of OWC is usually smaller and more distinct compared with that of radio wireless. Therefore, smaller communication cells can be created in OWC, enabling higher-density spectrum reuse. This dense spatial multiplexing opens the path to exponential capacity growth. Moreover, OWC provides extra privacy and security, as light does not penetrate walls. But the drawback is that OWC is not suitable for large-area and non-line-of-sight coverage. For this reason, OWC is not intended to replace radio wireless communication, but as a powerful supplement, offloading heavy traffic loads from congested radio wireless networks with its ultra-high data rate, especially for indoor scenarios, where a large fraction of Internet traffic occurs.

1.2 Future indoor wireless networks

From the discussions above, it can be found that two wheels from the physical layer are driving the wireless communication systems to catch up with the exponentially increasing capacity demands from emerging wireless applications, namely: spatial multiplexing and more bandwidth. The cases of the former one include mmWave beam steering and massive MIMO used in 5G cellular networks, MIMO used in WLAN networks, and IR beam steering used in OWC networks. The cases of the latter one include mmWave spectrum used in 5G cellular and WLAN networks, and wealth spectrum resources in OWC. Moreover, moving to higher frequencies (mmWave and optical) further enhances the capability of spatial multiplexing from two paths: 1) The reduced diffraction and penetration of EM waves at higher frequencies brings network architecture-based spatial multiplexing: smaller communication cells, which contribute the major portion to the increase of the density of radio communications in the past 45 years [23]. 2) The shorter wavelength reduces the antenna size, which in turn increases the number of antennas that can be deployed on a base station, thereby enabling advanced spatial multiplexing techniques such as massive MIMO and beam steering. For 5G cellular networks, small cell base stations and multiple antennas are seen as fundamental technologies [32]. Because nearly 80% of the mobile traffic volume is generated indoor [33], with the rollout of 5G cellular networks, a huge number of 5G small cells are going to be used to boost signals in indoor areas, such as shopping centers, offices, and homes. For WLNA networks, there will be a similar trend, as considered in IEEE 802.11ax. Not to mention the small cells of OWC networks.

In this context, to increase cost efficiency, energy efficiency, and system scalability while reducing system complexity, a converged wired-wireless indoor network that can support small cells of the aforementioned wireless networks is needed. Considering the future evolution, let's be more general, a converged wired-wireless indoor network that not only supports future RF and optical frequency but also supports advanced spatial multiplexing techniques including but not limited to RF massive MIMO, RF beam steering, and IR beam steering is needed. Such an indoor wireless network should be able to meet the following four requirements: ① Has broadband link medium for emerging bandwidth-hungry wireless services. ② Simultaneously supports different frequency bands ranging from RF to optical, including 2.4 GHz, 5 GHz, future mmWave (28 GHz, 38 GHz, 60 GHz, and others), and optical frequencies. ③ Has a very cost-efficient architecture. Since many access points of different wireless networks are going to be installed indoors, and the costs of indoor networks are borne by building owners/users, which is different from operator-owned outdoor networks, low cost becomes an important requirement. ④ Supports advanced spatial multiplexing techniques for future exponentially increasing capacity demands.

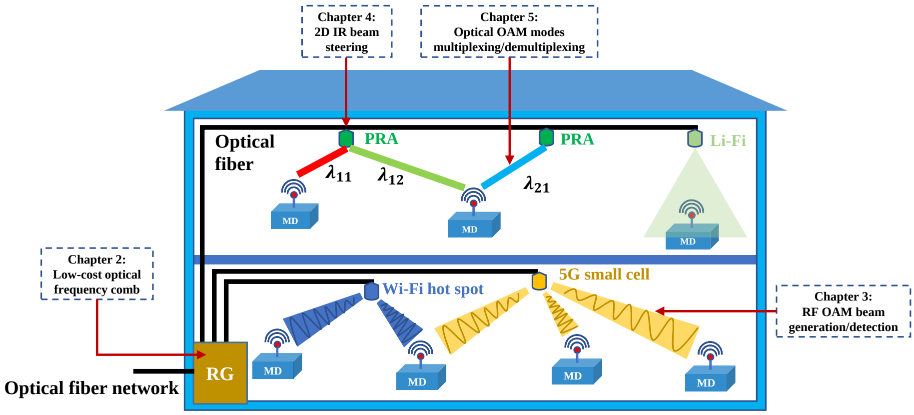

Figure 1.2: Future converged fiber-wireless indoor network. MD: mobile device, PRA: pencil-radiating antenna, RG: residential gateway.

1.2.1 Converged fiber-wireless indoor network

Combining the excellent works of the Electro-Optical Communication Group of Eindhoven University of Technology [23, 25, 34–39] and the big picture of wireless communication evolution, the architecture of future converged fiber-wireless indoor network can be obtained, as shown in Figure 1.2. Optical fiber is used as the network medium to connect all the access points of different wireless networks into a converged network due to the advantages of low-loss, EM interference-free, compact in size, and most importantly, ultra-broadband, which meets the requirement ①. Here, silica single-mode fiber (SMF) is preferred because SMF links are fully transparent for all signal formats, and they can deploy a wide range of wavelength channels for multiplexing many different kinds of services. Such features are essential for compatibility with different wireless networks and are essential to provide enough capacity. Besides, because of the single-mode waveguiding of SMF, fully-passive power splitting or wavelength routing devices can be used, which reduces operating costs. On the other hand, for scenarios of lower bandwidth and short links, such as home networks, plastic optical fiber (POF) is a very interesting low-cost fiber network solution due to its ductility and large light-guiding core, which makes it easy to couple (do-it-yourself), reducing installation costs. Although POF has a limited bandwidth due to its large core, Gbps transmission speed can still be achieved [39].

In the proposed converged fiber-wireless indoor network, a centralized network architecture is built, as shown in Figure 1.2. The signal processing units in remote RF or optical access points, including up/downconversion and baseband signal processing, are moved to the central site, i.e., the residential gateway (RG). Such a fiber-wireless network is inherently compatible with OWC. Modulated optical signals can be delivered to remote optical access points through fiber, and then directly transmitted to users wirelessly after amplification. RF access can be realized by using the revolutionary radio-over-fiber (RoF) technology [40]. To support different kinds of RF wireless services at different frequencies, different RF carriers (mainly mmWave carriers) can be generated centrally by using highly efficient photonic techniques [40] in the RG. After upconversion, RF signals at desired wireless transmission frequencies are modulated onto optical carriers, and then transmitted over fiber in the RF-over-fiber scheme. In the remote RF access points, RF signals can be recovered with high-speed photodetectors and then directly transmitted to users wirelessly after amplification. Therefore, the requirement ② is met.

A remote RF or optical access point here serves as a simple active antenna, with no need for signal processing. With this configuration, the complexity of RF/optical remote access points can be largely reduced, and therefore also the cost, power consumption, and the difficulty in installation and maintenance, which is a major benefit for the dense deployment of 5G, Wi-Fi, and OWC small cells in the future. Moreover, new signal processing standards can be flexibly upgraded and configured in the center without replacing the remote access points, which is excellent for continuously evolving wireless services. Therefore, the requirement ③ is met.

1.2.2 Key research points

Based on the above discussions, the following key research points can be highlighted to realize the proposed converged fiber-wireless indoor network:

- **Low-cost high-performance optical frequency comb source for indoor RoF system**

  Since all signals are processed and modulated onto optical carriers centrally, extremely huge data traffic can be expected for the RoF system of the converged fiber-wireless indoor network, which makes low-cost broad-bandwidth optoelectronic devices with excellent linearity and low phase noise essential. Here, we pay special attention to optical frequency comb sources. In the frequency domain, an optical frequency comb [41]

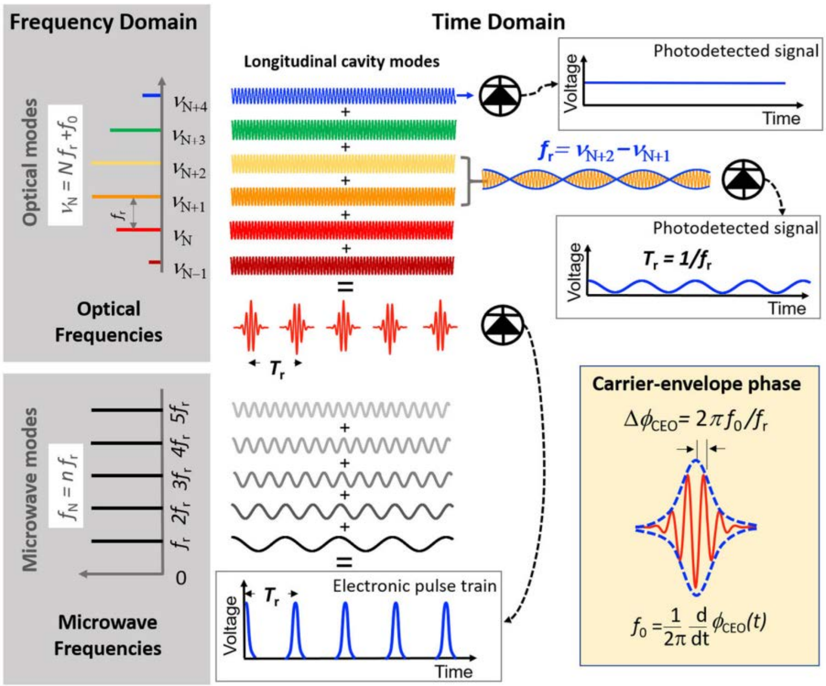

Figure 1.3: Time and frequency domain representation of an optical frequency comb, which connects optical and RF domains [41].

consists of a series of discrete, equally spaced frequency lines, and there is a fixed-phase relationship between these frequency modes. In the time domain, it produces a periodic train of optical pulses. As shown in Figure 1.3, an optical frequency comb can link an array of coherent radio frequencies to an array of coherent optical frequencies. The produced optical pulse train with period T_r corresponds to the mode spacing (or repetition rate) $f_r = 1/T_r$ in the frequency domain. The precise value of any optical mode is determined by the expression $\upsilon_N = N f_r + f_0$, where $f_0 \leq f_r$ is the offset frequency, which relates to time-changes of the optical carrier phase relative to the pulse envelope (carrier-envelope offset phase $\phi_{CEO}(t)$); N is an integer mode number on the order of 10^5. By using a photodetector for direct detection, the optical pulse train can be converted into an electronic pulse train, which can be expanded into RF Fourier harmonics

$f_N = nf_r$, where $n = 0, 1, 2, ...$ No offset frequency exists for RF harmonics because the optical carrier is eliminated by the photodetection. It can be seen that coherent radio frequencies of nf_r are linked with coherent optical frequencies of $Nf_r + f_0$. Therefore, RF carriers of nf_r can be generated by using an optical frequency comb with mode spacing f_r. Conversely, such an optical frequency comb can also be obtained through amplitude modulation of a continuous optical carrier, as shown in the yellow shaded inset of Figure 1.3.

In the indoor RF system, optical frequency combs can be used to efficiently generate RF carriers, providing low-cost flexible solutions for generating RF signals with different frequencies of many different wireless services. Besides, optical frequency combs can also be used to offer coherent optical carriers for dense wavelength-division multiplexing (DWDM), which is a crucial optical fiber multiplexing technology using a set of parallel optical channels with slightly different wavelengths to significantly increase the system capacity and deal with the huge data traffic. Due to the broadband phase coherence provided by optical frequency combs, the receiver scheme can be simplified by performing joint reception and processing of several wavelength channels [42], reducing the phase tracking complexity and increasing the transmission performance. Therefore, **low-cost high-performance optical frequency comb sources for the indoor RoF system** are considered a key research point.

- **Photonics techniques for spatial multiplexing in the converged fiber-wireless indoor network**

  As discussed previously, the proposed converged fiber-wireless indoor network aims to support future 5G and beyond cellular, WLAN, and OWC networks, so it needs to support advanced spatial multiplexing techniques of these networks (the requirement ④). In the converged fiber-wireless indoor network, because all signals are modulated onto optical carriers and transmitted to remote access points over fiber, the key points move to enable advanced spatial multiplexing with photonic techniques.

  As shown in Figure 1.2, beam steering techniques implemented in the future indoor 5G small cells, Wi-Fi hotspots, and pencil-radiating antennas (PRAs) are essential to boost the network capacity and user density further while keeping the network energy-efficient, thus have attracted a lot of attention [38, 43, 44], and are still being studied extensively. Here, we focus on **photonic techniques for optical beam steering**. RF beam steering is the topic of other researchers in our research group.

If we shift our focus to a single beam, a new spatial multiplexing degree of freedom can be found, which is orbital angular momentum (OAM) [45], one of the fundamental physical properties of EM waves. The total angular momentum of EM waves can be divided into two parts: spin angular momentum (SAM) and OAM. SAM is associated with polarization vector rotation. OAM is associated with phase structure rotation. A beam carrying OAM has a helical phase front and a related doughnut intensity profile in the plane perpendicular to the transmission direction. The helical phase is characterized by the azimuthal phase term of $\exp(il\varphi)$ in the electric fields [46, 47], where l is the eigenvalue of the OAM and usually known as topological charge, and φ is the azimuthal angle. Theoretically, the eigenvalues are unlimited, providing infinite eigenmodes (or orthogonal states) of EM waves. Therefore, different OAM modes can be used as orthogonal communication channels [48,49] to further boost the capacity-increase for both RF and optical communications [50–52]. Furthermore, OAM can be embedded in a massive MIMO system to achieve multiplicative spectrum efficiency [53]. OAM multiplexing is considered one of the enablers of 6G networks [54–56], which makes **photonic techniques for RF and optical OAM modes multiplexing** a key research point.

1.3 The scope of this thesis

Based on the future converged fiber-wireless indoor networks discussed in Section 1.2.1 and the key research points highlighted in Section 1.2.2, this thesis provides solutions to the following two categories of challenges. The proposed techniques aim to enhance the marked positions of Figure 1.2, and the corresponding system sketches are shown in Figure 1.4, in which the proposed systems/devices are framed by red dashed boxes.

- **Low-cost high-performance optical frequency comb source for indoor RoF system**

  In Chapter 2, we developed an O-band frequency comb source based on a passively mode-locked InAs quantum dot laser that has achieved an ultra-stable repetition rate of 25.5 GHz with 0.07 GHz deviation over the widest temperature range (from 20°C to 120°C) yet reported for any type of mode-locked laser. These achievements are enabled by the high dot density and engineered quantized energy difference between the ground state and the first excited state, which is realized by the optimized self-assembled InAs quantum dot growth method. The measurement results demonstrate the fabricated device as an ultra-stable, uncooled frequency comb source for low-cost, large-bandwidth, and low-energy-consumption phase-coherent DWDM multi-channel indoor RoF systems.

- **Photonics techniques for spatial multiplexing in the converged fiber-wireless indoor network**

  - **Photonics techniques for RF-OAM modes generation/detection**
    In chapter 3, a novel electrically-controlled optical broadband phase shifter (ECO-BPS) with the measured phase error of 3.44° from 12 GHz to 20 GHz is proposed for generating/detecting multiple RF-OAM modes. With a novel Dammann vortex grating-based crosstalk investigation method, the performance of the ECO-BPS is carefully analyzed, including the crosstalk between the OAM channels at the demultiplexer side. By comprehensive numerical analysis and experimental broadband demonstration from 12 to 20 GHz, it is convincingly shown that by using the ECO-BPS, RF-OAM modes can be readily generated and transmitted with high purity and little crosstalk.
  - **Photonics techniques for optical beam steering**
    In Chapter 4, enabled by the designed and fabricated novel small-phase-gradient (45°) gap-surface plasmon metasurface-based polarization beam splitter, a centrally wavelength-polarization-controlled 2D beam steering system with full-area coverage capability is proposed. In the system example, a 2D beam-steering angle range of $\pm 13.8° \times 49.8°$ is achieved with a wavelength tuning range of C-band. The proposed system keeps high scalability to support multiple beams, flexibility to steer the beam, high optical efficiency, simple and cheap devices on remote sides, and centralized control to lower maintenance costs. As a proof-of-concept, a 1.2-m 20-Gbps beam-steered infrared wireless link is experimentally demonstrated.
  - **Photonics techniques for optical OAM modes multiplexing/demultiplexing**
    In Chapter 5, by combining the Dammann vortex grating approach, which is capable of simultaneously multiplexing/demultiplexing massive OAM beams with independent modulation, and the metasurface techniques developed previously, a metasurface-based 1×2

Dammann vortex grating, which has an intrinsic topological charge of +3, is designed, fabricated, and measured as a low-cost, high-efficiency method for $l = \pm 3$ optical OAM modes multiplexing/de-multiplexing. With the fabricated grating, $l = +3$ and $l = -3$ optical OAM beams are generated and transmitted respectively through 0.2-m free space with a 40-Gbps data rate.

Finally, in Chapter 6, the achieved results are summarized, and the future outlook is comprehensively discussed.

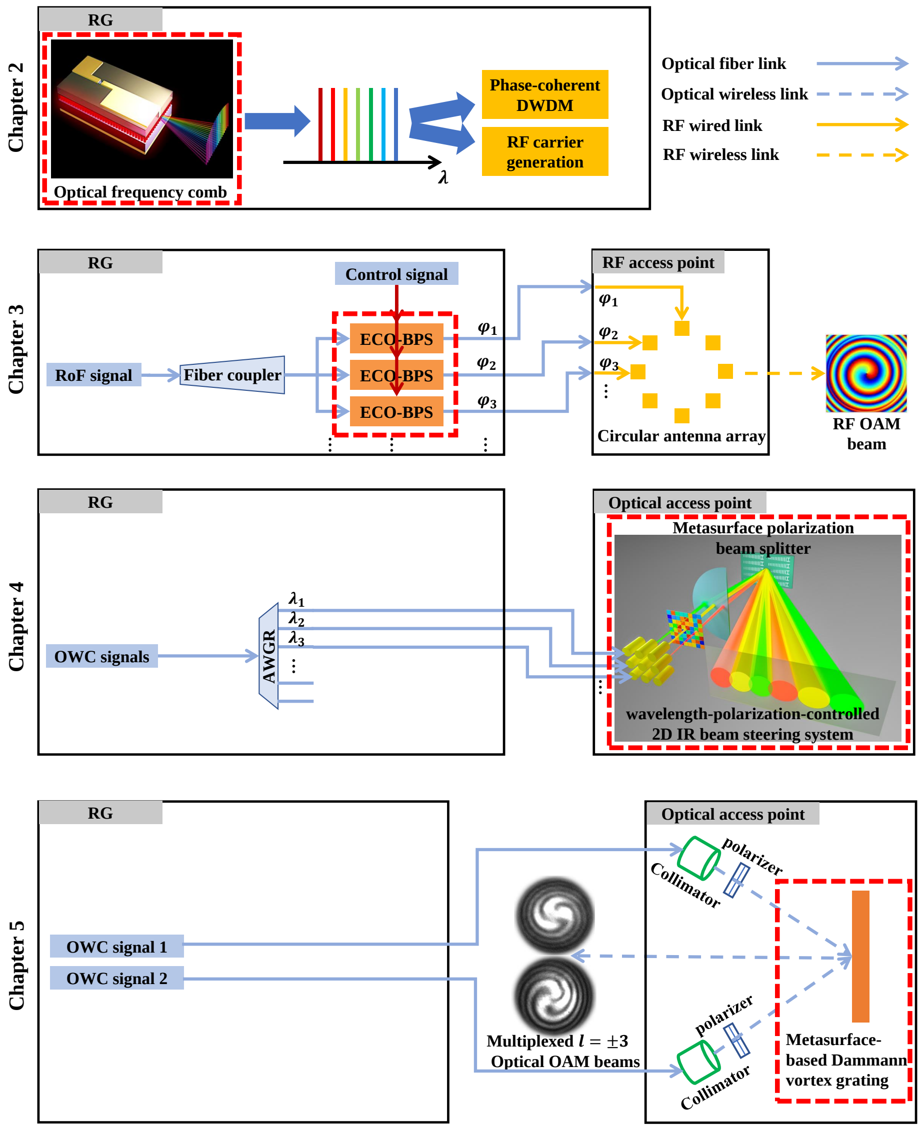

Figure 1.4: System sketches of the proposed solutions. The proposed systems/devices are framed by red dashed boxes. 2D: two-dimensional, DWDM: dense wavelength-division multiplexing, ECO-BPS: electrically-controlled optical broadband phase shifter, IR: infrared, OAM: orbital angular momentum, OWC: optical wireless communication, RF: radio-frequency, RG: residential gateway, RoF: radio-over-fiber.

Chapter 2

Uncooled Optical Frequency Comb Source for Indoor RoF System

In low-cost high-speed indoor RoF systems, optical frequency comb sources are essential for RF carrier generation [40] and phase-coherent DWDM multi-channel transmissions [42]. It is very attractive to apply semiconductor mode-locked lasers (MLLs) as frequency comb sources due to their advantages of low cost, compact in size, and high energy efficiency, which perfectly matches the requirements of the indoor communication network. In this chapter, an uncooled quantum dot (QD) MLL is designed, fabricated, and measured for low-cost phase-coherent DWDM multi-channel indoor RoF systems. The designed QD MLL operates in O-band because 1) silica optical fiber has low attenuation in O-band; 2) silica glass has a zero dispersion window in O-band. This is a collaboration work with University College London, and the corresponding publication (Pan S, Huang J, et al. Quantum dot mode-locked frequency comb with ultra-stable 25.5 GHz spacing between 20°C and 120°, *Photonics Research*, 2020) is co-first authored by Shujie Pan and Jianou Huang.

The practical indoor RoF system requires a frequency-stable comb source working in a temperature-varying environment with a minimum mode spacing of 25 GHz to support phase-coherent DWDM transmissions. Since 25 GHz is also a relevant value for 5G New Radio mmWave bands (24.25 GHz to 52.6

GHz) [57], such frequency comb source can support corresponding RF carrier generation at the same time. To the best of our knowledge, however, to date, there have been no demonstrations of comb sources that simultaneously offer a high repetition rate and stable mode spacing over an ultrawide temperature range. Here, we report a frequency comb source based on a QD MLL that generates a frequency comb with stable mode spacing over an ultrabroad temperature range of 20-120°C. The fabricated two-section passively mode-locked InAs QD MLL comb source produces an ultra-stable fundamental repetition rate of 25.5 GHz (corresponding to a 25.5 GHz spacing between adjacent modes in the frequency domain) with a variation of 0.07 GHz over the tested temperature range. By keeping the saturable absorber reversely biased at -2 V, stable mode-locking over the whole temperature range can be achieved by tuning the current of the gain section only, providing easy control of the device. At an elevated temperature of 100°C, the device shows a -6 dB comb bandwidth of 4.81 nm and 31 tones with >36 dB optical signal-to-noise ratio. The corresponding relative intensity noise, averaged between 0.5 GHz and 10 GHz, is -146 dBc/Hz. Our results show the viability of the InAs QD MLLs as ultra-stable, uncooled frequency comb sources for low-cost, large-bandwidth, and low-energy-consumption phase-coherent DWDM multi-channel indoor RoF systems.

2.1 State-of-the-art and challenge

2.1.1 State-of-the-art

Optical frequency combs consisting of equally spaced discrete optical frequency components have emerged as promising tools for a wide range of applications, including metrology, optical communications, optical clock distribution/recovery, RoF signal generation, and optical sampling [42, 58–63]. Integrated comb sources are particularly attractive due to the size and power consumption advantages and are being heavily investigated as light sources for short and medium reach DWDM communication systems [42, 59]. For instance, a microring-resonator-based Kerr frequency comb has been used to demonstrate C+L band coherent communications with >30 Tbps data rate [59]. Furthermore, for RoF systems, in addition to supporting phase-coherent DWDM transmissions, optical frequency combs are also used for forming multiple RF carriers [64–66]. However, practical systems also require a comb source to work stably over a wide temperature range (e.g., -20°C to 85°C).

A semiconductor MLL represents a simple and low-cost approach to generate frequency combs. Short-cavity MLLs can generate high repetition rate (thus, large mode spacing), stable mode spacing, and high optical signal-to-noise ratio (OSNR) frequency combs that suit phase-coherent DWDM transmissions and RF carrier generation. An MLL typically provides 5–10 nm bandwidth, promising comb-based transmitters [67]. The recent development of QD semiconductor materials and modeling theories [68–70] promise an ultrabroad gain bandwidth and ultrafast carrier dynamics [71], with many other important features including large gain and saturable absorber (SA) saturation energy ratio [72], low spontaneous emission rate [73], and the capability for monolithic integration with silicon substrates [74–77]. These promising features have inspired much research in the development of high-performance QD MLLs [78–83] and their applications for multi-Tbps communications [84–88].

Temperature resilience has long been the hallmark of QDs, mainly due to their delta-function-like density of states [89]. While high-temperature continuous-wave (CW) operation up to 220°C from InAs QD Fabry–Perot lasers has been demonstrated [90], exclusively from the QD ground state (GS) transition, turning this prediction into reality for QD MLLs involves not only thermal mechanisms but also the mutual interdependence of the gain section and the SA in two-section passive devices. The work of Cataluna et al. first emphasized the stability of mode-locking in 20 GHz InGaAs QD MLLs at elevated temperatures. However, the device exhibited unstable mode-locking operation over 70°C evidenced by RF SNR quenching (15 dB at 80°C) [91]. Stable mode-locking, exclusively through GS transition, from 20°C to 92°C, has also been demonstrated from two-section passive InAs QD MLLs [92]. However, mode-locking switching between GS and the first excited state (ES1) appears due to the carrier escape from the GS with increasing temperature, and the long laser cavity of 8 mm employed in their work limited the fundamental repetition rate to 5 GHz, which is not high enough to meet the minimum requirement (e.g., 25 GHz) of DWDM systems.

2.1.2 Challenge and the proposed solution

Although one may expect a broad mode-locking temperature range from one QD mode-locked device [91, 92] and observe a large mode spacing from another [93], a key challenge is to achieve simultaneously ultra-stable mode spacing over an extremely broad temperature range from a single frequency comb source with large mode spacing. In this chapter, by developing a QD active region with high dot density and large energy separation between the GS and higher energy states, we demonstrate stable mode-locking operating over a record temperature range between 20°C and 120°C. Our QD MLL operates in the telecom O-band and exhibits coherent optical pulses at a repetition rate of 25.5 GHz, and correspondingly, 25.5 GHz spacing between adjacent modes in the frequency domain. With temperature increased from 20°C to 120°C, the mode spacing changes by only approximately 0.07 GHz. Moreover, our device emits a comb bandwidth of 4.81 nm at an operating temperature of 100°C with 31 total channels within the -6 dB comb bandwidth. The corresponding average relative intensity noise (RIN) for the whole lasing spectrum was measured to be -146 dBc/Hz in the frequency range from 0.5 GHz (due to the limitation of the equipment) to 10 GHz. The demonstrated performance suggests the developed QD MLL is a strong candidate for an ultra-stable, uncooled frequency comb source that can be employed in a phase-coherent DWDM multi-channel indoor RoF systems with high capacity and efficiency.

2.2 Realization of the uncooled QD MLL

2.2.1 Material and epitaxial growth

The InAs QD laser structure was grown on a Si-doped GaAs (001) substrate using molecular beam epitaxy. The epitaxy starts with a 300 nm thick n-type GaAs buffer layer followed by a combination of n-type $Al_{0.2}Ga_{0.8}As/Al_{0.4}Ga_{0.6}As/Al_{0.2}Ga_{0.8}As$ in a thickness of 200 nm/1400 nm/200 nm, which acts as the lower cladding layer. Above the lower cladding layer is the active region, followed by another combination of $Al_{0.2}Ga_{0.8}As/Al_{0.4}Ga_{0.6}As/Al_{0.2}Ga_{0.8}As$ p-type upper cladding layer in a thickness of 200 nm/1400 nm/200 nm, respectively, and finally a 300 nm highly p-doped GaAs contact layer. A high optical gain is always desired for high-temperature operation of QD lasers; here, to this end, a larger than usual number of QD layers, with higher dot area density, were employed for the QD active region. For the growth of the active region, without adopting a conventional InAs/InGaAs/GaAs dot-in-a-well structure, where the InAs layer is sandwiched by InGaAs layers, here, InAs QDs were formed self-assembly on a GaAs surface by depositing a three-monolayer InAs QD layer directly on the GaAs surface. The initial InAs QDs were then covered by a 3.7 nm InGaAs strain-reducing layer, and such coverage growth conditions were also optimized to suppress ad-atom migration during the coverage. By doing so, the original uniformity can be kept without sacrificing dot density and multilayer structures. This could result in rather narrow photoluminescence (PL) emission from those QDs. Figure 2.1(a) illustrates the cross-sectional transmission electron microscopy (TEM) image of the active region presented in this chapter, comprising a tenfold layer stack of InAs QDs (twice the number of layers previously used in Ref. [74]). From the high-resolution bright-field scanning TEM image of a single dot, as shown in the inset of Figure 2.1(a), the typical dot size is ~20 nm in diameter and ~7 nm in height. Dot density as high as 5.9×10^{10} cm^{-2} is typically obtained in these structures [94] (nearly double the previous dot density of 3×10^{10} cm^{-2}). Figure 2.1(b) compares the room temperature PL spectra for the full QD laser epi wafer grown under previous conditions and the optimized growth condition, which has been employed in this work. As seen, despite the high dot density that was achieved, the PL full width at half maximum (governed by the inhomogeneous broadening due to size and shape distribution of the QDs) remained as low as 30 meV, which is comparable to our previous observation of 29 meV with low dot density. The combined effects have led to an enhancement of integrated PL intensity of the optimized sample at 2.6 times higher than the previous one. In addition, the quantized-energy difference (ΔE) between the GS and ES1 increased from 68 meV to 88 meV. The enhanced energy separation plays a vital role in effectively suppressing the carrier overflow and Auger recombination at elevated temperatures [90].

2.2.2 Device design and fabrication

Figure 2.1(c) shows a schematic diagram of the fabricated MLL. As can be seen, the device has a typical two-section ridge-waveguide laser structure with a 15 μm gap in the top p-contact metal pads, and the ridge width is 5 μm. To achieve a fundamental repetition rate of 25 GHz, the total length of the laser investigated in this chapter was set to be 1615 μm with the length of the absorber designed to be 200 μm, corresponding to a gain-to-absorber length ratio of 7:1. The isolation between the gain section and the absorber section is achieved by using shallow wet etching to selectively remove the heavily p-doped contact layer in the gap region, as indicated in Figure 2.1(d). The measured isolation resistance is 8 kΩ. No coating is applied to the cleaved facets. The devices were mounted p-side up on an indium-plated copper heat sink and gold-wire-bonded to enable testing.

The MLL was fabricated in the NanoLab of Eindhoven University of Technology through the following main steps: 1) Ridge waveguides fabrication. The ridges were firstly defined by electron beam lithography (EBL) and then etched by inductively coupled plasma etching. After the ridge etching, a thin SiO_2 passivation layer was immediately deposited on the sample by plasma-enhanced

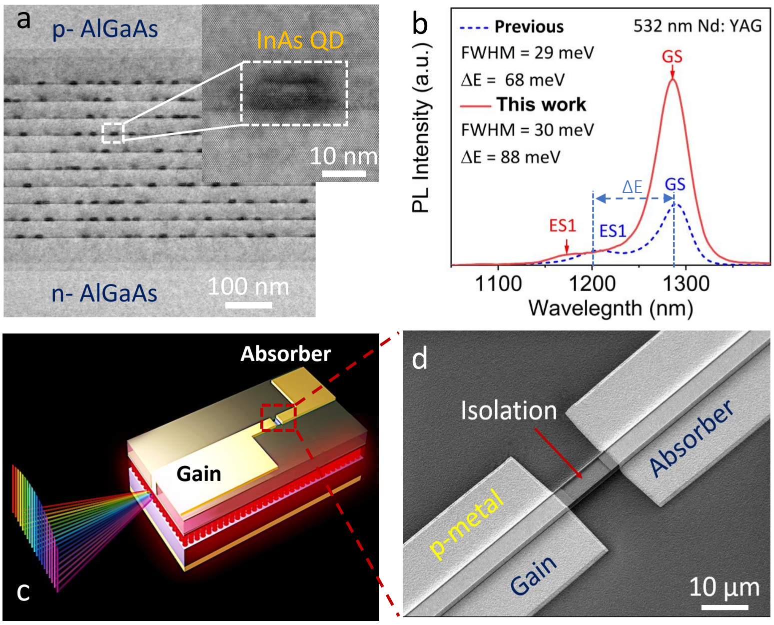

Figure 2.1: (a) Cross-sectional TEM image of the active region. The inset shows the high-resolution bright-field scanning TEM image of a single dot. (b) Comparison of the room temperature PL spectra for samples grown under previous conditions and the optimized growth conditions employed in this work. (c) Schematic of the passive two-section MLL. (d) SEM image of the device showing the gap between the gain and SA.

chemical vapor deposition to avoid further oxidation of the Al-containing layers. 2) Surface planarization. A thick HD4104 polyimide layer was spin-coated on the sample and then thermally cured in a vacuum oven. 3) Etching back. The covered p-contact areas were etched open by reactive ion etching. 4) P-contact pads fabrication. The Ti/Pt/Au p-contact metal pads were progressively defined and fabricated by EBL, metal evaporation, and acetone lift-off. 5) Electrical isolation of the gain section and the absorber section. The isolation areas were firstly defined by EBL. Then the corresponding heavily p-doped contact layer was etched away by using a solution consisting of hydrogen peroxide, citric acid, and water. 6) N-contact pads fabrication. The sample was firstly thinned, and then the Ni/Ge/Au n-contact metal pad was deposited on the back of the sample. 7) The final step was the rapid thermal annealing of the metal pads.

Scanning electron microscope (SEM) measurements were performed during the fabrication to verify the fabrication accuracy and the process results: 1) After the ridge etching, the widths of the ridges were measured, and the sidewalls of the waveguides were checked to verify the etching quality. 2) Before the p-contact pads fabrication, corresponding p-contact areas were checked to ensure the heavily p-doped contact layer was totally exposed. 3) After the wet etching, the isolation areas were checked to ensure the corresponding heavily p-doped contact layer was etched away.

2.3 Characterization of the device

2.3.1 Continuous-wave performance

CW performance of the fabricated InAs QD MLL comb source was first characterized at room temperature, as shown in Figure 2.2. Figure 2.2(a) shows typical light-current (*L-I*) characteristics at various reverse-bias voltages. As seen, while the *L-I* characteristics did not reveal pronounced hysteresis on the device under investigation, the nonlinear saturation effect of the SA can be observed for the higher reverse-bias voltages evidenced by the sudden power rise near the threshold. Incrementing the reverse-bias voltage caused a threshold increase from 17 mA to 29 mA due to the enhanced absorption loss within the SA region, which, as would be expected, also leads to decreased slope efficiency. The range of driving conditions over which stable mode-locking occurs in this device is illustrated in Figure 2.2(b). In this work, a stable mode-locking state was defined as a fundamental frequency tone SNR of over 25 dB [resolution bandwidth (RBW): 1 MHz, video bandwidth (VBW): 10 kHz] and the corresponding pulse width narrower than 15 ps. Here, although the device configuration of a high gain-to-absorption ratio of 7:1 was employed, stable mode-locking over a wide range of drive currents ranging from 30 mA to 115 mA and reverse-bias voltages from 1.5 V to 7 V was demonstrated. A wider range of mode-locking driving conditions could be achieved by employing device configurations with lower gain-to-absorption ratios [72, 95].

Figure 2.2(c) depicts a representative RF trace for the bias conditions of I_{gain} = 75.22 mA and V_{SA} = -2.9 V. A narrow linewidth fundamental RF tone at 25.54 GHz with an SNR of 47.9 dB is clearly indicated, corresponding to the free spectral range of our device. The absence of low-frequency fluctuations or Q-switched mode-locking is also noted. The corresponding autocorrelation

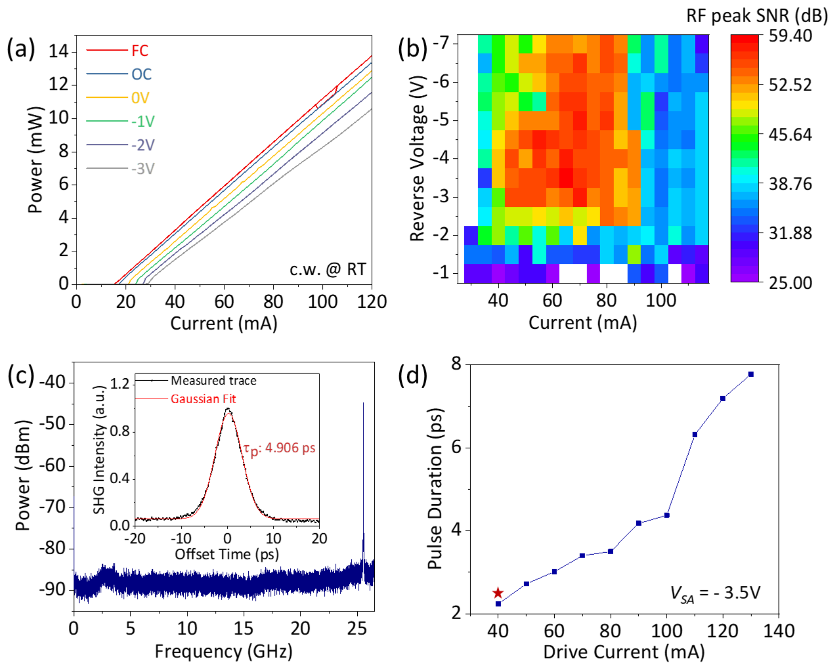

Figure 2.2: Two-section passive QD-MLL performance characterization at room temperature. (a) *L-I* characteristics for different SA reverse-bias voltages. (b) Fundamental RF peak SNR mapping. (c) RF spectrum in a 26.5 GHz span view (RBW: 1 MHz, VBW: 10 kHz). The inset shows the autocorrelation trace with Gaussian pulse fitting. (d) Pulse duration as a function of I_{gain} with V_{SA} = -3.5 V.

trace is displayed in the inset of Figure 2.2(c). A pulse duration of 4.906 ps was obtained, assuming a Gaussian pulse profile. Shorter pulse durations were observed from the same device at lower driving currents and higher reverse-bias voltages, as shown in Figure 2.2(d), where the narrowest pulse of 2.23 ps was achieved under the bias conditions of I_{gain} = 40 mA and V_{SA} = -3.5 V. The pulse duration is expected to be further shortened by decreasing the gain-to-absorption ratio through more effective shaping dynamics within the QD material [72].

The effect of temperature on the *L-I* characteristics, when the reverse-bias voltage was fixed at 0 V, is presented in Figure 2.3(a) for the same device as il-

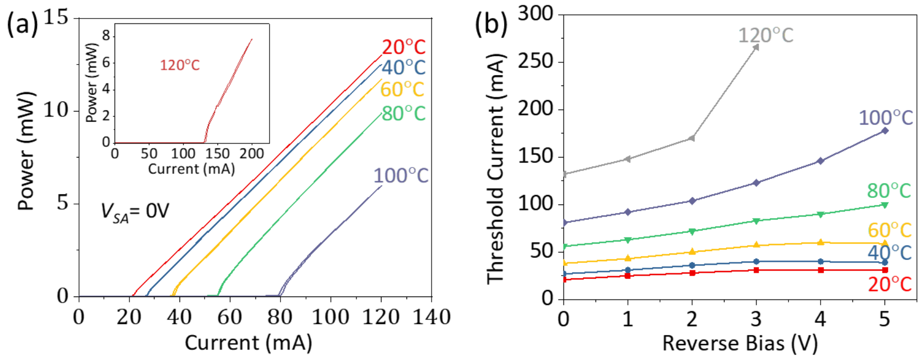

Figure 2.3: (a) Typical CW *L-I* characteristics of the two-section QD MLL as a function of temperature when V_{SA} = 0 V. (b) Dependence of threshold current on reverse-bias voltage and temperature.

lustrated in Figure 2.2. CW lasing was maintained until the testing was stopped at a heatsink temperature of 120°C due to the limitation of the test system. Under these conditions, no thermal rollover behavior was observed. Figure 2.3(b) highlights the effect of changes in the temperature and SA reverse-bias voltage on the threshold current. While, at a fixed reverse-bias voltage, for an increase in the temperature, the threshold current is generally increased, the calculated characteristic temperature T_0 remains an almost consistent value of around 55 K with reverse-bias voltage, indicating that T_0 is ultimately related to the physical properties of the gain section. This observation has also been previously observed in two-section quantum-well as well as QD lasers [96]. It is also noted that the modulation of loss in the SA by the reverse-bias voltage was more prominent for high temperatures, which was evidenced by the subtle hysteresis loops observed when the temperature exceeded 60°C.

2.3.2 Temperature performance

To evaluate the temperature performance of our QD MLL comb source, RF spectra were first measured as a function of temperature at a fixed reverse-bias voltage of 2 V, as shown in Figure 2.4(a). The driving currents were 49, 60, 64.7, 85, 148.5, and 210 mA at 20, 40, 60, 80, 100, and 120°C, respectively, chosen because it produces the shortest pulse width at the given temperature. Stable mode-locking operation over an extended temperature range from 20°C to 120°C has been achieved, with the SNR well over 30 dB and the corresponding pulse width narrower than 9 ps presented in Figure 2.4(c). To the best of our knowledge, this is the broadest mode-locking operation temperature range ever reported to date for any type of MLL. It was of significance, observed in Figure 2.4(b), that the change in mode spacing was only 0.07 GHz over the extremely broad temperature range of 100°C. Typically, an increase in the temperature leads to thermal expansion of the cavity length, and subsequently, a reduction in the mode spacing. However, as the temperature increases, the reduced refractive index of the semiconductor for a given wavelength results in an increase in the mode spacing. For the results presented, the effect of temperature on thermal expansion of the laser and the change of refractive index is well balanced, and thus the mode spacing remains ultra-stable with temperature, which is a desirable feature for optical communications. Furthermore, given that the temperature-dependent operation of a passive two-section MLL involves a mutual interplay of the gain section and the SA, here, for the device presented, with the SA reversed biased at a constant voltage, stable mode-locking over an ultrabroad temperature range has been easily achieved by simply adjusting the electrical biasing conditions, which yields an added benefit of bias simplicity.

The pulse duration change over temperature is presented in Figure 2.4(c); as seen, the value ranges from ~5 ps to ~8 ps between 20°C and 120°C. Note that the pulse duration presented here indicates the shortest pulse width that can be achieved at the given temperature. By carefully optimizing the driving conditions at each temperature, a relatively stable pulse duration of ~8 ps over the entire temperature range between 20°C and 120°C could be achieved. Figure 2.4(d) shows a color contour map depicting the regions of fundamental mode-locking (25.5 GHz) from 20°C to 120°C where the measured SNR of the RF tone is larger than 25 dB. It is worth mentioning that the range of driving conditions for expected stable mode-locking at each temperature should be broader than indicated since the testing range employed was underestimated [97]. Even so, it is quite apparent that an achievable mode-locking range shrinks as the temperature increases.

QD MLLs that operate at the GS are of interest in the context of optical communication systems owing to the desirable features of low power consumption and high wall-plug efficiency. However, operation at higher temperatures may shift the emission to the ES1 because of their lower gain and the relatively small quantized energy separation between the GS and the ES1. It was also thought that this phenomenon occurs more notably for those in shorter cavity QD MLLs with higher repetition rates. In this work, mode-locking exclusively from the GS has been achieved over the entire temperature range from 20°C to

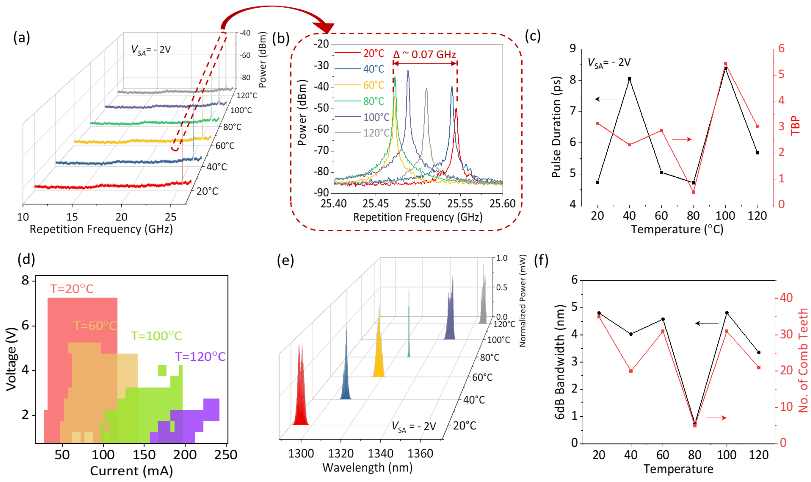

Figure 2.4: Temperature-dependent characteristics of two-section passive QD-MLL with a constant V_{SA} = -2 V and I_{gain} of 49, 60, 64.7, 85, 148.5, and 210 mA at 20, 40, 60, 80, 100, and 120°C, respectively. (a) RF spectra (RBW: 1 MHz, VBW: 10 kHz). (b) Zoomed-in RF spectra, as shown in (a). (c) Pulse duration. (d) Color map depicting the regions of fundamental mode-locking (25.5 GHz) from 20°C to 120°C where the SNR > 25 dB. (e) Optical spectra (resolution: 0.03 nm, VBW: 200 Hz). (f) -6 dB bandwidth and the orresponding number of comb teeth.

120°C, evidenced by the measured optical spectra as a function of temperature shown in Figure 2.4(e). It is noted that the absolute wavelengths of the MLL are indeed changing versus their operating temperature (-0.7 nm/°C), which is an undesirable feature for practical comb applications. However, by carefully tailoring the QD structure as well as the laser cavity length, i.e., achieving an optimum cavity design for a given gain function [98], this thermal-induced red shift could be dramatically restricted. Therefore, it would be possible to obtain a stable mode-locked QD comb source with an extremely low change in the wavelength of each comb line with temperature. Nevertheless, the small change of mode spacing achieved in this work promises a small guardband between adjacent DWDM channels [67], ensuring high spectral efficiency for multi-Tbps interconnects. Figure 2.4(f) summarizes the optical spectrum flatness at each temperature under the same driving condition as in Figure 2.4(e). As seen, the -6 dB comb bandwidth for most of the conditions is relatively constant within

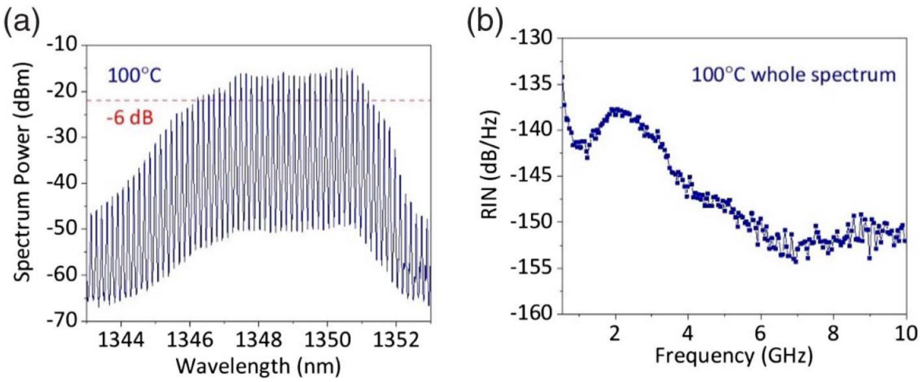

Figure 2.5: (a) Optical comb under bias conditions of I_{gain} = 148.5 mA and V_{SA} = -2 V at 100°C. (b) Average RIN for the whole optical comb shown in (a) from 0.5 to 10 GHz.

the range of 3.5 nm to 4.7 nm, and it is interesting to observe a very narrow comb bandwidth at 80°C. This phenomenon is still under investigation and possibly related to a combined effect of the cavity design, driving condition, and temperature-dependent tuning of the gain and absorption magnitude at the lasing wavelength. Further improvement of the comb bandwidth could be achieved by using chirped QDs [99], QD intermixing [100], and hybrid quantum well/QD structures [101]. Also, as expected, the corresponding number of comb teeth as a function of temperature shows a similar trend as the comb bandwidth. As seen, even at 120°C, it can still obtain >20 comb lines.

2.3.3 Feasibility for indoor RoF system

To evaluate the suitability of the developed QD MLL employed as an uncooled frequency comb source for phase-coherent DWDM multi-channel indoor RoF systems, the comb spectrum and the RIN are characterized at a high temperature of 100°C. Figure 2.5(a) shows the coherent comb spectrum, which exhibits a center lasing wavelength of ~1349 nm and a -6 dB comb bandwidth of 4.81 nm (under the bias conditions of I_{gain} = 148.5 mA and V_{SA} = -2 V), providing a maximum of 31 potential channels with an OSNR of more than 36 dB [0.1 nm amplified spontaneous emission noise bandwidth]. Figure 2.5(b) shows the RIN spectrum in the frequency range from 0.5 GHz to 10 GHz, where a low average RIN value of less than -146 dBc/Hz was achieved. The measured average absolute power per channel within the -6 dB comb bandwidth is ~ -18 dBm at 100°C, which is comparable to previous observations measured at room temperature [84]. The measured multiple tones with stable adjacent spacing and low RIN suggest the feasibility of the fabricated device for phase-coherent DWDM transmissions and pure RF carrier generation. To estimate the actual transmission capacity of this comb source at 100°C, a system-level wavelength-division multiplexing experiment employing an advanced modulation format with direct detection is still needed, but as a guideline, an anticipated transmission capacity of over 3.4 Tbps could be realized by employing 31 tones as optical carriers combined with a 28 GBaud 4-level pulse amplitude modulation format [84, 85].

2.4 Conclusion

We have developed a frequency comb source based on a passively mode-locked InAs QD laser that has achieved an ultra-stable repetition rate (corresponding to mode spacing between adjacent tones in the frequency domain) over the widest temperature range yet reported for any type of MLL, due to the high dot density and engineered quantized energy difference between the GS and the ES1. The QD MLL comb source operates in O-band and exhibits stable mode-locking at a fundamental repetition rate of 25.5 GHz with pulse widths of less than 9 ps at temperatures ranging from 20°C to 120°C. We have shown that the tone frequency spacing is nearly unaltered (0.07 GHz) with increasing operating temperature and that stable mode-locking over an 100°C temperature range can be simply achieved (with the absorber reversed biased at a constant voltage) by changing only the biasing conditions of the gain section. The QD comb source shows a relatively broad, coherent comb bandwidth (with a -6 dB bandwidth of 4.81 nm, offering a maximum of 31 optical channels) at 100°C with a low average RIN value of less than -146 dBc/Hz, making it feasible to handle a multi-Tbps transmission capacity and stable RF carrier generation. The findings pave the way for utilizing ultrastable, easy-operating, uncooled QD MLLs as efficient frequency comb sources for high-bandwidth, large-scale, low-cost phase-coherent DWDM multi-channel indoor RoF systems.

Chapter 3

Optical Generation/Detection of Broadband Radio-frequency Orbital Angular Momentum Modes

Due to the inherent orthogonality between different OAM modes, a new spatial multiplexing degree of freedom can be opened by establishing communication channels of the same frequency carried by different OAM modes, bringing a huge increase in the spectral efficiency and the system capacity. Therefore, OAM multiplexing techniques have the potential to solve the problem of RF spectrum scarcity. The generation of radio-frequency orbital angular momentum (RF-OAM) modes requires broadband phase shifters that provide constant phase shifts over a large frequency band. However, traditional RF phase shifters are difficult to meet the demand due to their bandwidth limitation. Luckily, microwave photonic techniques can be used to perfectly realize such broadband phase shifters. Moreover, RF phase shifters enabled by photonic techniques can be integrated with other photonic devices on a photonic integrated circuit, providing complete functions of RF carrier generation, signal modulation, frequency upconversion, etc... Finally, a complete data modulated RF-OAM multiplexed RoF link can be achieved.

In this chapter, a novel electrically-controlled optical broadband phase shifter (ECO-BPS) is proposed and experimentally investigated for broadband RF-OAM mode generation. Based on the proposed ECO-BPS and a 17-element circular antenna array, the effect of the phase error on the OAM mode quality is studied by comparing the OAM modes respectively synthesized by three phase schemes: ideal phase shifts, ECO-BPS phase shifts, and ideal optical true time delay (OTTD) phase shifts. In addition, the crosstalk caused by the phase error in applications of OAM modes multiplexing is investigated in a Dammann vortex grating-based OAM modes demultiplexing system. All experimental and numerical simulation results demonstrate the feasibility of the ECO-BPS in broadband RF-OAM applications.

3.1 State-of-the-art and the proposed approach

3.1.1 State-of-the-art

With rich orthogonal OAM modes, EM waves have the potential to carry much more channels at the same frequency, which could greatly improve the spectrum efficiency [50, 102]. Therefore, in the optics and radio regimes, OAM modes multiplexing has recently been widely considered for high-capacity communications [103, 104].

For generating OAM modes, spiral phase plates (SPPs) are useful in both optical and RF domain [105]. In the RF regime, circular antenna arrays (CAAs) can also be used to excite OAM modes [106]. Compared with the method using SPPs, which can only generate fixed OAM modes, a CAA can generate different OAM modes by correctly controlling the radiation phase of each antenna. Therefore, CAAs are much more flexible and feasible in RF-OAM applications. In order to obtain highly pure RF-OAM modes with a CAA, reconfigurable phase shifters with low phase error in a large bandwidth are required. However, RF phase shifters implemented in the electronic domain usually have the disadvantages of limited bandwidth, large size, and phase-frequency dependence. Therefore, researchers began to look for solutions in the field of optics. OTTD technology, which is usually used for RF beam steering [107], has been proposed to realize phase shifters for RF-OAM modes generation [108, 109]. OTTD is useful in beam steering because it provides a constant time delay for each spectral component, which corresponds to a phase shift varying with the frequency in order to maintain the pointing of the beam over a large bandwidth. However, this property is harmful in broadband RF-OAM applications, where in order to maintain the OAM modes over a large bandwidth, it is necessary to have the same phase shifts at different frequencies. Microwave photonic signal processing technology provides better solutions for high-performance RF phase shifters [110]. Unprecedented features, such as large operation bandwidth, compact size, ultra-low loss, inherent instantaneous processing, and immunity of EM interference, are enabled by photonics technologies. Many microwave photonic-based signal processors and phase shifters have been proposed [111–115], in which polarizers and Mach-Zehnder modulators are used to realize broadband RF phase shifters. All of these designs have excellent phase shift stability and large operating bandwidth.

3.1.2 The proposed approach

In this chapter, first we propose a novel ECO-BPS based on a parallel Mach-Zehnder modulator (P-MZM) for broadband RF-OAM modes generation. This ECO-BPS was briefly discussed in our previous work [116]. Here the comprehensive analysis is presented. In our design, the phase shift is controlled by adjusting only direct-current (DC) bias, which makes the proposed phase shifter simpler and easier to integrate. With electrical control, the inherent broadband and low-loss features of the ECO-BPS make it promising for future broadband RF-OAM modes generation. Secondly, the measured phase shifts of the ECO-BPS are applied to a 17-element circular antenna array to synthesize $l = 1$ OAM beams in the broadband from 12 to 20 GHz. The generated OAM patterns are then compared with the patterns synthesized by ideal phase shifts and ideal OTTD phase shifts in terms of amplitude profiles, phase front profiles, and spiral spectrum. Through these comparisons, the effect of the phase error on the quality of the OAM mode is investigated. Thirdly, to further investigate the crosstalk caused by the phase error in applications of OAM modes multiplexing, a 1×2 Dammann vortex grating [117] based OAM modes demultiplexing system is designed to quantify the crosstalk of $l = \pm 1$ multiplexed OAM modes, which are synthesized by the previous three kinds of phase shifts, respectively, in the broadband from 12 to 20 GHz. The crosstalk results obtained from the demultiplexing system agree very well with the spiral spectrum theory. All the numerical simulations show that highly pure OAM modes can be generated for broadband RF signals by using the ECO-BPS.

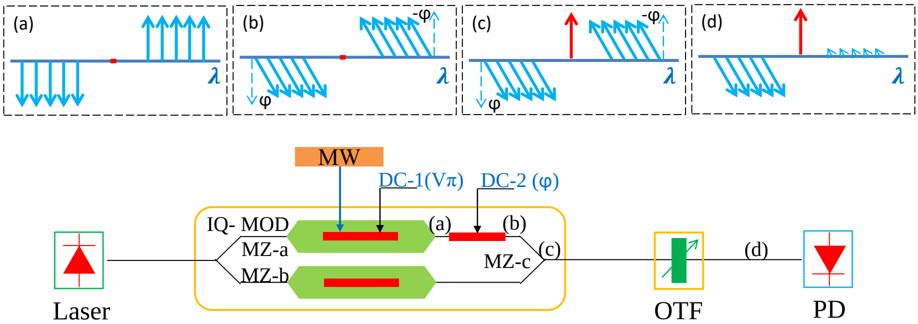

Figure 3.1: Principle of the proposed electrically-controlled optical broadband phase shifter. DC: direct-current, IQ-MOD: in-phase/quadrature modulator, MW: microwave signal, MZ-a/b/c: Mach-Zehnder modulator-a/b/c, OTF: optical tunable filter, PD: photo-diode.

3.2 Electrically-controlled optical broadband phase shifter

3.2.1 Operation principle

In this section, the detailed mathematical expressions of the proposed ECO-BPS are derived. The ECO-BPS, which includes a laser, an optical in-phase/quadrature modulator (IQ-MOD), an optical tunable filter (OTF), and a photo-diode (PD), is schematically shown in Figure 3.1. The laser signal (optical carrier) is modulated by the microwave signal in the Mach-Zehnder modulator MZ-a and finally detected by a PD. This link can be easily integrated into a small photonic chip based on the generic foundry approach [118]. The optical carrier can be expressed as:

$$E(t) = E_0 \exp(j\omega_0 t) \tag{3.1}$$

where E_0 and ω_0 represent the optical carrier's amplitude and angular frequency, respectively. The optical carrier is then split into two sub-MZMs (MZ-a and MZ-b). MZ-a operates in the pull-push mode with DC bias V_π. The microwave signal, used to modulate the optical carrier on MZ-a, can be described as:

$$E_{am}(t) = E_m \cos(\omega_m t) \tag{3.2}$$

where E_m and ω_m represent the amplitude and the angular frequency of the microwave signal, respectively. For simplicity, the microwave signal is written in its complex expression:

$$E_{am}(t) = E_m \exp(j\omega_m t) \tag{3.3}$$

With the high order ($> 1^{st}$) sidebands ignored, the optical signal after MZ-a can be expressed as:

$$\begin{aligned} E_a(t) = &-\frac{1}{2}E_0 J_{+1}(m)\exp(j\omega_0 t + j\omega_m t) \\ &+\frac{1}{2}E_0 J_{-1}(m)\exp(j\omega_0 t - j\omega_m t) \end{aligned} \tag{3.4}$$

where $m = \pi E_m / V_\pi$ is the modulation depth, $J_{+1}(m)$ and $J_{-1}(m)$ denote the 1^{st} kind Bessel functions of order ± 1. The optical spectrum of the modulated signal after MZ-a is shown in Figure 3.1(a) schematically, where the arrows represent different spectral components of the microwave signal modulated on the optical carrier.

Here MZ-b is used to reserve the optical carrier; thus, a single waveguide can replace MZ-b for this purpose. No DC bias is applied to MZ-b to allow its maximum transmission. The optical signal after MZ-b can be expressed as:

$$E_b(t) = \frac{1}{2}E_0 \exp(j\omega_0 t) \tag{3.5}$$

The DC bias of MZ-c is used to tune the phase of the modulated optical signal generated by MZ-a. After MZ-c, optical signals from MZ-a/b are combined with the additional delay τ, which is induced in MZ-c. The result can be written as:

$$\begin{aligned} E_{out}(t) = &-\frac{1}{2}E_0 J_{+1}(m)\exp[j(\omega_0 + \omega_m)(t+\tau)] \\ &+\frac{1}{2}E_0 J_{-1}(m)\exp[j(\omega_0 - \omega_m)(t+\tau)] \\ &+\frac{1}{2}E_0 \exp(j\omega_0 t) \end{aligned} \tag{3.6}$$

Then the lower frequency sideband (upper wavelength sideband) is filtered out by an optical notch filter (an OTF is used here), and the optical signal can be expressed as:

$$\begin{aligned} E_{out}(t) = & -\frac{1}{2}E_0 J_{+1}(m)\exp[j(\omega_0+\omega_m)(t+\tau)] \\ & +\frac{1}{2}E_0\exp(j\omega_0 t) \end{aligned} \tag{3.7}$$

Equation (3.7) can be rewritten as:

$$\begin{aligned} E_{out}(t) = & -\frac{1}{2}E_0 J_{+1}(m)\exp[j(\omega_0+\omega_m)t+\theta(\omega_m)] \\ & +\frac{1}{2}E_0\exp(j\omega_0 t) \\ \theta(\omega_m) = & j\omega_0\tau(1+\frac{\omega_m}{\omega_0}) \end{aligned} \tag{3.8}$$

Equation (3.8) shows that the additional phase shift varies with the frequency of the modulated microwave signal. However, since $\omega_0 \gg \omega_m$, equation (3.8) can be further simplified as:

$$\begin{aligned} E_{out}(t) = & -\frac{1}{2}E_0 J_{+1}(m)\exp[j(\omega_0+\omega_m)t+j\omega_0\tau] \\ & +\frac{1}{2}E_0\exp(j\omega_0 t) \end{aligned} \tag{3.9}$$

The optical signal is then detected by a photo-diode (PD), and the resulting current signal can be written as:

$$\begin{aligned} I(t) = & \mu\times\left\{-\frac{1}{2}E_0 J_{+1}(m)\exp[j(\omega_0+\omega_m)t+j\omega_0\tau] \right. \\ & \left. +\frac{1}{2}E_0\exp(j\omega_0 t)\right\} \\ & \times\left\{-\frac{1}{2}E_0 J_{+1}(m)\exp[j(\omega_0+\omega_m)t+j\omega_0\tau] \right. \\ & \left. +\frac{1}{2}E_0\exp(j\omega_0 t)\right\}^* \\ = & \underbrace{\frac{1}{4}\mu E_0^2\left(J_{+1}^2(m)+1\right)}_{DC}-\underbrace{\frac{1}{2}\mu E_0^2 J_{+1}(m)\cos(\omega_m t+\omega_0\tau)}_{microwave} \end{aligned} \tag{3.10}$$

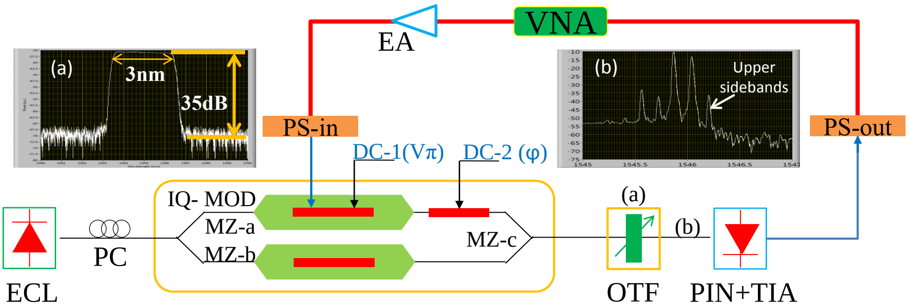

Figure 3.2: Experimental setup of the proposed electrically-controlled optical broadband phase shifter. DC: direct-current, EA: electrical amplifier, ECL: external cavity laser, IQ-MOD: in-phase/quadrature modulator, MZ-a/b/c: Mach-Zehnder modulator-a/b/c, OTF: optical tunable filter, PC: polarization controller, PIN: p-i-n diode, PS-in/out: phase shifter-in/out, TIA: transimpedance amplifier, VAN: vector network analyzer

The microwave signal at the output of the proposed broadband phase shifter results in a time-delayed replica of the original signal (equation (3.2)). The broadband feature is guaranteed by the huge frequency difference between the optical carrier and the microwave signal.

Here a comparison between the ECO-BPS and the OTTD phase shifter proposed in [119] is carried out. For the OTTD case, with negligible dispersion, the phase of the modulated microwave signal can be expressed as:

$$
\begin{aligned}
I_{ottd}(t) &= I_{DC} + I_{MW}\cos\left(\omega_m\left(t+\tau_{ottd}\right)\right) \\
&= I_{DC} + I_{MW}\cos\left(\omega_m t + \theta_{ottd}\left(\omega_m\right)\right) \\
\theta_{ottd}\left(\omega_m\right) &= \omega_m \tau_{ottd}
\end{aligned}
\tag{3.11}
$$

where I_{DC} and I_{MW} denote the DC and the current of the detected microwave signal after a PD. As shown in equation (3.11), the phase deviation regarding different frequencies of the modulated microwave signal can not be ignored. Compared with equation (3.10), it is obvious that the broadband feature of the ECO-BPS is guaranteed because the phase shift is done in the optical domain.

3.2.2 Measurement of ECO-BPS

The experimental setup of the ECO-BPS is shown in Figure 3.2. An optical carrier from an external cavity laser (ECL) with 12 dBm optical power is sent to a P-MZM (Fijitsu FTM7961) via a polarization controller (PC). The integrated structure of P-MZM can guarantee its high environment robustness. As shown in Figure 3.2, MZ-a is biased at its null point (V_π) via DC-1 for microwave signal modulation. Then a phase shift (φ) is optically applied to the optical signal via MZ-c by electrically tuning the bias voltage of DC-2. The optical carrier from MZ-b is then combined with the optical signal from MZ-a via MZ-c. To avoid power imbalance for different phase shifts, the upper sidebands are filtered out with the optical spectrum as shown in Figure 3.2(b). The measured transmission profile of the OTF (Santec OTF950) is shown in Figure 3.2(a). The measured roll-off slope of the employed OTF is 68 dB/nm. The beating between the optical carrier and the lower sidebands reconstructs the microwave signal after the photo-diode (PIN+TIA). The input and output of the ECO-BPS are labeled as PS-in and PS-out in Figure 3.2.

The phase shift performance of the ECO-BPS is evaluated by an electrical vector network analyzer (VNA). The sinusoidal stimulus signal from the output of the VNA is applied to PS-in of the ECO-BPS. The retrieved signal from PS-out of the ECO-BPS is then fed to the input of the VNA. Such signal is further compared with its local replica to obtain the amplitude/phase responses (versus frequency). The frequency of stimulus sinusoidal signal is swept from 12 GHz to 20 GHz. Its lower boundary depends on the filter slope of OTF, while its upper boundary depends on the bandwidth of the engaged electro-optical devices. We plan to generate seventeen progressive phase shifts from $-\pi$ to π. But in the employed VNA, the measured phase will jump from $-\pi$ to π or π to $-\pi$ when the phases are close to $-\pi$ or π. Thus, we generated 16 phase shifts by applying 16 DC levels to the ECO-BPS. The measured frequency-phase curves are shown in Figure 3.3(a). The 17^{th} phase shift is synthesized by fitting the measured data. It is noticed that the ripples at the lower frequencies are stronger than the ones at the higher frequencies since the upper sidebands at the higher frequency can be better filtered out. The frequency-averaging of the measured phase shifts is shown in Figure 3.3(b), which indicates a good agreement between the measured phase shifts and the applied voltages. Now we focus on the variation of the measured phase shifts towards the frequency. As shown in Figure 3.3(c), the phase error variations in the middle range (7V-9V) are smaller than others, mainly because the VNA is calibrated at 8V. The maximum standard deviation of the measured phase error is 3.44° from 12 GHz to 20 GHz. There are three

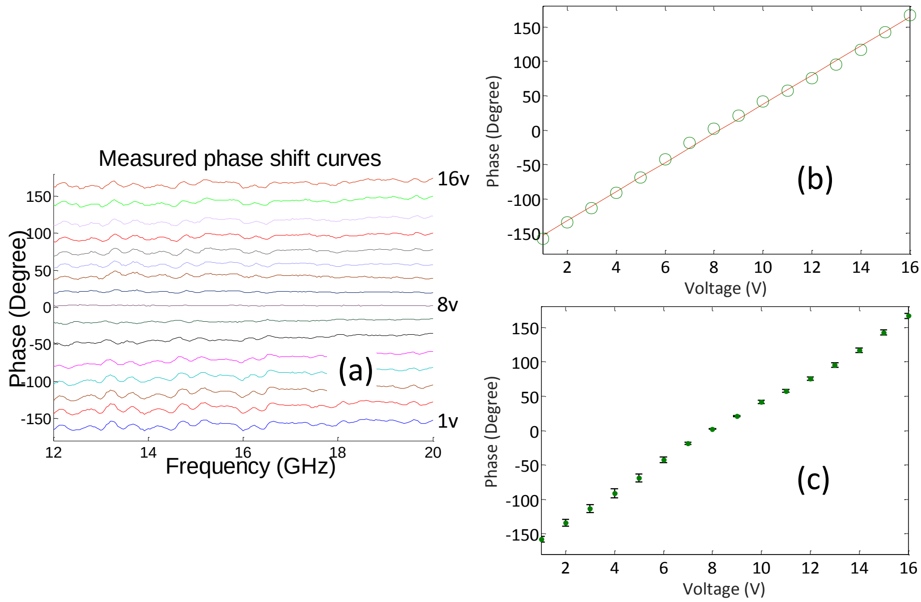

Figure 3.3: Measured frequency-phase curve and voltage-phase curve, including (a) the measured phase response with different applied bias voltages, (b) the frequency-averaging of (a) and its fit curve, (c) the variance of (b).

main possible sources for the phase error. One is the phase variation induced by residual upper sidebands. The second is the random phase error induced by noise. And the last is the phase error caused by the time variation of OTF. By integrating OTF and P-MZM in a single chip, the first and third sources can be largely reduced.

3.3 OAM mode analysis

The numerical analyses in the following parts are based on Rayleigh-Sommerfeld diffraction theory [120], which provides very accurate results if two conditions are met: 1) the diffracting aperture must be large compared with a wavelength, and 2) the diffracting fields must not be observed too close to the aperture. These conditions are well satisfied in the situations treated here.

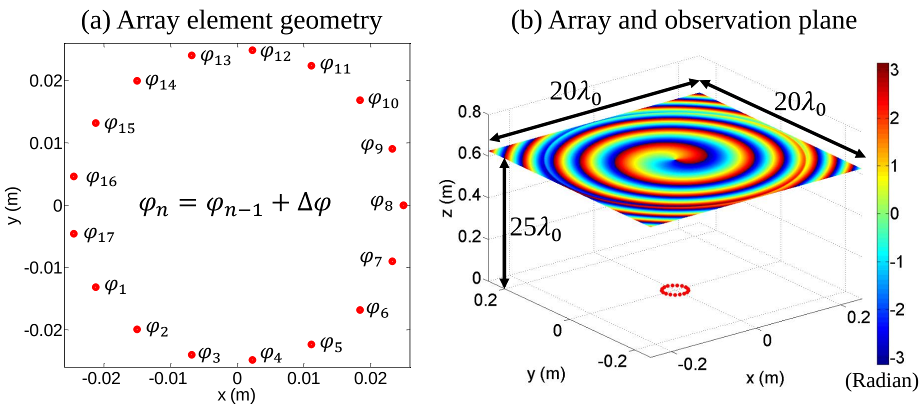

Figure 3.4: (a) The geometries of the circular antenna array used for OAM modes generation/detection and (b) its observation plane.

3.3.1 OAM modes generation and detection based on CAA

A CAA for OAM mode generation with geometric and phase configurations is shown in Figure 3.4(a). Seventeen ideal short dipoles with progressive phases are distributed equidistantly around a circle. In principle, the number of antenna elements (N) depends on the largest OAM mode (l_{max}) and can be expressed as:

$$N > 2|l_{max}| \tag{3.12}$$

The progressive phase shifts are added to the RF signals before being launched to the CAA as shown in Figure 3.4(a). The unit phase shift is given by:

$$\Delta\varphi = -2\pi l/N \tag{3.13}$$

where l is the excited OAM mode. As shown in Figure 3.4(b), an observation plane for OAM modes monitoring is located $25\lambda_0$ above the CAA plane, and $\lambda_0 = 0.025m$ is the wavelength of the reference frequency (12 GHz). The size of the observation plane is $20\lambda_0$ for both x and y directions. The phase fronts of the excited OAM modes are intersected and monitored on the observation

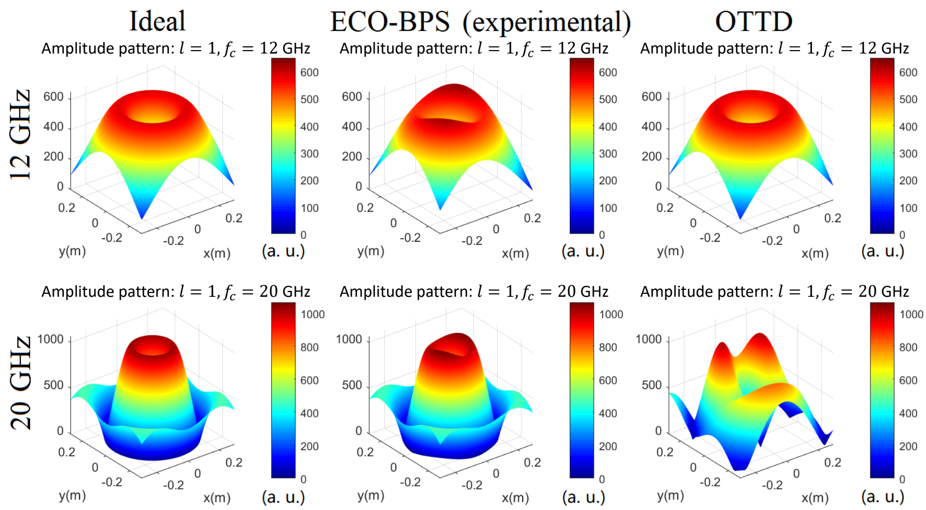

Figure 3.5: 3D Amplitude patterns of $l = 1$ OAM modes based on ideal phase shifts, ECO-BPS phase shifts and ideal OTTD phase shifts.

plane. The excited OAM modes can be flexibly configured by controlling the phases (of all spectral components) of the RF signals. Since different OAM modes are all orthogonal, a generated OAM mode can be separated from the multiplexed OAM modes by a CAA with the opposite phase configurations. The purity of generated/detected OAM modes is limited by imperfect phase shifts (phase error). Thus a broadband phase shifter with low phase error at all spectral components is required.

3.3.2 OAM mode synthesis

Based on the CAA mentioned above, $l = 1$ RF-OAM beams are respectively synthesized by three phase schemes: ideal phase shifts, ECO-BPS phase shifts, and ideal OTTD phase shifts, in the broadband from 12 GHz to 20 GHz. The OTTD phase shifts are set to be the same as the ideal case at 12 GHz. OAM modes of the three cases are then compared in terms of amplitude profiles and phase front profiles.

The synthesized three-dimensional (3D) amplitude patterns are shown in Figure 3.5, for the frequency of 12 GHz and 20 GHz. The ideal amplitude pat-

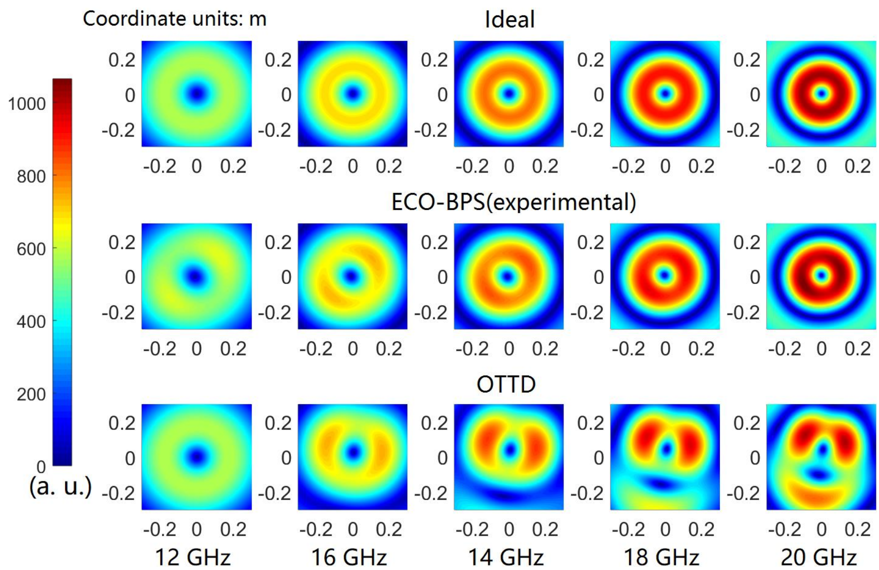

Figure 3.6: Amplitude patterns of $l = 1$ OAM modes sliced at observation plane.

tern looks like a vortex with a singular point in its center. The ideal amplitude patterns at 12 GHz and 20 GHz are different due to their wavelength difference. In general, the flatness and the divergence of amplitude patterns indicate the quality of the generated OAM modes. As shown in Figure 3.5, the quality of OAM modes synthesized by ECO-BPS phase shifts is similar with the ideal ones, at both 12 GHz and 20 GHz. However, the OTTD one exhibits a much worse quality at 20 GHz, because each antenna element's phase relation is no longer correct in the OTTD phase scheme.

In Figure 3.6, the 2D amplitude patterns sliced at the observation plane are shown from 12 GHz to 20 GHz, with a step of 2 GHz. The quality of OAM modes synthesized by the ECO-BPS is slightly worse than the ideal ones, mainly due to the variation of the measured phase shifts. The quality of the modes generated with ideal OTTD phase shifts exhibits a degradation as the frequency increases. At the frequencies of 18 GHz and 20 GHz, the vortex even breaks, which indicates the partial deterioration of OAM modes.

The phase fronts of all the three cases sliced at the observation plane are shown in Figure 3.7. For the ideal case, the phase shifts are perfectly allocated for both 12 GHz and 20 GHz RF signals. Therefore, the rotating phase fronts

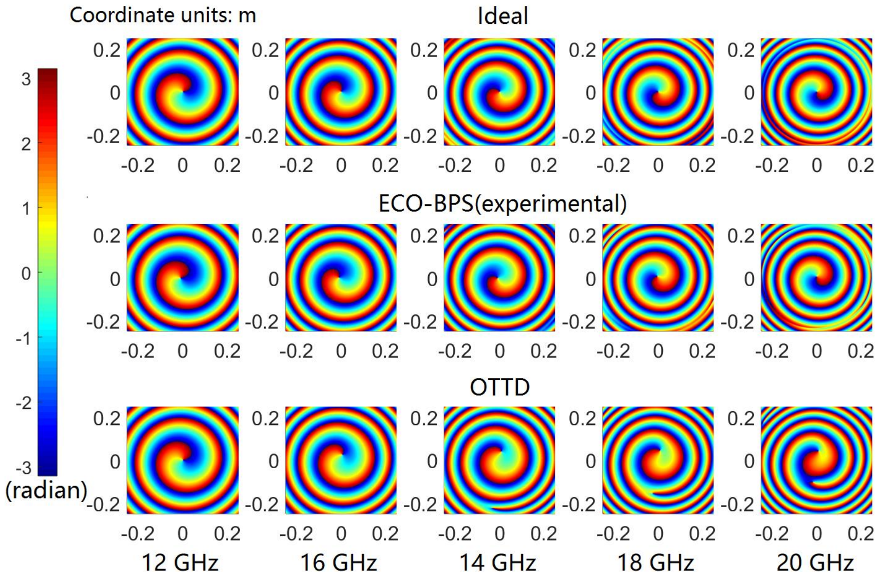

Figure 3.7: Phase patterns of $l = 1$ OAM modes sliced at observation plane.

are perfectly observed with a clear singular point in the center, which exhibits a highly pure $l = 1$ OAM mode. The ECO-BPS case has a very similar behavior as the ideal one, showing its feasibility for broadband operation. For the OTTD case, the delays for each antenna element are calculated based on the ideal phase shifts at 12 GHz. Thus, its phase front at 12 GHz is the same as the ideal case. However, the OTTD delays will cause linearly increasing phases at 20 GHz, resulting in the disorder of phase fronts shown in Figure 3.7. Such disorder will reduce the purity of the $l = 1$ OAM mode and raise crosstalk to other OAM modes.

3.3.3 Spiral spectrum

To accurately elucidate the disorder of the synthesized OAM beams, the spiral spectrum [121] of $l = 1$ OAM modes synthesized by the three kinds of phase shifts is calculated and shown in Figure 3.8. It can be seen the ideal case has pure $l = 1$ OAM modes. For the ECO-BPS case, at all frequencies, about 99% of the beam energy is carried by the $l = 1$ OAM mode. Highly pure $l = 1$ OAM mode

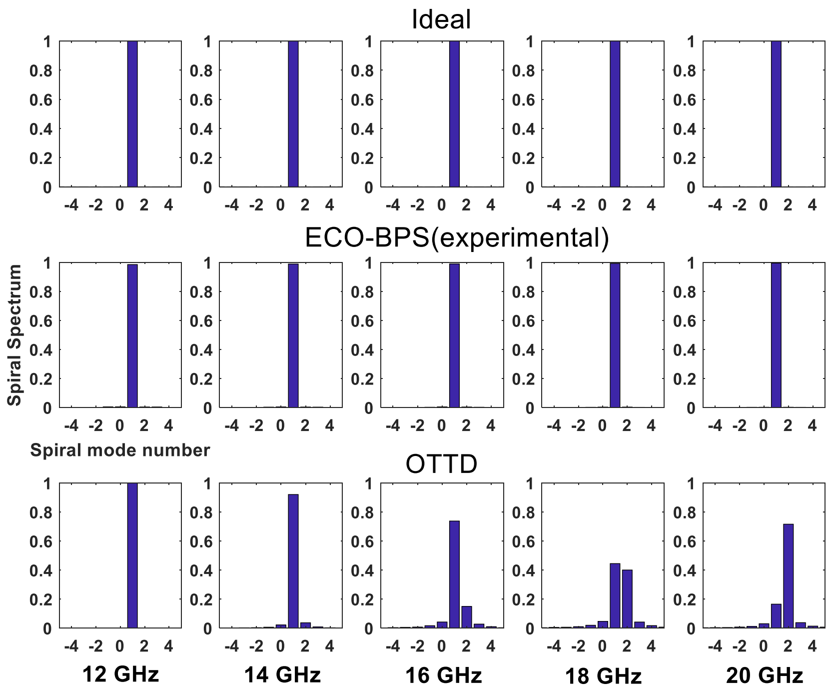

Figure 3.8: The spiral spectrum of $l = 1$ OAM modes sliced at observation plane.

is obtained in the entire bandwidth. For the OTTD case, since the phase error increases linearly with the frequency, the generated OAM mode gradually drifts from $l = 1$ to $l = 2$ as the frequency increases. Actually, at 24 GHz, the total phase shift of the OTTD case will be 4π, which corresponds to an $l = 2$ OAM mode, meaning the desired $l = 1$ OAM mode is totally gone. The spiral spectrum indicates that OTTD phase shifts can only be used in a narrow bandwidth for OAM beam generation, but the ECO-BPS can be used to generate highly pure broadband RF-OAM modes.

3.4 Crosstalk investigation

Based on the previous discussions, it can be seen the phase error causes OAM modes diffusion, which will lead to crosstalk in applications of OAM modes

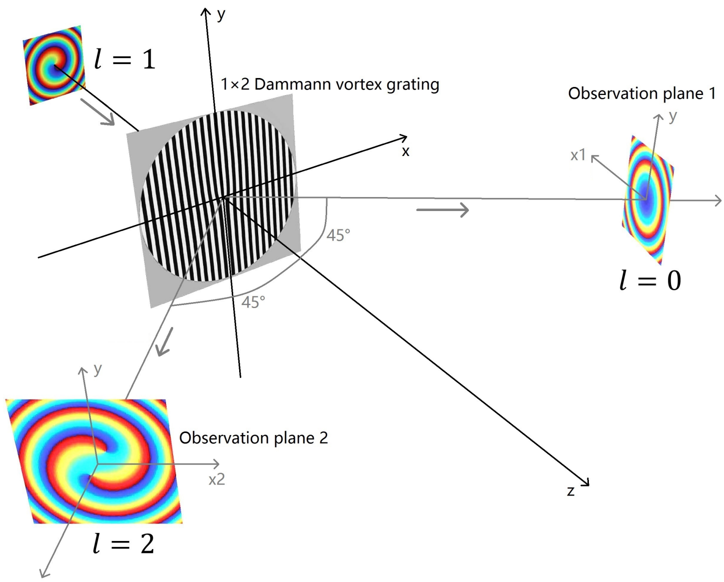

Figure 3.9: Dammann vortex grating-based OAM modes demultiplexing system.

multiplexing. In order to have a better understanding of the crosstalk, a 1×2 Dammann vortex grating-based OAM modes demultiplexing system, as shown in Figure 3.9, is designed to investigate the crosstalk of $l = \pm 1$ multiplexed OAM modes by numerical simulations. The system configuration is as follows: The distance from OAM generation to the grating is $25\lambda_0$. The grating diameter is set to $40\lambda_0$ to ensure a complete beam pass. The grating diffraction angle is set to 45° to avoid interference between two diffraction directions. The diffraction distance is set to 500m to obtain far fields. All simulations are done in a free space background.

As shown in the example of Figure 3.9, when an $l = 1$ OAM beam illuminates the 1×2 Dammann vortex grating, which has an intrinsic topological charge of 1, $l = 0$ OAM beam and $l = 2$ OAM beam can be obtained respectively in its ±1 main diffraction directions. The corresponding phase patterns of $l = 0$ OAM mode and $l = 2$ OAM mode can be observed on observation plane 1 and observation plane 2, respectively. With an input $l = -1$ OAM beam, $l = -2$ OAM mode is observed on observation plane 1 and $l = 0$ OAM mode is observed on observation plane 2. Therefore, for an incident $l = \pm1$ multiplexed OAM beam, the superposition

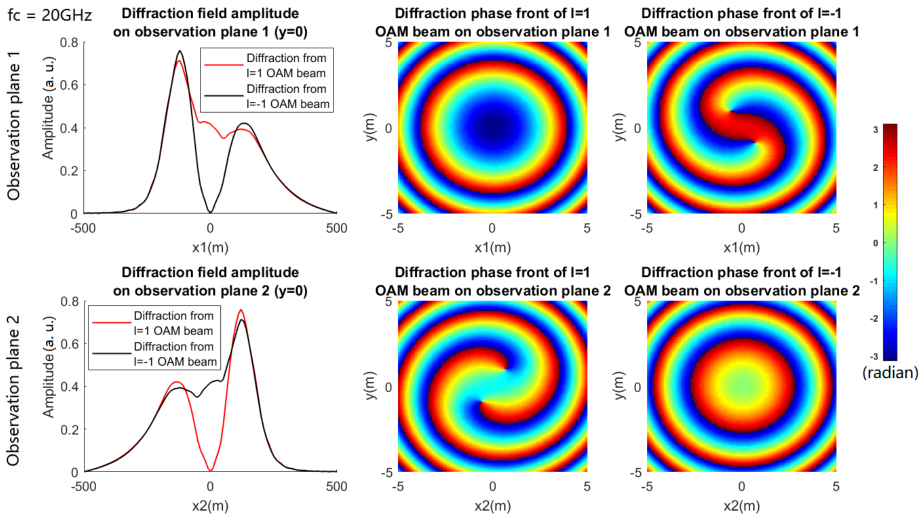

Figure 3.10: Demultiplexing results of $l = \pm 1$ multiplexed OAM beam synthesized by ideal phase shifts at 20 GHz.

of $l = 0$ mode and $l = -2$ mode is obtained on observation plane 1, and the superposition of $l = 2$ mode and $l = 0$ mode is obtained on observation plane 2. The two $l = 0$ modes are the demultiplexed signals. In the ideal case, there is a singular point in the center of a high-order ($l \neq 0$) OAM beam, so only the $l = 0$ beam can be detected at the center of an observation plane. Thus, at the center of an observation plane, the field amplitude ratio of high-order ($l \neq 0$) OAM mode to $l = 0$ OAM mode is defined as crosstalk here.

Figure 3.10 shows the demultiplexing results of $l = \pm 1$ multiplexed OAM beam synthesized by ideal phase shifts at 20 GHz. From the amplitude curve, it can be seen the amplitude pattern of the diffraction beam is distorted. This is because the grating diffraction angle is large (45°). However, the singular point can still be observed clearly at the center of each observation plane. In addition, as expected, high-quality phase patterns of $l = \pm 2$ and $l = 0$ are obtained on the two observation planes. Thus the demultiplexing is accomplished. Based on the results, the calculated crosstalk is very small in the ideal case, and it can be considered the system resolution limit.

In Figure 3.11, crosstalk curves of the three kinds of phase shifts are shown from 12 GHz to 20 GHz with a step of 2 GHz. The crosstalk maintains a very

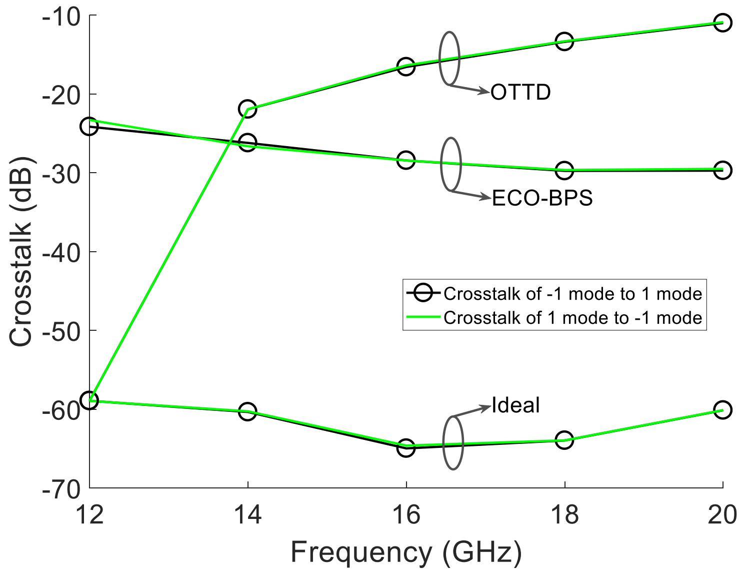

Figure 3.11: Crosstalk based on ideal phase shifts, ECO-BPS phase shifts and ideal OTTD phase shifts.

small value (system resolution limit) for the ideal case, around -62 dB. Due to the phase error, the crosstalk of the ECO-BPS case increases to around -27 dB in the entire bandwidth. For the OTTD case, at 12 GHz, its phase shifts are the same as the ideal case, so they have the same small crosstalk. However, as the frequency increases, the crosstalk of the OTTD case increases rapidly due to the phase-frequency dependence of the OTTD phase shifts. Starting from 14 GHz, the crosstalk of the OTTD case becomes significantly larger than that of the ECO-BPS case. It should be noticed that the OTTD phase shifts used here are ideal, only the inherent phase error is considered.

On the other hand, the crosstalk can also be calculated by using the spiral spectrum, which is discussed in Section 3.3.3. The crosstalk of the $l = 1$ ($l = -1$) mode to the $l = -1$ ($l = 1$) mode is derived from the $l = -1$ ($l = 1$) sidelobe. A comparison is made in Figure 3.12. It can be seen that the two crosstalk results respectively obtained from the demultiplexing system and the spiral spectrum theory agree very well. This suggests the demultiplexing system does distinguish the desired OAM mode. The ideal case is not included in the comparison

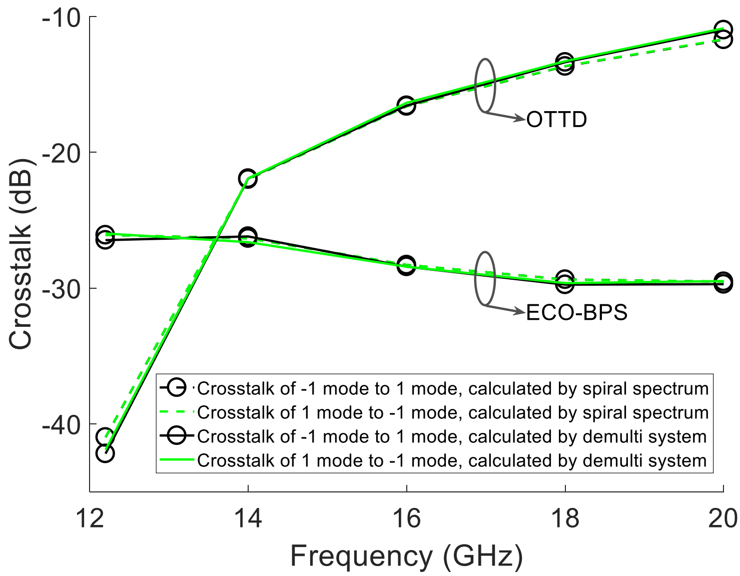

Figure 3.12: Comparison of the crosstalk respectively calculated by using the demultiplexing system and the spiral spectrum.

because of the resolution limit of the demultiplexing system. Although only the case of $l = \pm 1$ OAM modes demultiplexing is analyzed here, according to the spiral spectrum, we can infer that there is larger crosstalk among other modes for the OTTD scheme.

3.5 Conclusion

A novel ECO-BPS is proposed to generate broadband RF-OAM modes. The standard deviation of the measured phase error of the ECO-BPS is 3.44° from 12 GHz to 20 GHz. By comparing the OAM modes respectively synthesized by ideal phase shifts, ECO-BPS phase shifts, and ideal OTTD phase shifts in terms of amplitude profiles, phase front profiles, spiral spectrum, and crosstalk, the feasibility of the ECO-BPS in broadband RF-OAM applications is demonstrated.

Chapter 4

2D Infrared Beam Steering Enabled by a Passively Field-programmable Metasurface

With the explosive growth of the number of broadband mobile devices and the rapid development of the Internet of Things [122], the booming demand for high-speed wireless connectivity is challenging the existing radio wireless communication solutions, especially in indoor scenarios. The widely used wireless technology Wi-Fi suffers from a limited data rate because the data are modulated on a narrow band and transmitted at low carrier frequencies such as 2.4 GHz and 5 GHz. Moreover, this capacity is shared among multiple users. The latest IEEE 802.11ac standard provides a channel bandwidth of up to 160 MHz in the 5 GHz spectrum, with a physical-layer data rate of up to 6.93 Gbps [123]. Nevertheless, the radio spectrum is still overwhelmed by the ever-increasing high-speed connection demands.

To satisfy the demanding data rate beyond what RF communication can support, beam-steered infrared (IR) light communication (BS-ILC) is introduced [25, 35]. Optical beam steering is one of the main challenges in energy-efficient and high-speed BS-ICL. To date, active beam-steering schemes based on spatial light modulators (SLMs) or micro-electrical mechanical system (MEMS) mirrors, as well as the passive ones based on diffractive gratings, have been demonstrated for IR light communication. In this Chapter, first time to the best of our knowledge, an IR beam is steered by 49.8° on one side enabled by a passively field-programmable metasurface. By combining the centralized control of wavelength and polarization, a passive metasurface-based remote optical access point can two-dimensionally steer the IR beam to achieve full coverage of an area. The proposed system has the scalability to support multiple beams, flexibility to steer the beam, high optical efficiency, simple and cheap devices on remote sides, and centralized control (low maintenance cost), while it avoids disadvantages such as grating loss, small coverage area, and bulky size. Based on the proposed beam-steering technology, we also demonstrated a proof-of-concept experiment link with a data rate of 20 Gbps.

4.1 State-of-the-art and the proposed approach

4.1.1 State-of-the-art

Optical wireless communication (OWC) has recently attracted much interest due to the tremendous number of spectrum resources in the optical regime, which can provide ultra-high wireless capacity in an indoor environment and largely solve the shortage of radio spectrum resources [23]. Visible light communication (VLC) [27] and BS-ILC [25, 35] are the two main technical directions of OWC. VLC transports data over LED illumination systems, and multiple users share the VLC capacity. It provides access to a bandwidth of no less than 320 THz in the 400 nm-700 nm range [23]. BS-ILC uses well-directed narrow IR beams to establish point-to-point communication channels. Multiple users are served by a corresponding number of IR beams. Each user has an independent connection to the transmitter, which guarantees capacity and data safety. Besides, directed narrow IR beams can provide high energy efficiency. Furthermore, because a relatively high transmitted power of IR light is allowed in terms of eye safety, BS-ILC can achieve a very high data rate and system capacity. For VLC and BS-ILC, capacities >10 Gbps [26] and >400 Gbps [28] have been demonstrated in the laboratory, respectively.

However, as a prerequisite for BS-ILC, the 2D IR beam steering approach is still the main challenge towards the practical realization of BS-ILC. SLM-based [31, 124] and MEMS-mirror-based [125] active beam steering solutions have been proposed. When using MEMS-based mirrors, a large beam steering angle (~ 10°) can be achieved by mechanically tuning the small mirrors, but it is difficult to realize multi-beam operation because multiple steering elements are needed, resulting in complex control schemes and system configurations. For SLM-based approaches, the IR beam can be steered by electronically tuning the phase profile of the wavefront with the SLM. No mechanical movement is introduced. Hence, quick and stable steering can be realized. However, SLM-based systems are relatively bulky because complicated angle magnifiers are needed as the SLM itself can only provide a very limited steering angle ($\sim 3°$). Additionally, the grating loss is introduced by the SML, and the scalability towards many beams is also limited.

Passive beam-steering solutions [126–131] are therefore more accessible, in which the beam directions are mapped to the wavelengths. By inputting many wavelengths to the system through a fiber, the corresponding beam directions can be activated simultaneously. Gratings [126,127], phased arrays [128], grating couplers [129], and arrayed waveguide grating routers (AWGRs) [130,131] have been applied to realize fully passive 2D IR beam-steering systems. Among them, AWGR-based beam-steering modules [130, 131] have obvious advantages: a large 2D angular range of $18.6° \times 18.6°$, compact size, high efficiency, full area coverage, fast steering speed, and scalability to support multiple beams. In [131], an AWGR-based beam-steering system supporting 80 independent beams with a data rate per beam of 112 Gbps is demonstrated, which indicates a huge system capacity of 8.96 Tbps.

4.1.2 The proposed approach

Here, we present a novel solution to IR beam steering based on a passively field-programmable metasurface. Metasurfaces are an emerging approach to manipulating EM waves. They are generally created by assembling arrays of sub-wavelength resonators to provide complete control of the phase, amplitude, and polarization of EM waves [132–134]. Hence, actively tunable metasurfaces are widely considered for realizing beam steering [135–139]. Tunable metasurfaces can be dynamically controlled via external stimuli, which are usually electrical biases, laser pulses, or heat inputs. Owing to the sub-wavelength scale of the resonators, controlling every resonator is difficult, which would make the structure very complicated and hard to fabricate, particularly in the optical range. Therefore, tunable metasurface-based beam steering is usually realized at radio frequencies [138, 139]. In the optical range, controlling every resonator is unrealistic, yielding very limited beam steering [137]. On the other hand, beam steering based on a passive metasurface is proposed by Ding et al. [140]. Similar to the approach using grating, wavelength tuning is applied to change the beam direction. However, only the +1 diffraction order can be used in the phase gradient metasurface, while the other diffraction orders are strongly suppressed. Although high efficiency can be obtained, the steering angle is limited, and a very wide wavelength tuning range is needed (7.3° steering angle is achieved over a wide spectral range of 580-700 nm in [140]).

In our system, a polarization beam splitter based on a passive gap-surface plasmon metasurface (GSPM) is applied for 2D IR beam steering. GSPM has the advantages of high efficiency, excellent control over the reflected or transmitted light, and a simple manufacturing technique [141]. It has been used to realize numerous flat devices such as anomalous reflectors [142], focusing flat mirrors [143], phase modulators [144], holograms [145], polarisation beam splitters [146], metagratings [147], and OAM generators [52, 148, 149]. With the GSPM-based beam splitter and a simple liquid-crystal polarization controller, polarization-controlled beam steering can be realized. Together with an AWGR-based beam-steering module, a polarization-wavelength-controlled 2D IR beam-steering system is achieved. The new system keeps all the advantages of AWGR-based beam-steering approaches [130, 131], and additionally has polarization control capability. Hence, the coverage is greatly expanded. Furthermore, the grating loss existing in SLM-based and grating-based beam-steering approaches can be avoided by using the metasurface, which improves energy efficiency. Finally, a metasurface polarization beam splitter is designed, fabricated, and measured. With the fabricated metasurface chip, polarization-controlled 2D IR beam steering experiments are performed in C-band, and a 20-Gbps beam-steered IR wireless link is built over 1.2-m free space, which proves the feasibility of the proposed 2D IR beam steering system.

4.2 Operation principle

The proposed 2D IR beam-steering system is shown in Figure 4.1. It is composed of an AWGR-based beam-steering module [130, 131], a liquid-crystal polarization controller, and a metasurface polarization beam splitter. $M \times N$ outputs of the AWGR are connected to an $M \times N$ 2D fiber array. The output plane of the fiber array is placed in the object plane of a half lens. The output beams of the fiber array are first modulated by the liquid-crystal polarization controller to manipulate their polarization, following which they are deflected by the half lens. The deflected beams are then reflected by the metasurface polarization beam splitter, which is placed in the focal plane of the half lens. Both normal reflection and abnormal reflection occur on the surface of the metasurface po-

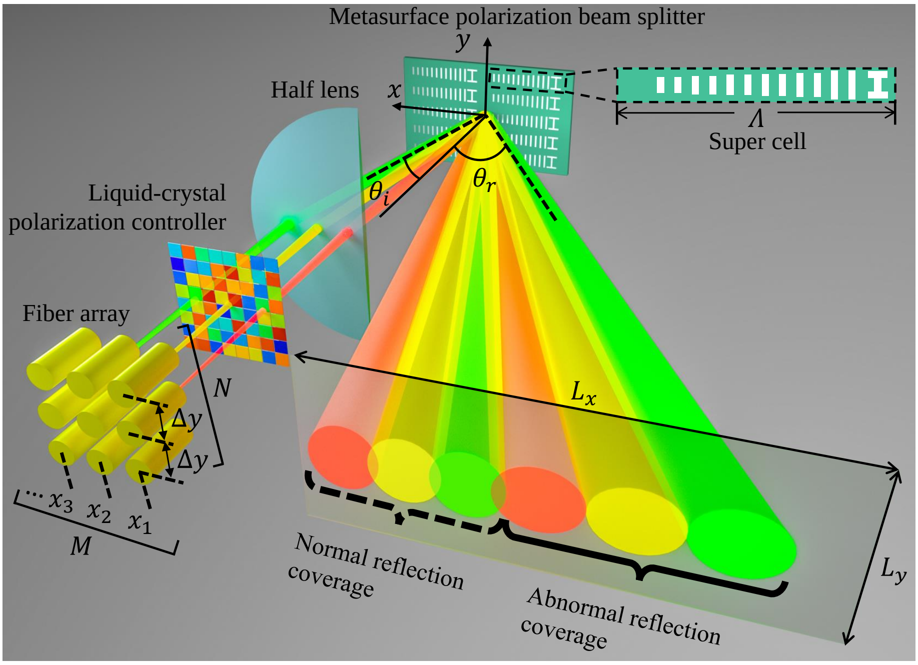

Figure 4.1: Architecture of the proposed metasurface-based 2D IR beam-steering system.

larization beam splitter; thus, the number of final output beams is doubled, and the total beam coverage area is greatly expanded (normal reflection coverage + abnormal reflection coverage).

The proposed beam-steering system has two tuning schemes: wavelength tuning and polarization tuning. By adjusting the input wavelength of the AWGR, one can control the position of the lighted fiber and then control the beam direction after the half lens, which further controls the emission directions of a pair of normally and abnormally reflected output beams. The polarization tuning is enabled by the liquid-crystal polarization controller and the metasurface polarization beam splitter. For a y-polarized incident beam, the metasurface polarization beam splitter generates a positive phase gradient along the negative x-direction; thus, the beam is abnormally reflected, as shown in Figure 4.1. The nonlinear relation between the abnormal reflection angle θ_r and the incident angle θ_i is $\sin\theta_r = \sin\theta_i + \lambda/\Lambda$, where λ is the wavelength and Λ is the length of

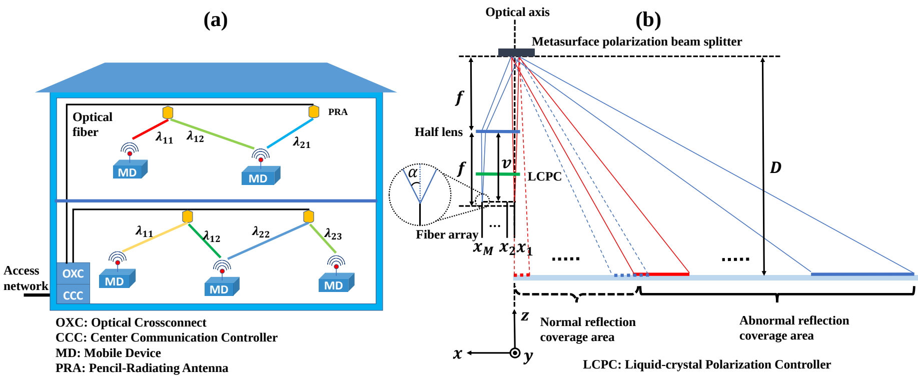

Figure 4.2: (a) Indoor beam-steered IR light communication network. (b) Schematic of the proposed 2D beam-steered IR light communication system.

the super cell of the metasurface polarization beam splitter, as shown in Figure 4.1. The $\theta_r - \theta_i$ relation implies a critical incident angle $\theta_{ic} = \arcsin(1 - \lambda/\Lambda)$. For an x-polarized incident beam, the metasurface polarization beam splitter acts as a mirror, and the beam is normally reflected. By adjusting the polarization of a fiber beam with the liquid-crystal polarization controller, one can control the power distribution between the corresponding normally and abnormally reflected output beams. Therefore, a wavelength-polarization-controlled 2D beam-steering approach is achieved.

In section 4.3, the system configuration is thoroughly discussed. The design and characterization of the metasurface polarization beam splitter are presented in detail in sections 4.4 and 4.5, respectively.

4.3 Design of the proposed 2D beam-steered IR light communication system

The concept of the indoor beam-steered IR light communication network is shown in Figure 4.2(a) [131]. In each room, several pencil-beam radiating antennas can provide high-speed connections to mobile devices with well-directed narrow IR beams. To cover the whole area, 2D IR beam steering is essential.

Figure 4.2(b), which is the $y = 0$ cross-section of Figure 4.1, schematically illustrates the configuration of the proposed 2D IR beam-steering system. The fiber array is placed away from the focus and closer to the lens. The distance between the output plane of the fiber array and the half lens is v, which defines the relative defocusing parameter $p = 1 - v/f$ $(0 \le p < 1)$. The metasurface polarization beam splitter is placed in the focal plane of the half lens. Here, the half lens is used to avoid blocking the reflected beams.

The system aims to cover a square image area of size $L_x \times L_y$ with no spacing between adjacent beam spots, as shown in Figure 4.1. Since the positive phase gradient of the metasurface polarization beam splitter is along the negative x-direction, the wave vector in the y-direction follows the law of specular reflection. Therefore, in the y-direction, the nonlinearity of the abnormal reflection is not significant, and the system can be configured by only considering the normal reflection coverage. Each beam spot has the same width W_y in the normal reflection coverage area. To cover a length of L_y at a distance D from the metasurface while no spacing exists between adjacent beam spots, W_y should be equal to L_y/N. The required lens focal length f and the constant y-direction fiber spacing Δy can be determined by using paraxial geometric optics [130]:

$$f = \frac{L_y}{N \cdot 2\tan\alpha} - p \cdot D \tag{4.1}$$

$$\Delta y = 2f \cdot \tan\alpha \cdot (\frac{f}{D} + p) \tag{4.2}$$

where $\tan\alpha = \lambda/(\pi w_0)$ with the mode field radius w_0 (e^{-2} intensity radius) of the single-mode fiber. In the normal reflection coverage area, the beam spots are all circular. If the x-direction fiber spacing Δx is constant and equal to Δy, the normal reflection area can be just covered. However, in this case, owing to the nonlinearity of the abnormal reflection, the abnormal reflection coverage area cannot be fully covered. Thus, the position of each column of the fiber array x_1, x_2... should be determined by making the beam spots of adjacent fiber columns tangential along the x-direction in the abnormal reflection coverage area:

$$
\begin{aligned}
&D \cdot \tan\{\arcsin\{\sin[\arctan(\frac{x_{n+1} - pf \cdot \tan\alpha}{f})] + \frac{\lambda}{\Lambda}\}\} \\
&\qquad - f \cdot \tan\alpha \\
&= D \cdot \tan\{\arcsin\{\sin[\arctan(\frac{x_n + pf \cdot \tan\alpha}{f})] + \frac{\lambda}{\Lambda}\}\} \\
&\qquad + f \cdot \tan\alpha
\end{aligned}
\tag{4.3}
$$

where $n = 1,2...$, λ is the wavelength and Λ is the length of the super cell of the metasurface polarization beam splitter. x_n $(n \geq 2)$ can be obtained from the recursive equation (4.3) with the initial condition $x_1 = 0$.

A condition on x_M is still needed to determine where to stop (i.e., the value of M). This condition can be obtained from the situation in which the normal and abnormal reflection coverage areas exactly overlap:

$$
\begin{aligned}
&f \cdot \tan\{\arcsin\{\sin[\arctan(-p \cdot \tan\alpha)] + \frac{\lambda}{\Lambda}\}\} \\
&\qquad - \frac{2f^2 \cdot \tan\alpha}{D} - pf \cdot \tan\alpha \\
&\qquad \leq x_M < \\
&f \cdot \tan\{\arcsin\{\sin[\arctan(p \cdot \tan\alpha)] + \frac{\lambda}{\Lambda}\}\} \\
&\qquad - pf \cdot \tan\alpha
\end{aligned}
\tag{4.4}
$$

x_M should take the minimum value in this range. On the other hand, x_M is also limited by the critical angle of the metasurface polarization beam splitter:

$$
x_M < f \cdot \tan(\theta_{ic}) - pf \cdot \tan\alpha \tag{4.5}
$$

where $\theta_{ic} = \arcsin(1 - \lambda/\Lambda)$ is the critical angle of the metasurface polarization beam splitter. Based on the above two equations, the following condition should be satisfied to ensure that no gap exists between the normal and abnormal reflection coverage areas:

$$
\sin[\arctan(p \cdot \tan\alpha)] < 1 - \frac{2\lambda}{\Lambda} \tag{4.6}
$$

Since $p \cdot \tan\alpha$ is usually small ($\sim 10^{-2}$), a clearer relation can be obtained by ignoring it:

$$\Lambda > 2\lambda \tag{4.7}$$

which is the design requirement for the metasurface polarization beam splitter. With the value range of x_M and the initial condition $x_1 = 0$, the number of the fiber columns M and the x-position of each column $x_1, x_2 ... x_M$ can be fully determined by using the recursive equation (4.3). Furthermore, the coverage length in the x-direction can now be obtained:

$$\begin{aligned} L_x = D \cdot \tan\{\arcsin\{\sin[\arctan(\frac{x_M + pf \cdot \tan\alpha}{f})] + \frac{\lambda}{\Lambda}\}\} \\ + f \cdot \tan\alpha \end{aligned} \tag{4.8}$$

In the abnormal reflection coverage area, no spacing or overlap exists between adjacent beam spots. In the normal reflection coverage area, no spacing or overlap exists between adjacent beam spots along the y-direction, while an overlap exists between adjacent beam spots along the x-direction because the distance between two fiber columns is less than Δy. A square image area of size $L_x \times L_y$ is fully covered. In practice, due to the wavelength tuning, a slight wavelength difference exists between the beams emitted from different fibers. The maximum wavelength difference is usually tens of nanometers, which is two orders of magnitude smaller than the wavelengths in fiber-optic communication. Considering $\Lambda > 2\lambda$, the influence of wavelength change can be ignored, and the reflection characteristics of the metasurface can be considered the same for all the wavelengths. Therefore, the system can be configured at one wavelength (usually at the center wavelength), as done in the design process above.

As a comparison, we use the same basic parameters as Koonen et al. [130]: $p = 0.21$, $L_y = 1.68$ m, $D = 2.4488$ m, $N = 14$, $\lambda = 1.5$ μm, and $w_0 = 4.5$ μm. In our metasurface polarization beam splitter, $\Lambda = 4$ μm, which meets $\Lambda > 2\lambda = 3$ μm. Then, we find $f = 51.2$ mm, $\Delta y = 2.51$ mm, $M = 9$, $L_x = 2.75$ m, and $x_M = 19.4$ mm. Therefore, an image area of 2.75×1.68 m^2 is fully covered with a 9×14 2D fiber array (126-port AWGR), the total size of which is 19.4×32.63 mm^2. Compared with the demonstration by Koonen et al. [130], in which 1.68×1.68 m^2 is fully covered with a 14×14 2D fiber array (196-port AWGR) of total size 32.63×32.63 mm^2, our system is considerably enhanced in coverage and size while using the same basic parameters.

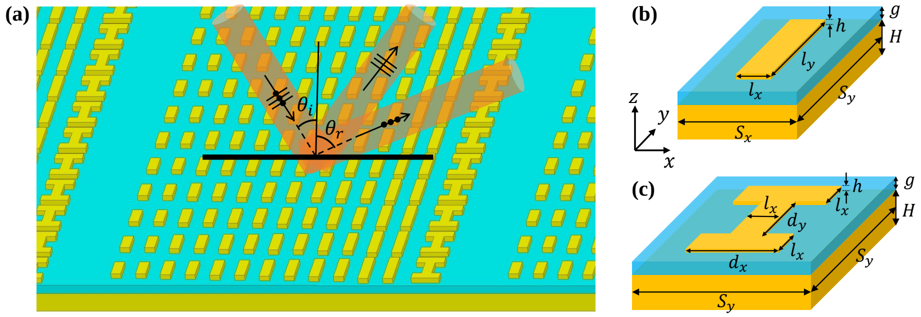

Figure 4.3: (a) Schematic of the designed polarization beam splitter. θ_i is the incident angle, and θ_r is the abnormal reflection angle (in the xz-plane). (b) Schematic of the type 1 meta-atom. (c) Schematic of the type 2 meta-atom.

4.4 Design of metasurface polarization beam splitter

The metasurface polarization beam splitter plays a key role in the proposed 2D IR beam-steering system. Here, to demonstrate the system concept, a GSPM-based metasurface polarization beam splitter is designed and fabricated at λ = 1550 nm. Figure 4.3(a) schematically shows the designed polarization beam splitter, which consists of periodical arrays of gap plasmon-based meta-atoms. Two types of meta-atoms are used, type 1 and type 2, as shown in Figure 4.3(b) and Figure 4.3(c), respectively. They are both composed of an Au ground, a SiO_2 spacer in the middle, and a top Au nano-pattern designed with different shapes. When the meta-atom is illuminated by an x-polarized or a y-polarized incident plane wave, electric currents are induced on both the top Au pattern and the bottom Au ground, which result in strong near-field coupling and anti-parallel electric current oscillations, forming strong magnetic resonance [150]. By varying the geometry of the meta-atoms, the reflection phase and amplitude of each unit cell can be engineered independently at the designed wavelength.

All the design parameters are optimized by using Lumerical finite-difference time-domain (FDTD) software. The software internal material database is used to build the structures. In the simulation of each meta-atom, periodic boundary conditions are applied on the structure's four sides (yz and xz-planes). Perfectly matched layer (PML) boundaries are applied on the top and bottom of the simulation box. A normally incident plane wave source at 1550 nm is used

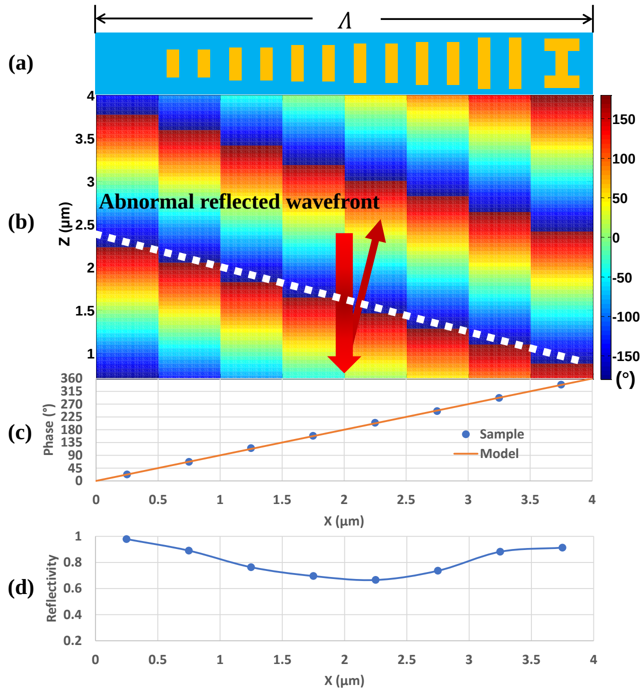

Figure 4.4: (a) Super cell of the designed metasurface polarization beam splitter. (b) Simulated scattered E_y phase patterns of all the phase units under the illumination of a normally incident y-polarized plane wave ($\lambda = 1550$ nm). (c) Scattered phase of each phase unit within a super cell. (d) Reflectivity of each phase unit within a super cell.

as illumination.

As shown in Figure 4.4(a), a super cell consists of 8 phase units is designed to cover a 2π phase with a $\pi/4$ phase interval. Each phase unit is made of meta-atoms with different geometries. In our design, all the meta-atoms share the following parameters: $S_x = 250$ nm, $S_y = 500$ nm, $H = 200$ nm, $g = 90$ nm, $l_x = 100$ nm, and $h = 55$ nm. The zero-phase unit has no Au pattern on the SiO_2 spacer. Each of the six phase units from $\pi/4$ to $6\pi/4$ is a parallel connection of 2 identical type-1 meta-atoms. The pattern lengths l_y are 225 nm, 266 nm, 292 nm, 315 nm, 345 nm, and 413 nm, respectively. The $7\pi/4$ phase unit is a single type-2 meta-atom with $d_x = 280$ nm and $d_y = 200$ nm. Compared with the design

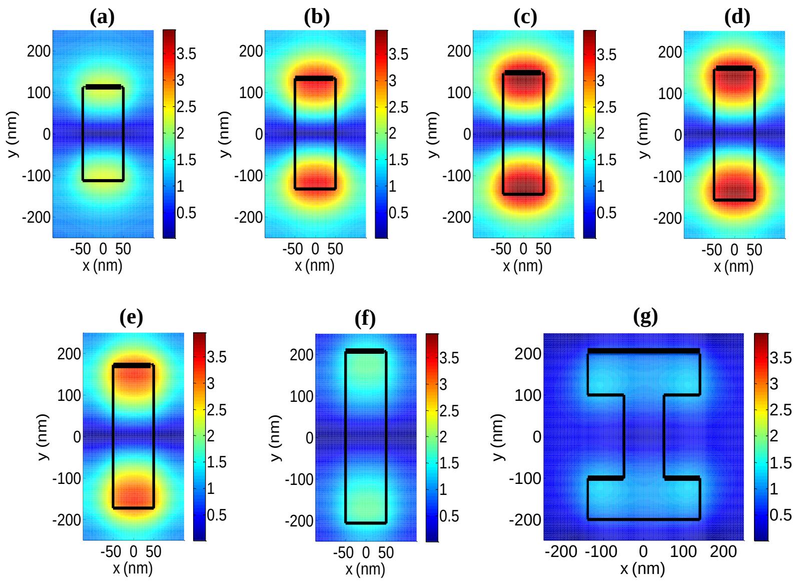

Figure 4.5: Magnitude of the electric field at $\lambda = 1550$ nm in the xy-plane in the center of the spacer, under a normally incident y-polarized plane wave. (a)-(f) correspond to l_y =225 nm, 266 nm, 292 nm, 315 nm, 345 nm, and 413 nm type-1 meta-atoms, respectively. (g) corresponds to the type-2 meta-atom.

wavelength $\lambda = 1550$ nm, all the meta-atoms have subwavelength dimensions.

Figure 4.4(b) shows the simulated scattered E_y phase patterns of all the phase units in a super cell under the illumination of a normally incident y-polarized plane wave ($\lambda = 1550$ nm). It can be seen that a positive phase gradient along the x-direction is formed, which creates an abnormal reflected wavefront. According to the generalized laws of reflection and refraction [151], for a y-polarized plane wave at an incident angle θ_i, the abnormal reflection angle θ_r is

$$\sin\theta_r = \sin\theta_i + \frac{\lambda}{\Lambda} \tag{4.9}$$

where Λ is the length of the super cell. In our design, $\Lambda = 4$ μm. It can be seen

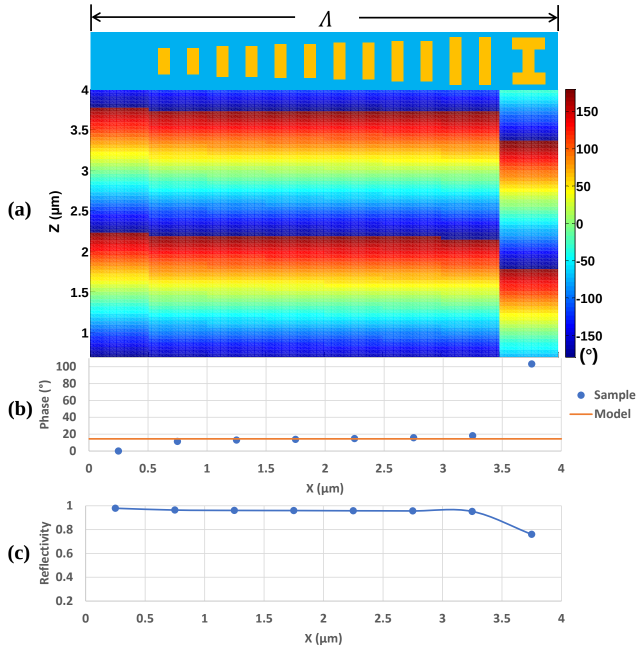

Figure 4.6: (a) Simulated scattered E_x phase patterns of all the phase units in a super cell under the illumination of a normally incident x-polarized plane wave ($\lambda = 1550$ nm). (b) Scattered phase of each phase unit within a super cell. (c) Reflectivity of each phase unit within a super cell.

that θ_i and θ_r have a nonlinear relation, and a critical angle exists for θ_i:

$$\theta_{ic} = \arcsin(1 - \frac{\lambda}{\Lambda}) \tag{4.10}$$

When $\theta_i > \theta_{ic}$, the abnormal reflection disappears, and surface plasmon-polaritons are excited. To obtain a broad incident range and meet the design requirement $\Lambda > 2\lambda$, a large θ_{ic} is needed, resulting in a large Λ. Therefore, eight phase units are used to cover 2π ($\theta_{ic} = 37.77°$) with a $\pi/4$ phase interval. However, the $\pi/4$ phase interval cannot be achieved using only type-1 meta-atoms; therefore, type-2 meta-atom is introduced to achieve a large phase shift.

Figure 4.4(c) precisely shows the scattered phase of each phase unit, which uniformly covers a 2π phase. The simulation results agree very well with the

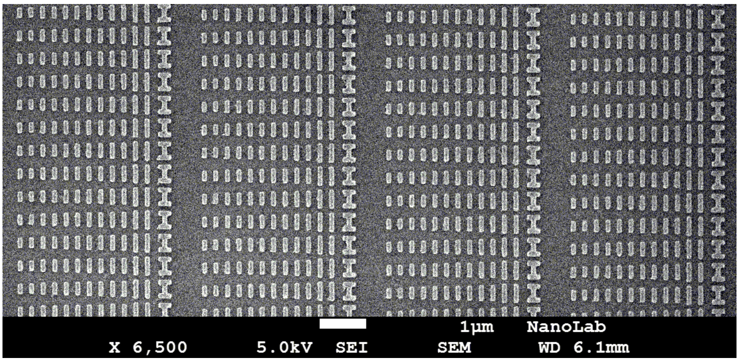

Figure 4.7: SEM image of the fabricated metasurface polarization beam splitter.

model. The reflectivity of each phase unis is shown in Figure 4.4(d), overall good efficiency is obtained. Figure 4.5 further shows the simulated xy-plane electric-field magnitude distribution in the center of the spacer of the designed meta-atoms. It can be seen that similar resonances occur in each meta-atom, and the resonance can be manipulated by varying the length of the top Au nanopattern. Therefore, different phase responses can be obtained. Combined with Figure 4.4(d), we can find that stronger coupling leads to lower reflectivity.

For an x-polarized incident plane wave, the phase response of each phase unit is designed to be basically the same. Figure 4.6(a) shows the simulated scattered E_x phase patterns of all the phase units in a super cell under the illumination of a normally incident x-polarized wave ($\lambda = 1550$ nm). The corresponding phase values are shown in Figure 4.6(b). Since two types of meta-atoms are used, a phase mismatch exists, as we can see in Figure 4.6(a). However, most of the phase units have the same phase response. Thus, in general, the super cell acts as a mirror. The reflectivity of each phase unis is shown in Figure 4.6(c), high efficiency is obtained.

Based on the above discussions, the designed metasurface has different reflection characteristics for x and y-polarized incident light, that is, a polarization beam splitter. With this polarization beam splitter, one can manipulate the direction and power of the reflected light by controlling the polarization of the incident light.

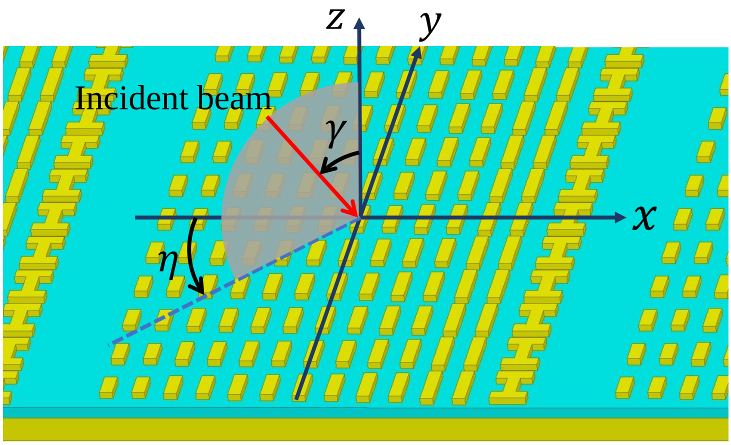

Figure 4.8: Schematic of the incident direction in the device measurements.

4.5 Device characterization and 2D beam steering

As shown in Figure 4.7, the designed metasurface polarization beam splitter was fabricated in our clean room with the following main steps: 1) A 200-nm Au ground was deposited on a Si substrate by metal evaporation. 2) a 90-nm-thick SiO_2 layer was deposited on the Au ground by plasma-enhanced chemical vapor deposition (PECVD). 3) A 950 PMMA A4 layer was spin-coated on the SiO_2 layer. After baking on a hotplate, the sample was sent into an electron beam direct write lithography system for pattern definition. After lithography, the sample was developed in an MIBK/IPA solution and then rinsed with IPA. 4) A 2-nm-thick Cr layer was deposited on the sample by metal evaporation to improve adhesion. Subsequently, a 53-nm-thick Au layer was deposited without taking the sample out. 5) The top Au patterns were obtained by acetone lift-off.

In the previous section, the metasurface is designed and optimized under the illumination of normally incident x and y-polarized plane waves at $\lambda = 1550$ nm. In addition, the discussed incident beams are limited in the xz-plane as shown in Figure 4.1, Figure 4.2(b), and Figure 4.3(a). These analyses are enough for system and device design. However, to support the ideal of polarization-wavelength-controlled 2D IR beam-steering, more solid proofs are needed. Therefore, the fabricated metasurface is fully measured under comprehensive incident, as schematically shown in Figure 4.8. The incident direction

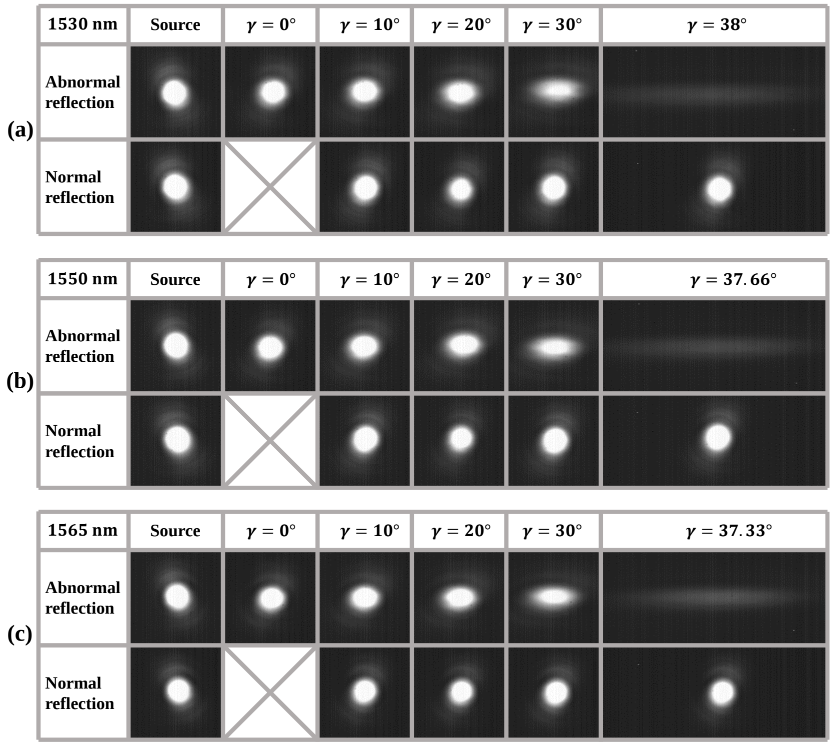

Figure 4.9: Measured far-field beam spots of the normal and abnormal reflection in the xz-plane ($\eta = 0°$) with different incident angles (γ). (a)-(c) correspond to λ =1530 nm, 1550 nm, and 1565 nm, respectively.

is described by two angles: the azimuthal angle η, and the polar angle γ, as defined in Figure 4.8. Because of the symmetry of the designed metasurface, η can be limited to 0° to 90°. We did comprehensive measurements in five incident planes: $\eta = 0°$, 20°, 45°, 65°, and 90°. In each incident plane, γ is set within 0° to 35°. Because wavelength tuning is applied in the system, all measurements are performed at three wavelengths: 1530 nm, 1550 nm, and 1565 nm, corresponding to C-band.

By using a charge-coupled device (CCD) image sensor, the far-field beam spots of the normal and abnormal reflection are observed in the xz-plane ($\eta = 0°$) with different incident angles (γ), as shown in Figure 4.9. Here, the

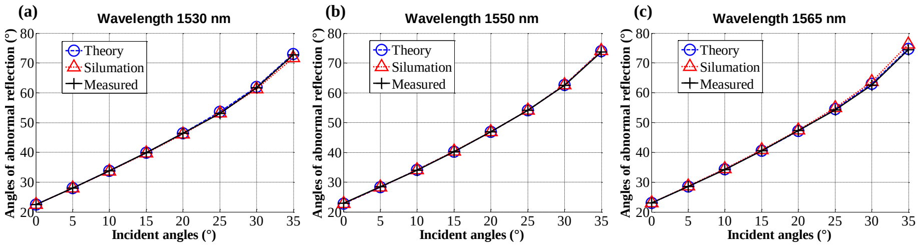

Figure 4.10: Measured relation between the incident angle and the abnormal reflection angle. The measurements are performed in the xz-plane ($\eta = 0°$). (a)-(c) correspond to λ =1530 nm, 1550 nm, and 1565 nm, respectively.

incident beams are collimated to have small divergence angles, and the incident beam spots are shown as references. All the beam spots are observed at the same distance from the light source. For the abnormal reflection, the beam spots slowly change from circular to oval-like as the incident angle (γ) increases. This is due to the nonlinearity of the abnormal reflection, which makes the beam diverge faster in the x-direction than in the y-direction. To observe the abnormal reflection closing to the critical angles, γ is set to 38°, 37.66°, and 37.33° at 1530 nm, 1550 nm, and 1565 nm, respectively. The critical angles at the three wavelengths are 38.13°, 37.77°, and 37.49°, respectively. It can be seen the observed beam spots are severely stretched, and the abnormal reflection almost disappears, which is as expected. We can also find that the beam distortion is slight when the incident angle (γ) is away from the critical angle, while severe distortion occurs when the incident angle (γ) is close to the critical angle, because the nonlinearity of the abnormal reflection is significant in this case. For the normal reflection, all the observed beam spots remain almost unchanged as the incident angle (γ) increases, proving that the designed metasurface acts as a mirror in this situation.

Figure 4.10 shows the measured relation between the incident angle and the abnormal reflection angle. These angle relations are measured in the xz-plane ($\eta = 0°$). It can be seen that the measurement results agree very well with the theory and the simulation results. The angle relation remains almost unchanged when the input wavelength switches from 1530 nm to 1565 nm, which is compatible with the proposed 2D IR beam-steering system.

To prove the feasibility of the proposed polarization-wavelength-controlled 2D IR beam steering, we measured the power imbalance between the normal and abnormal reflection at different incident polarization states and wave-

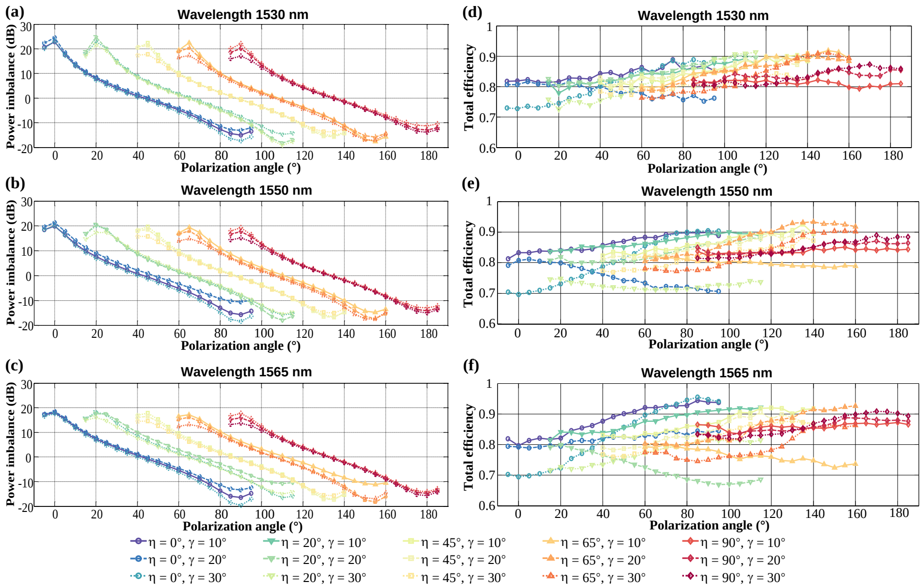

Figure 4.11: (a)-(c) Measured power imbalance changing with incident polarization states, at λ =1530 nm, 1550 nm, and 1565 nm, respectively. (d)-(f) Measured total efficiency changing with incident polarization states, at λ =1530 nm, 1550 nm, and 1565 nm, respectively. The measurements are performed in the five incident planes: $\eta = 0°$, 20°, 45°, 65°, and 90°. In each incident plane, three incident polar angles are set: $\gamma = 10°$, 20°, and 30°.

lengths, as shown in Figure 4.11(a), Figure 4.11(b), and Figure 4.11(c). The measurements are performed in the five incident planes (defined by η). In each incident plane, three incident polar angles are set: $\gamma = 10°$, 20°, and 30°. Here, the power imbalance is defined as the received optical power (in dBm) of the abnormal reflection minus that of the normal reflection. It can be seen at all the three wavelengths, when the polarization state changes by 90°, the beam power switches from the abnormal reflection direction to the normal reflection direction, and vice versa. The maximum and minimum power imbalance indicates the isolation between the normal and abnormal reflection. The polarization state that maximizes the abnormal reflection (or normal reflection) shifts as the incident plane changes. We also measured the total efficiency of the normal and abnormal reflection, as shown in Figure 4.11(d), Figure 4.11(e), and Fig-

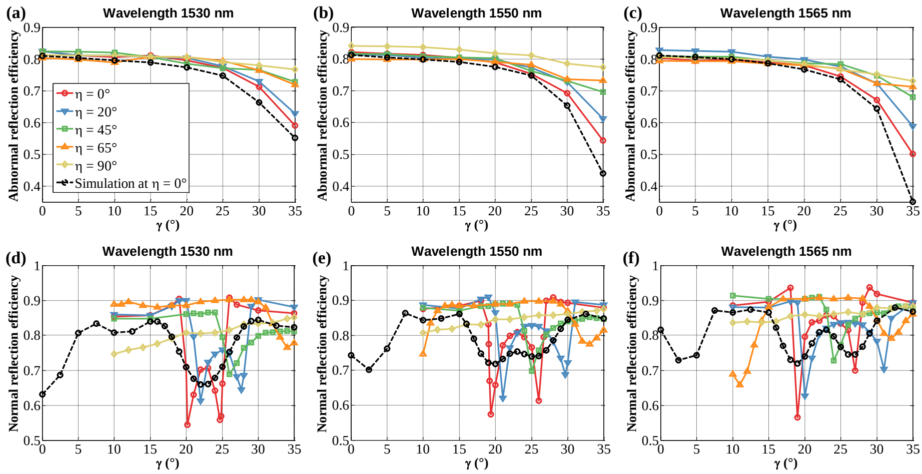

Figure 4.12: Measured power efficiency of the abnormal reflection ((a)-(c)) and normal reflection ((d)-(f)), at λ =1530 nm, 1550 nm, and 1565 nm, respectively. The measurements are performed in the five incident planes: $\eta = 0°$, 20°, 45°, 65°, and 90°. Simulation results at $\eta = 0°$ are also presented.

ure 4.11(f). High power efficiency (> 67%) is achieved at all the polarization states and wavelengths. Polarization-controlled 2D beam steering is verified in a broad wavelength band, which gives good proof to the proposed 2D beam steering system.

The power efficiency of the normal and abnormal reflection is also measured in the five incident planes with different incident polar angles (γ), as shown in Figure 4.12. The measurements start from $\gamma = 10°$ because the normal reflection is blocked by our measurement setup when $\gamma < 10°$. The power efficiency of the abnormal reflection (normal reflection) is measured by adjusting the incident polarization to maximize the received abnormal reflection (normal reflection) power while keeping the incident power constant. At all the three wavelengths, the measured results show similar trends. For the abnormal reflection, the reflection efficiency decreases gently with increasing γ. The measured efficiency is approximately 80% when γ is less than 15° in all the incident planes and wavelengths, and it is > 70% when γ is less than 25°, which is state-of-the-art efficiency. For the normal reflection, in all the incident planes and wavelengths, the measured reflection efficiency is > 75% for most of the γ. It can be seen when $\eta = 0°$, 20°, 45°, and 65°, there are efficiency notches at some specific γ,

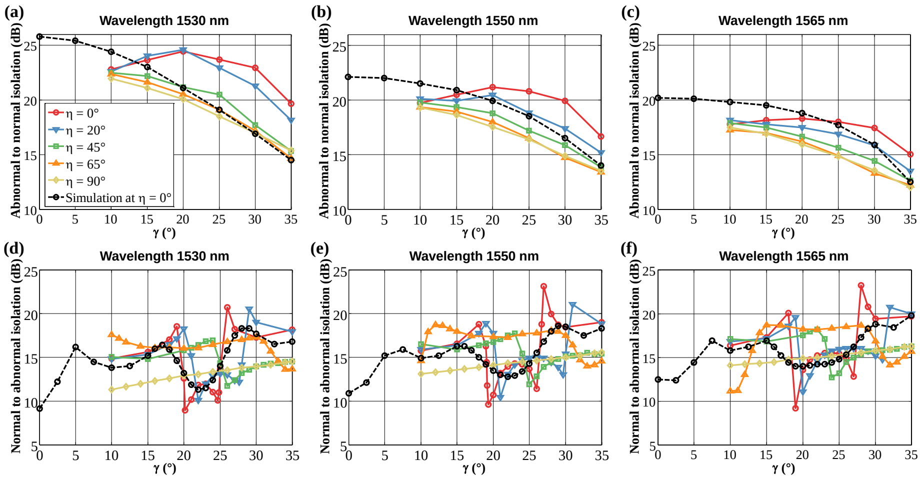

Figure 4.13: (a)-(c) Measured abnormal to normal isolation, at λ =1530 nm, 1550 nm, and 1565 nm, respectively. (d)-(f) Measured normal to abnormal isolation, at λ =1530 nm, 1550 nm, and 1565 nm, respectively. The measurements are performed in the five incident planes: $\eta = 0°$, 20°, 45°, 65°, and 90°. Simulation results at $\eta = 0°$ are also presented.

where the efficiency drops to around 60%. This is caused by the angular dispersion under transverse magnetic (TM)-polarized illumination [152]. When $\eta = 90°$, there is no efficiency notch. Because in this case, the incident wave that maximizes the normal reflection is a transverse electric (TE) wave. In general, the influence of the angular dispersion is limited, and a high reflection efficiency is achieved. The simulation results at $\eta = 0°$ are also presented in Figure 4.12. The trend of the simulated curves matches that of the measured curves. For the efficiency of the abnormal reflection, good agreement is achieved between the simulation and the measurement, especially when $\gamma < 30°$. For the efficiency of the normal reflection, the position of the efficiency notches is also matched. The difference between the simulation and the measurement mainly comes from the fabrication error, the material property difference between the simulation database and the actually used materials, and the simulation accuracy. Nevertheless, the simulation results do show the important characteristics of the fabricated metasurface.

The isolation between the normal and abnormal reflection is measured in the same manner as the efficiency. As shown in Figure 4.13, the isolation shows similar trends as the efficiency. The overall abnormal to normal isolation decrease from 20 ± 5 dB to 15 ± 3 dB as the wavelength increases from 1530 nm to 1565 nm. The overall normal to abnormal isolation is 15 ± 5 dB at all the three wavelengths. Isolation notches can be seen in Figure 4.13(d), Figure 4.13(e), and Figure 4.13(f), which is caused by the efficiency notches of the abnormal reflection. The isolation can also be obtained from the maximum and minimum values of a power imbalance curve shown in Figure 4.11, but only for $\gamma = 10°$, 20°, and 30°. The simulation results at $\eta = 0°$ are also presented in Figure 4.13.

The measurement results prove the abnormal reflection characteristics and the good performance of the designed metasurface polarization beam splitter in a broad bandwidth from 1530 nm to 1565 nm (C-band). The device has a large incident angle range and a high reflection efficiency. When the incident polar angle (γ) changes from 0° to 35°, the efficiency (for both normal and abnormal reflection) is larger than 50% (3 dB). An incident polar angle of up to 35° is available, which is close to the critical angle (37.77° at 1550 nm when $\eta = 0°$). Polarization-controlled 2D IR beam-steering is also verified by changing the polarization states of incident beams in multiple incident planes and polar angles. Therefore, the feasibility of the proposed 2D IR beam-steering system is verified.

4.6 A system example

Here, an example of the proposed 2D beam-steering system is designed to show its feasibility further. Since the fabricated metasurface polarization beam splitter is measured in C-band, we use a commercially available C-band 96-port AWGR (90 ports are used) in this design. By using the same basic parameters as the AWGR-based beam-steering module in Koonen et al. [131]: $p = 0.21$, $w_0 = 4.5$ μm, $f = 51.2$ mm, and 12-cm spot size, full coverage area of 1.2×2.9 m^2 with room height 2.4488 m is obtained, which is equivalent with a beam-steering angle range of ±13.8°×49.8°. The designed system example has an achievable f/0.95 lens and a 9×10 2D fiber array arranged as follows: x positions=(0, 2.459, 4.906, 7.343, 9.768, 12.181, 14.583, 16.973, 19.352) mm and $\Delta y = 2.51$ mm. It is worth noting that the fabricated metasurface does not reach its bandwidth limit in C-band, which means the beam steering range can be increased by extending the wavelength tuning range and using AWGRs operating at corresponding wavelengths. Figure 4.14 shows the calculated coverage area filled by the beam spots; herein the e^{-2} intensity contours of the beam spot footprints are shown. It can be seen that the beam spots are circular in the normal

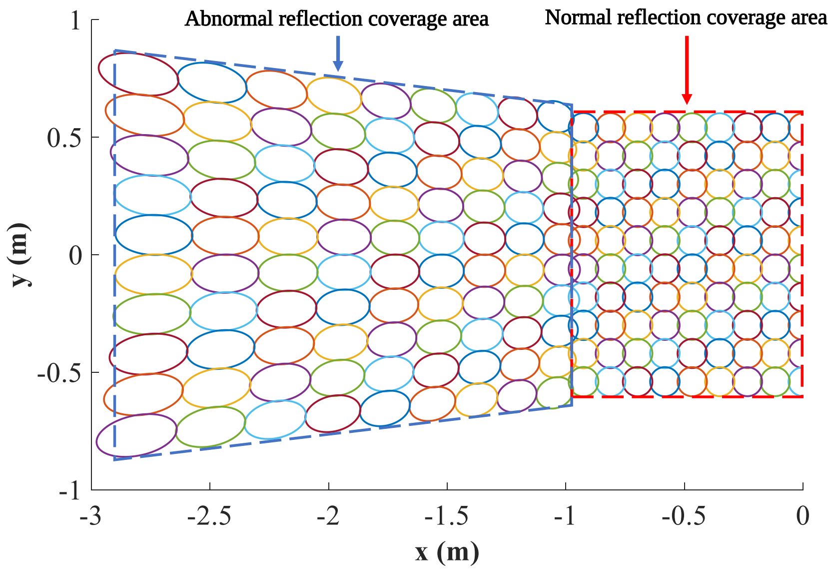

Figure 4.14: The designed system example fully fills the coverage area with its beam spots.

reflection coverage area, while they expand and become oval-like in the abnormal reflection coverage area, which is as expected and experimentally observed in Figure 4.9. In addition, the abnormal reflection coverage area expands along y-direction due to the nonlinearity of the abnormal reflection, which is ignored in the design process presented in Section 4.3. Nevertheless, full area coverage can still be maintained, and the design process applies.

For the designed system example, by using the same basic parameters of the AWGR-based beam-steering module, a larger coverage area is obtained with fewer AWGR ports and a smaller wavelength tuning range (only C-band). Since the extra loss introduced by the metasurface is less than 50% according to the measurement results, and the AWGR-based beam-steering module with the same basic parameters has been demonstrated in [131], the feasibility of the designed system can be verified.

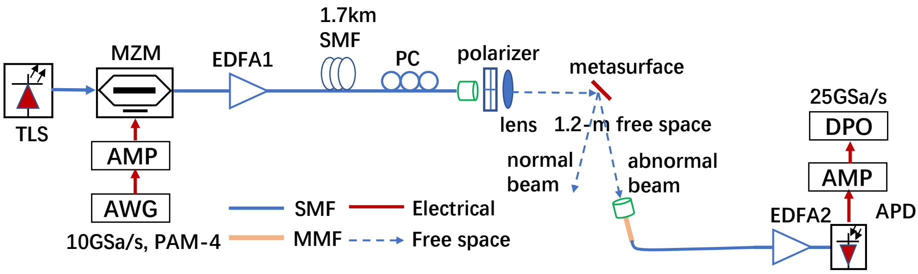

Figure 4.15: Experimental setup of the metasurface-based beam-steered IR wireless link. AMP: amplifier, APD: avalanche photodiode, AWG: arbitrary waveform generator, DPO: digital phosphor oscilloscope, EDFA: erbium-doped fiber amplifier, MMF: multi-mode fiber, MZM: Mach-Zehnder modulator, PC: polarization controller, SMF: single-mode fiber, TLS: tunable laser source.

4.7 Proof-of-concept experiment

A proof-of-concept experimental setup was built using the fabricated metasurface, as shown in Figure 4.15. A tunable laser source with a 10-dBm output optical power is used to generate the optical carrier in the communication control center, which is then modulated by a 10-GHz Mach-Zehnder modulator (MZM). The electrical data are produced by an arbitrary waveform generator (AWG) to drive the MZM after amplification. In the experiment, transmitted pulse amplitude modulation (PAM) signals are generated offline using a MATLAB program and then sampled by the AWG running at 10 GSa/s, producing a 10-GBaud/s PAM-4 baseband signal. Thus, the achieved data rate is 20 Gbps. It is worth noting that the data rate is limited by the used optoelectronic devices. If a large bandwidth transceiver is employed, a 100-Gbps data rate or more can be achieved. Moreover, the insertion loss caused by the designed metasurface chip is less than 3 dB, which enables the achievement of high signal-to-noise-ratio values to meet the high-speed transmission requirement. The modulated optical signal is amplified by an erbium-doped fiber amplifier (EDFA) and then launched into a 1.7-km single-mode fiber. A polarization controller (PC) combined with a free-space polarizer is used to control the polarization states of the incident light so as to manipulate the power distribution of beams emerging from the metasurface chip. The optical beam is launched into free space via a collimator (the focal length is 18 mm) with a measured power below 10 dBm which meets the requirements of human eye safety. The light is further

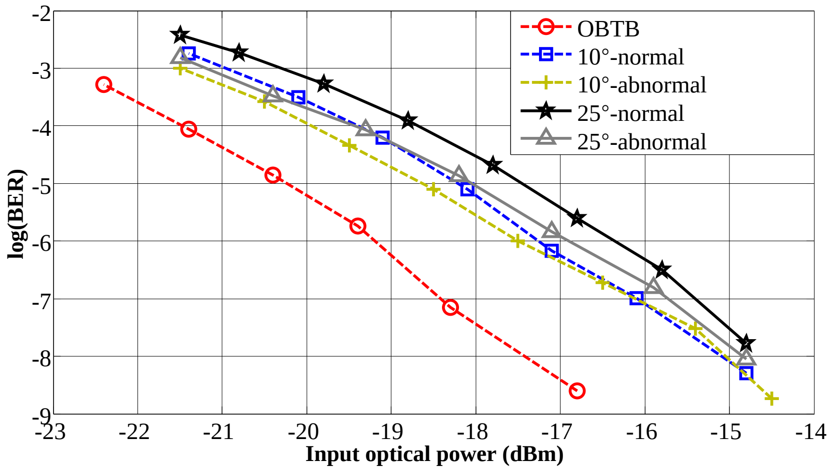

Figure 4.16: BER performance of a 10-GBaud/s PAM4 signal over 1.2-m free space at incident angles $\gamma = 10°$ and 25°. The measurements are performed in the xz-plane ($\eta = 0°$), and $\lambda = 1550$ nm.

collimated by a lens and then launched onto the chip, resulting in normal and abnormal beams. After 1.2-m free-space transmission, both beams are coupled into a short section of multi-mode fiber (MMF) and then a single-mode fiber (SMF) via another collimator. The received optical power is amplified and then detected by an avalanche photodiode. The amplified output electrical PAM-4 signal is oversampled by a digital phosphor oscilloscope (DPO) sampling at 25 GSa/s for further signal processing.

Figure 4.16 illustrates the bit-error-ratio (BER) performance of the 20-Gbps PAM-4 signal as a function of the optical power received by a variable optical attenuator placed at the front of the avalanche photodiode. Here, the incident beam is in the xz-plane ($\eta = 0°$), and the incident angles (γ) are set to 10° and 25°. Four output beams are generated, transmitted, and measured at the receiver end, as shown in Figure 4.16. We also measured the BER performance of the 20-Gbps PAM-4 signal at optical back-to-back (OBTB) transmission. Compared to the OBTB transmission, a penalty of almost 3dB is observed at a 7% forward error correction limit of 1×10^{-3}, which is mainly caused by the noise figure of the EDFA at the receiver end.

4.8 Conclusion

By combining active and passive approaches, we proposed a novel 2D IR beam-steering system, which can be tuned by changing the wavelength and polarization. The polarization tuning is achieved by using a metasurface polarization beam splitter in conjunction with a liquid-crystal polarization controller. The wavelength tuning is enabled by an AWGR-based beam-steering module. Thus, the proposed system keeps all the advantages of AWGR-based beam-steering approaches and additionally has polarization control capability. Furthermore, the grating loss existing in SLM-based and grating-based beam-steering approaches is avoided by using the metasurface. Therefore, the proposed system has the scalability to support multiple beams, flexibility to steer the beam, high optical efficiency, and a large coverage area. With the designed and fabricated metasurface polarization beam splitter, polarization-controlled 2D IR beam steering experiments are performed, and a 20-Gbps beam-steered IR wireless link is built as a proof-of-concept.

Chapter 5

Optical OAM Modes Multiplexing/Demultiplexing Enabled by Metasurface-based Dammann Vortex Grating

We have discussed photonic techniques for RF-OAM modes generation/detection in Chapter 3. Taking it one step further, enabling optical OAM modes multiplexing/demultiplexing is also of great value because it can massively increase the capacity of narrow-beam OWC systems. In this Chapter, by combining the Dammann vortex grating approach and the metasurface techniques presented in Chapter 4, a metasurface-based Dammann vortex grating is designed, fabricated, and experimentally demonstrated as a low-cost, high-efficiency method for optical OAM modes multiplexing/demultiplexing.

5.1 State-of-the-art and the proposed approach

5.1.1 State-of-the-art

In a narrow-beam OWC system, the communication link between the two parties is established by a narrow light beam. "Traditional" multiplexing techniques such as wavelength-division multiplexing and polarization-division multiplexing enable the link with many channels, therefore increasing the aggregate transmission data rate significantly. To further promote the communication capacity to the next level, OAM is widely favored because it offers a new degree of freedom for multiplexing [48, 49].

In order to enable OAM as the capacity multiplier in practical narrow-beam OWC systems, it is essential to find efficient approaches and devices for optical OAM modes multiplexing/demultiplexing. Conventional optical vortex generation approaches are based on spiral phase plates [151, 153–159], phase holograms [160–162], and Q-plates [163]. These devices can be implemented by bulk materials or advanced metasurfaces. However, for these non-reconfigurable devices, the flexibility of arbitrary optical OAM mode generation is limited.

A liquid-crystal-based SLM can be used to dynamically form desired phase mask and generate/detect the desired OAM modes [102, 164, 165]. However, for multiplexing different OAM modes, each OAM mode with independent modulation needs to be generated separately in space (by different SLMs or by different areas of an SLM), and then combined by multiple optical beam combiners to produce coaxially propagated OAM multiplexing beams. At the receiver end, for OAM modes demultiplexing, only a certain OAM mode can be converted to a Gaussian mode by an SLM (or an area of an SLM) which is loaded with a spiral phase pattern inverse to the OAM mode to be demultiplexed, while all other modes remain in an OAM state with a nonzero charge [164, 165]. This spatial separation method makes parallel detection of massive OAM channels difficult. With such SML-based approaches, multiplexing OAM modes with independent data channels and demultiplexing massive OAM channels in parallel need a large number of expensive SLMs and beam splitters/combiners, resulting in sophisticated systems, bulk volume, high optical loss, and high cost, which prevents their practical implementations. In [102] and [165], although free-space data links with an ultra-high data capacity of 2.56 Tbps and 100 Tbps is obtained by multiplexing 4 and 12 OAM modes, respectively, only four independent OAM channels are established with four SLMs. Therefore, these pioneering works mainly demonstrate the great potential of OAM multiplexing-based OWC systems. In practice, new approaches are urgently needed to multiplex independent OAM channels and realize parallel demultiplexing, as well as merge OAM multiplexing with other existing multiplexing techniques.

Impressively, binary-phase Dammann vortex gratings [166–169] are demonstrated to have the capabilities of multiplexing massive OAM channels with independent modulation and simultaneous demultiplexing [51]. Binary-phase vortex gratings through hologram coding can be used to achieve the same function [170], while Dammann vortex gratings concentrate diffraction energy into the desired diffraction orders and make the massive OAM channels with uniform energy distributions, therefore greatly increasing the energy efficiency and extending the OAM modes generation/detection range [166]. In [51], independent collinear free-space OAM channels generation, transmission, and simultaneous detection using Dammann vortex gratings are demonstrated. By multiplexing 10 independent OAM channels together with 80 wavelengths and 2 polarizations, 80/160 Tbps system capacity is achieved. Therefore, Dammann vortex grating-based OAM modes multiplexing/demultiplexing techniques show a practical path toward an OWC capacity of Pbps level. In [52] a reflective metasurface-enabled special binary-phase vortex grating is proposed to multiplex OAM modes and polarization states simultaneously in an OWC system. By multiplexing 4 independent OAM channels and 2 polarizations, a system capacity of 448 Gbps is achieved. The same function can also be realized by a Dammann vortex grating to further improve energy efficiency.

5.1.2 The proposed approach

Based on the discussions above, it is very attractive to implement Dammann vortex gratings in a low-cost and high-efficiency way. The phase pattern of a Dammann vortex grating can be obtained with an SLM. However, due to its large spatial resolution (~20 μm), the number of OAM modes that can be supported and the energy efficiency are limited. In this Chapter, by taking advantage of the metasurface techniques presented in Chapter 4, a metasurface-enabled 1×2 Dammann vortex grating, which has an intrinsic topological charge of $+3$, is designed, fabricated, and experimentally demonstrated as a powerful tool for optical $l = \pm3$ OAM modes multiplexing/demultiplexing. The 0-π binary-phase Dammann vortex grating is realized by filling the desired grating phase patterns with the designed sub-wavelength metasurface 0 and π phase units. Such pixel-filling method can also be used to easily realize Dammann vortex gratings for multiplexing/demultiplexing other OAM modes, bringing advantages of flexibility, stability, and low cost (one set of phase units and fabrication process for different Dammann vortex gratings). The proposed device keeps Dammann vortex grating's capability of simultaneously multiplexing/demultiplexing massive OAM beams with independent modulation, as well as the metasurface's unprecedented features of high efficiency, easy-to-fabrication, compact in size, and very-low grating loss.

5.2 Dammann vortex grating-based OAM modes multiplexing/demultiplexing

We first define an operator *mod* on real numbers: $a \, mod \, b = a - b \times \lfloor a/b \rfloor$, where a and b are real numbers, and $b \neq 0$. $\lfloor a/b \rfloor$ is the floor function that takes as input a real number a/b, and gives as output the greatest integer less than or equal to a/b. It can be inferred that $0 \leq a \, mod \, b < b$. Based on the *mod* operation, we define a function $B(c)$ on $c \in [0, b)$. $B(c)$ is determined by a set of transition points c_k, where $0 \leq k \leq u$ is an integer, $u \geq 2$ is the total number of the transition points, and $0 = c_0 < c_1 < c_2 < ... < c_k < ... < c_u = b$. $B(c)$ is then expressed as:

$$B(c) = \begin{cases} 1, \; c_{2t} \leq c < c_{2t+1} \\ -1, \; c_{2s+1} \leq c < c_{2s+2} \end{cases} \tag{5.1}$$

where t and s are integers that satisfy $0 \leq t \leq (u-1)/2$ and $0 \leq s \leq (u-2)/2$, respectively. It can be seen that the value of $B(c)$ is 1 in $[0, c_1)$, and it shifts from 1 to -1 or -1 to 1 at each of the transition points c_k, $1 \leq k \leq u-1$. Therefore, the only free parameters of $B(c)$ are the transition points c_k and the upper bound b of the function domain.

Now we can obtain the function needed:

$$G(\phi) = B(\phi \, mod \, 2\pi) \tag{5.2}$$

where ϕ is a real number, It is easy to conclude that $G(\phi)$ has a period of 2π. Therefore it can be expressed by its Fourier series:

$$G(\phi) = \sum_{n=-\infty}^{+\infty} A_n \exp(in\phi) \tag{5.3}$$

$$A_n = \frac{1}{2\pi} \int_{-\pi}^{\pi} G(\phi) \exp(-in\phi) \mathrm{d}\phi \tag{5.4}$$

Equation (5.4) gives the amplitude A_n of the n^{th} harmonic, and $|A_n|^2$ denotes the energy. Since $b = 2\pi$ is fixed for $G(\phi)$, the only free parameters of $G(\phi)$ is the transition points; therefore A_n is only depends on the transition points. From Dammann grating [168], a series of special transition points can be obtained: $c'_k = 2\pi X_k$ (for $k \geq 1$), where X_k is the phase transition positions of Dammann gratings presented in [171]. Such transition points uniformly distribute energies among the designed harmonics. Actually, when we set $\phi = \gamma x$ (a blazed phase), where x is the horizontal spatial coordinate, $\gamma = 2\pi/d$, and d is the grating period, as well as use a set of c'_k, corresponding one-dimensional Dammann grating is obtained from $G(\phi)$.

Now we set $\phi = \gamma x + i\ell\varphi$ (a blazed spiral phase), and use c'_k as transition points, a one-dimensional Dammann vortex grating can be obtained:

$$V_{\gamma,\ell}(x, y) = G(\gamma x + i\ell\varphi) = \sum_{n=-\infty}^{+\infty} A_n \exp(in\gamma x)\exp(in\ell\varphi) \tag{5.5}$$

where ℓ is the intrinsic topological charge of the grating, φ is the azimuthal angle. The Dammann vortex grating keeps the Dammann grating's capability of uniformly distributing energies among the designed diffraction orders because the same transition points (c'_k) are used (therefore the same A_n). Besides, it encodes $l = n\ell$ OAM mode onto the n^{th} diffraction order, as shown in equation (5.5), which is the basis of Dammann vortex grating-based OAM modes multiplexing. If we illuminate the grating with a vortex beam carrying $l = m$ OAM mode. The product can be represented by $\sum_{n=-\infty}^{+\infty} A_n \exp(in\gamma x)\exp[i(n\ell + m)\varphi]$, which indicates the $l = m$ OAM mode can be demultiplexed when $n\ell + m = 0$.

Through the above discussion, the operation principle of Dammann vortex grating-based OAM modes multiplexing/demultiplexing is explained, and the method to generate a Dammann vortex grating is also presented. Two-dimensional gratings can be easily obtained by superimposing the phase of an x- and a y-dimensional Dammann vortex gratings [166]. For clarity, a simple $l = \pm 3$ OAM modes multiplexing/demultiplexing system based on two identical reflective 1×2 Dammann vortex gratings with an intrinsic topological charge of $+3$ is shown in Figure 5.1. At the receiver end, due to the doughnut intensity profile of an OAM beam, the Gaussian beam converted from the demultiplexed OAM beam can be easily separated from other OAM beams by using a pinhole [51] or by directly coupling into a single-mode fiber [165]. It can be seen that the system supports simultaneously multiplexing/demultiplexing of multiple OAM beams with independent data channels, and can easily merge OAM modes multiplexing with other existing multiplexing techniques (data 1 and data 2 can be wavelength-multiplexed and polarization-multiplexed). In Figure 5.1, the shown grating order n corresponds to the incidence collinear

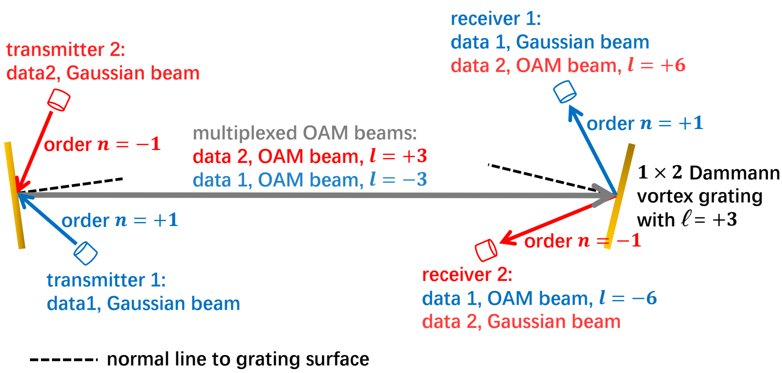

Figure 5.1: A simple $l = \pm 3$ OAM modes multiplexing/demultiplexing system based on two identical reflective 1×2 Dammann vortex gratings with an intrinsic topological charge of $+3$.

with the transmission direction of the multiplexed OAM beams. In practice, the transmission direction is usually aligned to be perpendicular to the grating surface to obtain maximum input/output angle range. Here, the case of non-perpendicular is shown to illustrate the moderate alignment requirements of the system.

5.3 Design of metasurface-based Dammann vortex grating

We aim to design a metasurface-based 1×2 Dammann vortex grating, which has an intrinsic topological charge of $+3$, at $\lambda = 1550$ nm. The basic design method is to use sub-wavelength phase units (or phase pixels) to fill the phase pattern of the corresponding Dammann vortex grating. Because a Dammann grating is a 0-π binary-phase grating, we only need two kinds of phase units: 0 and π, which significantly reduces the design difficulty, the structural complexity, and the impact of simulation and fabrication errors on device performance (more phase units bring more errors). Here, phase units consisting of meta-atoms used in Chapter 4 are designed, as shown in Figure 5.2. Each of them is a parallel connection of two identical meta-atoms shown in Figure 5.3(a). The used meta-atoms share the following parameters: $S_x = 250$ nm, $S_y = 500$ nm, $H = 200$ nm, $g = 90$ nm, $l_x = 100$ nm, and $h = 55$ nm. The top pattern lengths l_y of the 0

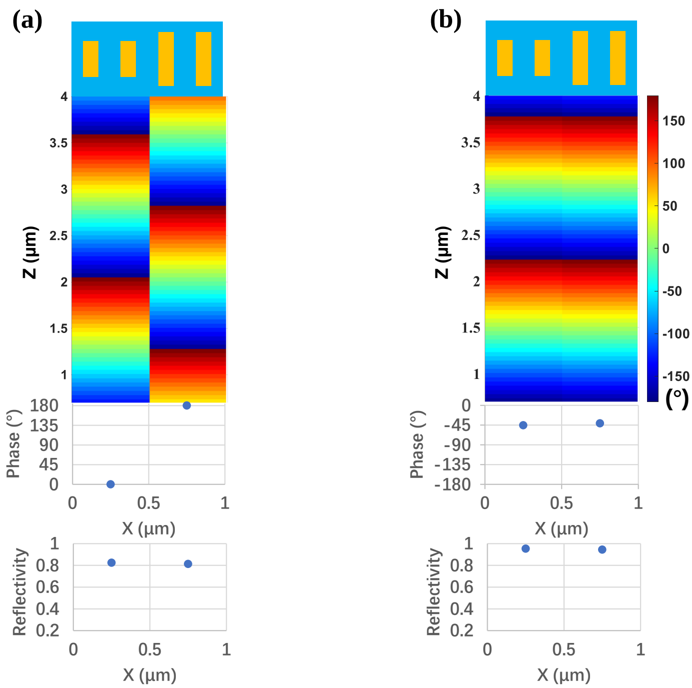

Figure 5.2: (a) Simulated scattered E_y phase patterns and reflectivity of the phase units under the illumination of a normally incident y-polarized plane wave (λ = 1550 nm). (b) Simulated scattered E_x phase patterns and reflectivity of the phase units under the illumination of a normally incident x-polarized plane wave (λ = 1550 nm).

and π meta-atoms are 240 nm and 360 nm, respectively. As shown in Figure 5.2(a), there is a phase difference of π between the scattered E_y phase patterns of the two phase units under the illumination of a normally incident y-polarized plane wave (λ = 1550 nm). Besides, the two phase units have almost the same high reflectivity (>80%). Therefore, the desired phase units are obtained for y-polarized incidence. For an x-polarized normally incident plane wave, the two phase units have almost the same phase response and high reflectivity (>95%), as shown in Figure 5.2(b). In this case, the device act as a nice mirror.

The designed square phase units have a side length of 500 nm. This length is used as the minimum spatial resolution to generate the phase pattern of the

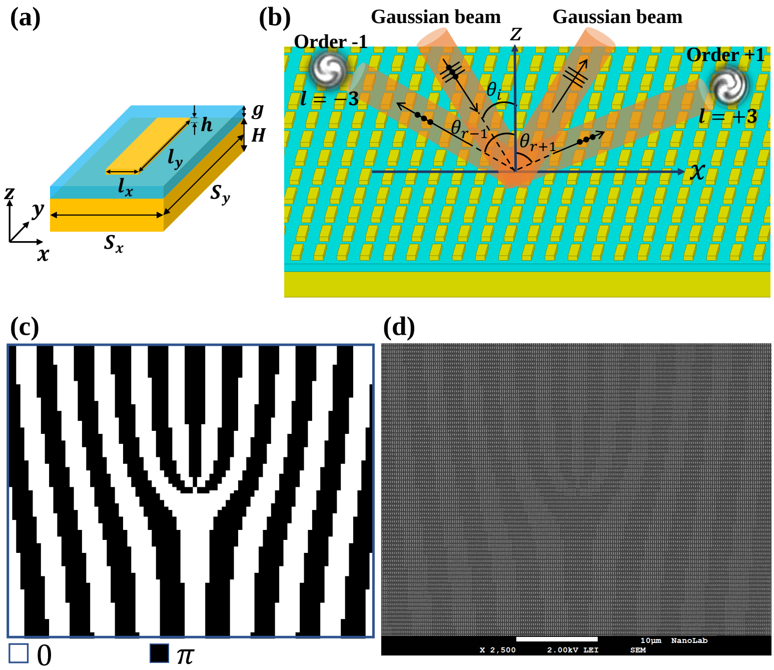

Figure 5.3: (a) Schematic of the used meta-atom. (b) Schematic of the designed Dammann vortex grating. The incident and reflections are in the xz-plane. θ_i is the incident angle, θ_{r+1} is the reflection angle of the $+1$ grating order, θ_{r-1} is the reflection angle of the -1 grating order. (c) Phase pattern of the designed Dammann vortex grating (center part). (d) SEM image of the fabricated Dammann vortex grating (center part).

1×2 Dammann vortex grating with MATLAB, as shown in Figure 5.3(c). The grating period is set to 5 μm, containing 10 pixels. After filling the phase pattern with the phase units, the desired grating is obtained. When illuminated by a y-polarized Gaussian beam (or plane wave), its ±1 diffraction orders carry ±3 OAM modes respectively, as shown in Figure 5.3(b).

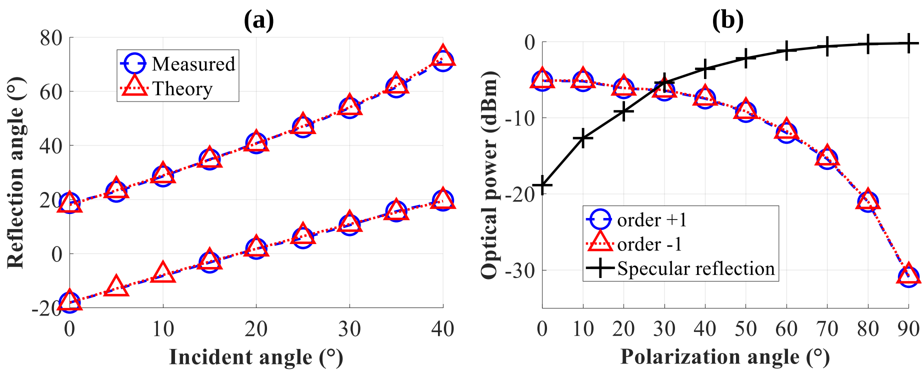

Figure 5.4: (a) Measured relation between the incident angle and the reflection angles of the ±1 grating orders (λ=1550 nm). (b) Measured optical power of the ±1 grating orders and the specular reflection changing with incident polarization states. θ_i=25°, λ=1550 nm.

5.4 Device characterization and optical OAM modes generation

The designed metasurface-based 1×2 Dammann vortex grating is fabricated in our cleanroom following the same process of the metasurface polarization beam splitter presented in Chapter 4. Figure 5.3(d) shows the SEM image of the device. Since the designed grating is a one-dimensional grating, all the measurements are performed in the xz-plane with a collimated Gaussian incident beam, as shown in Figure 5.3(b). Here, due to the symmetry of the grating, we only apply incidence on the left side of the z-axis, and the incident angles are recorded as positive values. For the reflections, angles on the left side of the x-axis are recorded as negative values, while angles on the right side of the x-axis are recorded as positive values.

5.4.1 Grating characteristics

Figure 5.4(a) shows the measured relation between the incident angle and the reflection angles of the ±1 grating orders. It can be seen that the measurement results agree very well with the results calculated by the grating equation, which proves the manufacturing accuracy of the grating period. Two reflection angles of grating order -1 at 5° and 10° incident angles are missing because the reflections are blocked by our measurement setup.

To demonstrate the polarization dependence of the reflections, the output optical power of the ±1 grating orders and the specular reflection is measured as a function of incident polarization states at an incident angle of 25°, as shown in Figure 5.4(b). The incident optical power is set to 0 dBm, and the incident wavelength is 1550 nm. 25° is chosen for the measurement convenience of all the reflections. It can be seen that when the polarization state changes by 90°, the reflection power switches from the ±1 grating orders to the specular reflection, and vice versa. Under y-polarized incidence (polarization angle = 0°), the desired grating is obtained, and the ±1 grating orders have almost the same optical power as anticipated. The total power efficiency of the ±1 grating orders is 0.61. Considering the simulated reflectivity of the used meta-atoms is 0.8, and the maximum efficiency of a 1×2 Dammann grating is 0.8106 [171], providing a maximum reflection efficiency of 0.64, the majority of the reflected power is indeed concentrated in the desired ±1 grating orders. For TM incidence (polarization angle = 90°), the device behaves as a mirror with high reflectivity (about 0.95), which is as expected.

Table 5.1: Measured power efficiency of the ±1 grating orders and the specular reflection.

Incident Angle (°)	**Wavelength (nm)**	**Polarization Angle (°)**	**Power Efficiency**		
			order -1	**Specular**	**order +1**
25	1530	0	0.3126	0.0160	0.2606
		90	0.0008	0.9440	0.0007
	1550	0	0.3033	0.0143	0.3047
		90	0.0008	0.9616	0.0007
	1570	0	0.2786	0.0152	0.3061
		90	0.0007	0.9418	0.0006
40	1530	0	0.2978	0.1513	0.1442
		90	0.0008	0.9418	0.0007
	1550	0	0.2992	0.1485	0.1218
		90	0.0007	0.9506	0.0007
	1570	0	0.3054	0.1258	0.0758
		90	0.0007	0.9682	0.0005

To investigate the broadband performance and the behaviors at large incident angles, power efficiency of the ±1 grating orders and the specular reflection under incident angles of 25° and 40° is measured and compared at three wavelengths (covering C-band): 1530 nm, 1550 nm, and 1570 nm, as shown in Table 5.1. For TM incidence, the device works as a nice mirror at all the wavelengths

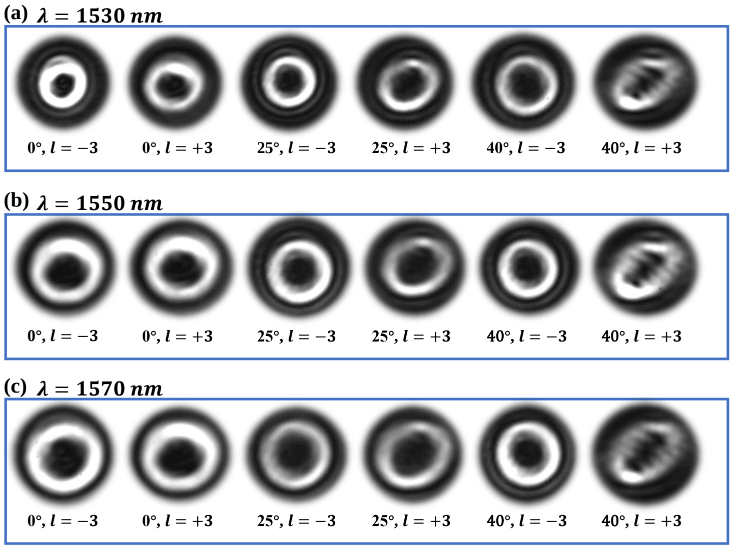

Figure 5.5: Detected intensity patterns of the optical vortices generated by the fabricated device.

and incident angles. For the desired y-polarized incidence, the reflected power is uniformly distributed in the ±1 grating orders at the design wavelength 1550 nm for 25° incidence. There are small power imbalances (less than 20%) between the grating orders at 1530 nm and 1570 nm, which is acceptable. When a large incident angle of 40° is applied, the power efficiency of the +1 grating order drops severely. Moreover, the 0 grating order, which is supposed to be strongly suppressed, occurs. However, the power efficiency of the -1 grating order does not change much due to the small reflection angle. These results are caused by the performance degradation of the metasurface when reflecting at large angles, which has already been observed in Chapter 4. Nevertheless, good grating performance is demonstrated in C-band, with a large incident range of at least 25°.

5.4.2 Optical OAM modes generation

As discussed before, the designed metasurface-based 1×2 Dammann vortex grating has an intrinsic topological charge of +3. $l = \pm3$ OAM modes can be

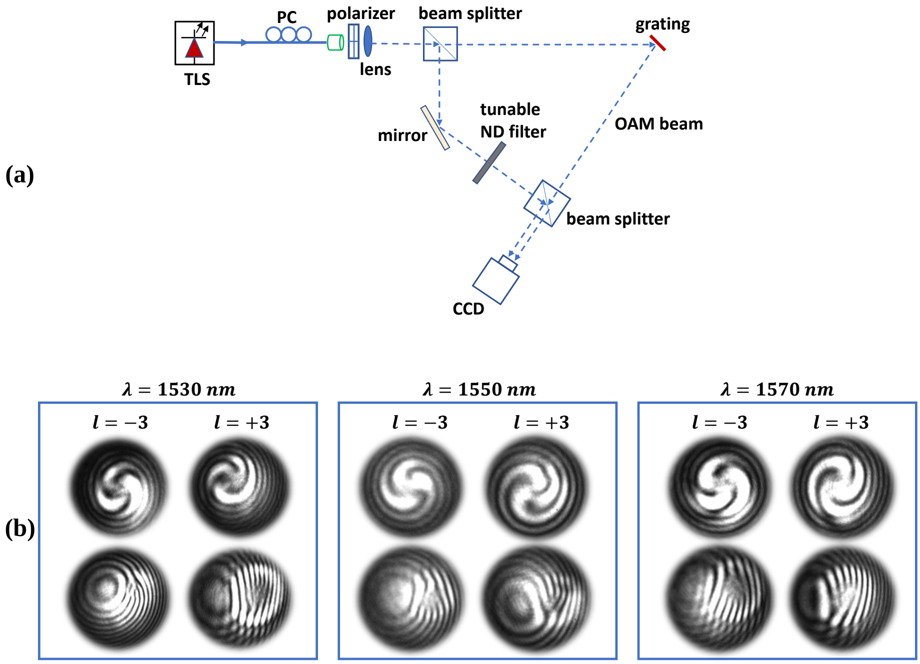

Figure 5.6: (a) Experimental setup for the topological charge detection. CCD: charge-coupled device, ND filter: neutral-density filter, PC: polarization controller, TLS: tunable laser source. (b) Detected interference patterns of the generated OAM modes ($\theta_i = 25°$).

generated in the ±1 grating orders respectively, under the illumination of a y-polarized Gaussian beam (or plane wave). The intensity patterns of the optical vortices generated from the collimated Gaussian incident beam can be directly detected with a CCD image sensor, as shown in Figure 5.5. The incident angles are set to 0°, 25°, and 40° at each of the three wavelengths (1530 nm, 1550 nm, and 1570 nm). When a large incident angle of 40° is applied, the generated optical vortices of +1 grating order degrade severely, the ring is distorted and almost broken. Such degradation is predictable because the reflection angle is quite large (71.1° as shown in Figure 5.4(a)) in this case. For other cases, clear optical vortices are observed.

The experimental setup shown in Figure 5.6(a) is built to further determine the topological charges of generated OAM beams. The desired y-polarized

Gaussian beam is generated by combining a tunable laser source, a polarization controller, a free-space polarizer, and a collimator. It is then divided by a free-space beam splitter. One of the beams is launched onto the grating at the desired incident angle to generate OAM beams; the other beam is re-directed by a mirror (or mirrors) and then combined with one of the generated OAM beams through another free-space beam splitter. Finally, the combined beams are launched onto a CCD image sensor to detect interference patterns.

Here, the incident angle is set to 25°, and the interference patterns are measured at the three wavelengths, as shown in Figure 5.6(b). When the OAM beam and the Gaussian beam are well adjusted to coaxial transmission, spiral interference patterns can be obtained, as shown in the top row of Figure 5.6(b). When there is an angle between the transmission directions of the two beams, pitch-fork hologram patterns can be obtained, as shown in the bottom row of Figure 5.6(b). As can be seen, clearly $l = \pm 3$ OAM modes are obtained at all the wavelengths. Therefore, a metasurface-based Dammann grating, which has an intrinsic topological charge of +3, is demonstrated to have high efficiency (around 60%), broadband operation (C-band), and a large incident angle range (at least 25°).

5.5 Transmission experiment

An optical OAM beam transmission experimental setup with 40-Gbps on-off keying (OOK) modulation is built by using the fabricated grating, as shown in Figure 5.7. A tunable laser source (TLS) with a 13.5-dBm output optical power is used to generate the optical carrier in the communication control center, which is then modulated by a broadband Mach-Zehnder modulator (MZM) with >32 GHz bandwidth. The electrical OOK data are produced by a bit-error-ratio tester (BERT) at 40 GSa/s to drive the MZM after amplification. Thus, the achieved transmission data rate is 40 Gbps. The modulated optical signal is amplified by an erbium-doped fiber amplifier (EDFA) to 13 dBm and then launched into a 1.7-km single-mode fiber (SMF). A polarization controller (PC) combined with a free-space polarizer is used to generate the desired polarization states. The Gaussian beam is launched into free space via a collimator (the focal length is 18 mm) with a measured power below 10 dBm which meets the requirement of human eye safety. The light is further collimated by a lens and then launched onto the fabricated grating, resulting in $l = \pm 3$ OAM beams or a specularly reflected Gaussian beam (depending on the incident polarization). After 0.2-m free-space transmission, the output beams are respectively coupled into a short

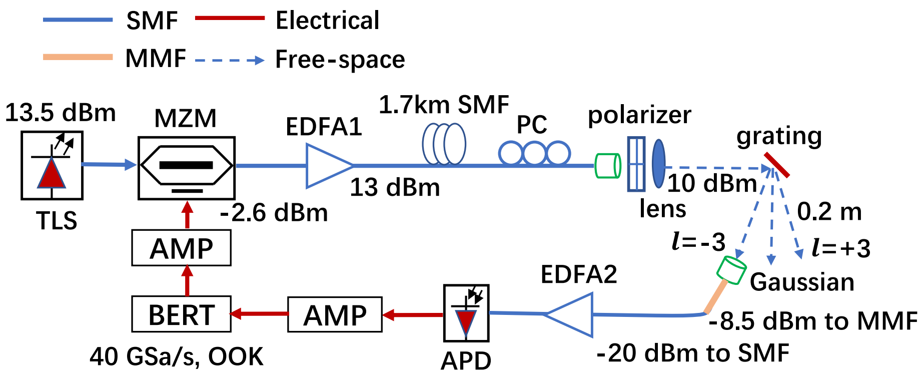

Figure 5.7: Experimental setup of the 40-Gbps OAM wireless transmission. AMP: amplifier, APD: avalanche photodiode, BERT: bit-error-ratio tester, EDFA: erbium-doped fiber amplifier, MMF: multi-mode fiber, MZM: Mach-Zehnder modulator, PC: polarization controller, SMF: single-mode fiber, TLS: tunable laser source.

section of multi-mode fiber (MMF) and then an SMF via another collimator. The received optical power is amplified and then detected by an avalanche photodiode (APD). The amplified output electrical OOK signal is then fed into the receiver of the BERT for further signal processing and BER calculation.

In the transmission experiment, the incident angle (θ_i) is set to 25° and 40°; the wavelength is 1550 nm. Figure 5.8 illustrates the BER performance of the 40-Gbps OOK signals as a function of the input optical power of the APD. By adjusting the incident polarization state to the desired one, $l = \pm 3$ OAM beams and a specularly reflected Gaussian beam are generated, transmitted, and measured at the receiver end. As a comparison, the optical powers launched into the EDFA2 for both the OAM beams and Gaussian beam are set to -20 dBm, which is limited by the coupled optical power of the +3 OAM beam at 40° incidence. For other OAM beams, the coupled optical power is typically -15 dBm. There is only a small difference between the BER performance of the OAM and Gaussian beams at both incident angles, which indicates the good quality of the generated optical OAM beams since they can be coupled into an SMF and support high-speed transmission. The high coupling loss of an OAM beam to an SMF suggests that in a Dammann vortex grating-based optical OAM modes demultiplexing system, this coupling method can be used as a mode filter to select the demultiplexed OAM mode because it is converted into a Gaussian

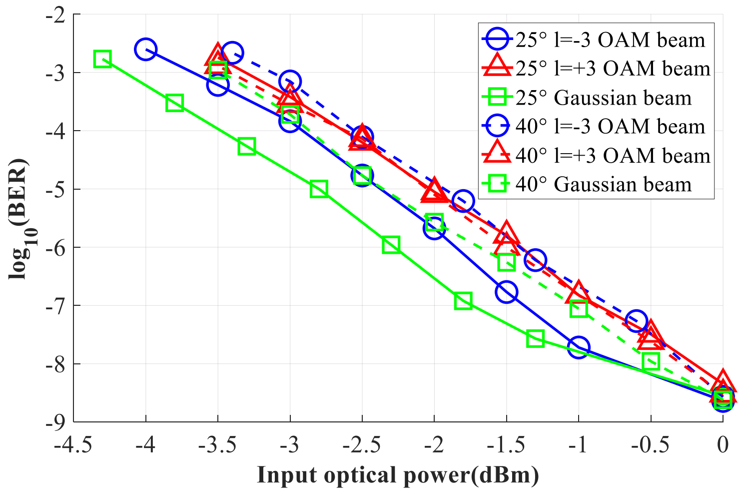

Figure 5.8: BER performance of the 40-Gbps OAM wireless transmission. The incident angle is set to 25° and 40°; the wavelength is 1550 nm.

beam that can be efficiently coupled into an SMF.

5.6 Discussion

Due to the polarization dependence of the designed phase units, the fabricated device only works as the desired Dammann vortex grating at y-polarized incidence. As for x-polarization, it works as a mirror. Such a feature can be exploited to achieve polarization-controlled beam steering or optical switching. However, a drawback is that it hinders the combination of OAM multiplexing and polarization multiplexing because two gratings are needed to multiplex OAM modes for two orthogonal polarization states, respectively. Moreover, this spatially separated multiplexing process leads to the additional complexity of combining the two beams into the coaxial transmission. To enable another polarization state, a new phase unit is carefully designed to achieve a π phase difference between its phase response under x and y-polarized illuminations, as shown in Figure 5.9. The new phase unit has the following structure parameters: $S_x = 250$ nm, $S_y = 500$ nm, $H = 200$ nm, $g = 160$ nm, $l_x = 100$ nm, $h = 55$ nm, and $l_y = 410$ nm. In Figure 5.9, the right phase unit is a 90°-rotation of the

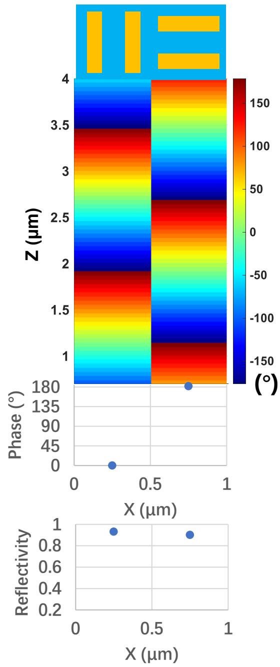

Figure 5.9: Simulated scattered E_x phase patterns and reflectivity of the phase units under the illumination of a normally incident x-polarized plane wave ($\lambda = 1550$ nm).

left one. The simulation is only performed in the x-polarization case because rotating polarization state by 90° is equivalent to exchanging the positions of the two phase units. Therefore, the phase difference between the scattered E_y phase patterns under a y-polarized illumination is $-\pi$. Besides, the two phase units have almost the same high reflectivity (>90%).

Filling the designed phase pattern shown in Figure 5.3(c) with the new phase units brings us a 1×2 Dammann vortex grating with +3 topological charge at x-polarized incidence and -3 topological charge at y-polarized incidence, which enables simultaneously multiplexing of OAM modes and polarization states. Based on the achieved results, this new design is promising and will be fabricated and experimentally investigated in future work.

Recently, instead of converting an OAM beam into a Gaussian beam or interfering OAM beams with other beams, R.M. Kerber et al. theoretically proposed and proved a remarkable new method to directly read out the extra information encoded in OAM beams [172, 173]. By using rotationally arranged plasmonic nano-antennas, the phase information in an OAM beam can be converted into spectral information, and hence different OAM modes can be distinguished. Behind this method is the dichroism of a plasmonic nano-structure interacting with OAM light, which has also been revealed in the work of R.M. Kerber et al.. The results pave a new way for OAM modes demultiplexing. Therefore, implementing plasmonic metasurfaces having OAM dichroism would be an attractive research topic for future work.

5.7 Conclusion

By combining the Dammann vortex grating approach, which is capable of simultaneously multiplexing/demultiplexing massive OAM beams with independent modulation, and the metasurface techniques developed in Chapter 4, a metasurface-based 1×2 Dammann vortex grating, which has an intrinsic topological charge of +3, is designed, fabricated, and measured. For the fabricated device, when illuminated by a y-polarized Gaussian beam (or plane wave), clear $l = \pm 3$ optical OAM beams are generated and detected with uniform energy distribution, and the total energy efficiency is as high as about 60%. With the fabricated grating, $l = 3$ and $l = -3$ optical OAM beams are generated and transmitted respectively through 0.2-m free space with a 40-Gbps data rate. The obtained results demonstrate metasurface as a highly efficient, flexible, and low-cost approach for Dammann vortex grating implementation, providing a new powerful device for Dammann vortex grating-based optical OAM modes multiplexing/demultiplexing.

Chapter 6

Summary and Future Outlook

6.1 Summary

In the proposed converged fiber-wireless indoor network, wireless services of 5G cellular, Wi-Fi, and optical wireless communication (OWC) networks are processed in the residential gateway centrally. All signals are then modulated onto optical carriers and transmitted to access points through the optical fiber by using radio-over-fiber (RoF) technology. This architecture makes high-performance optoelectronic devices for the RoF system and photonic techniques for spatial multiplexing for high spatial density delivery essential. In this thesis, several novel photonic techniques have been developed to enhance the RoF system and spatial multiplexing in the converged fiber-wireless indoor network to further boost the network capacity and allow high user densities. The activities have resulted in the following achievements:

6.1.1 Low-cost high-performance optical frequency comb source for indoor RoF system

In Chapter 2, an O-band optical frequency comb source based on a passively mode-locked InAs quantum dot (QD) laser is designed, fabricated, and demonstrated for two key requirements from the RoF system of the converged fiber-wireless indoor network: 1) Low-cost high-bandwidth optoelectronic devices with excellent linearity and low phase noise are key enablers for an indoor RoF system. Among them, the optical frequency comb source plays a key role in both radio-frequency (RF) carrier generation and phase-coherent dense wavelength-division multiplexing (DWDM). 2) Low cost is required for an indoor network because the costs are borne by building owners/users, which is different from operator-owned outdoor networks.

First, an InAs QD wafer structure having a larger than the usual number of QD layers and with higher dot area density is grown on a Si-doped GaAs (001) substrate using molecular beam epitaxy to achieve the high optical gain which is desired for high-temperature operation of QD lasers. For the growth of the active region, without adopting a conventional InAs/InGaAs/GaAs dot-in-a-well structure, where the InAs layer is sandwiched by InGaAs layers, in our work, InAs QDs are formed self-assembly on a GaAs surface by depositing a three-monolayer InAs QD layer directly on the GaAs surface. The initial InAs QDs are then covered by a 3.7 nm InGaAs strain-reducing layer, and such coverage growth conditions are also optimized to suppress ad-atom migration during the coverage. By doing so, the original uniformity can be kept without sacrificing dot density and multilayer structures. As a result, an active region comprising a tenfold layer stack of InAs QDs is obtained, and the dot density as high as 5.9×10^{10} cm^{-2} is typically achieved. With the optimized growth condition, despite the achieved high dot density, the photoluminescence full width at half maximum (governed by the inhomogeneous broadening due to size and shape distribution of the QDs) remains as low as 30 meV. The combined effects lead to a great enhancement of integrated photoluminescence intensity of the optimized sample. In addition, the quantized-energy difference between the ground state and the first excited state increases to 88 meV. The enhanced energy separation plays a vital role in effectively suppressing the carrier overflow and Auger recombination at elevated temperatures.

Second, the mode-locked InAs QD laser is fabricated from the wafer described above in our clean room, and then measured. Due to the high dot density and engineered quantized energy difference between the ground state and the first excited state, the designed device achieves an ultra-stable repetition rate (corresponding to mode spacing between adjacent tones in the frequency domain) over the widest temperature range yet reported for any type of mode-locked laser (MLL). The fabricated device exhibits stable mode-locking at a fundamental repetition rate of 25.5 GHz with pulse widths of less than 9 ps at temperatures ranging from 20°C to 120°C. Over the 100°C temperature range, the designed tone frequency spacing is nearly unaltered (varies within 0.07 GHz), and stable mode-locking is simply achieved by only changing the biasing conditions of the gain section while the absorber is reverse-biased at a constant voltage. >10 dBm output power is obtained at 120 mA injection current. The measured threshold current is around 20 mA. The device also shows a relatively broad -6 dB comb bandwidth of 4.81 nm, offering a maximum of 31 optical channels at 100°C with a low average relative intensity noise value of less than -146 dBc/Hz.

The obtained results pave the way for utilizing ultra-stable, easy-operating, uncooled QD MLLs as efficient frequency comb sources for broad-bandwidth, large-scale, low-cost phase-coherent DWDM multi-channel indoor RoF systems.

6.1.2 Photonics techniques for spatial multiplexing in the converged fiber-wireless indoor network

- **Photonics techniques for RF-OAM modes generation/detection**

  To push the realization of RF orbital angular momentum (OAM) multiplexing a step forward, this work provides a novel electrically-controlled optical broadband phase shifter (ECO-BPS) for circular antenna array (CAA)-based RF-OAM modes generation and detection, which solves the limited bandwidth and bulk volume problems of microwave phase shifters, and the narrow-bandwidth problem of optical true time delay (OTTD) phase shifters.

  In Chapter 3, first, the operation principle and the design of the proposed ECO-BPS are comprehensively presented. The fabricated device is measured to provide 0-2π constant phase shifts with low phase deviation over a broad frequency band from 12 GHz to 20 GHz. 17 equally spaced phase shifts covering 2π are generated by applying 16 direct-current levels to the proposed phase shifter (the 17^{th} phase shift is synthesized by fitting the measured data to avoid the phase jump in the measurement when the phases are close to π or -π). With the obtained 17 phase shifts and a 17-element CAA, the generation/detection of 16 RF-OAM modes (up to ±8) can be supported. The proposed phase shifter can theoretically provide a constant phase shift over the entire frequency band. In practice, the standard deviation of the measured phase error is 3.44°, which comes from three main possible sources: 1) the phase variation induced by residual upper sidebands. 2) the random phase error induced by noise. 3) the phase error caused by the time variation of the optical notch filter. By integrating the optical notch filter and the parallel Mach-Zehnder modulator in a single chip, sources 1) and 3) can be largely reduced.

  Second, to investigate the mode purity of the OAM generated with the proposed phase shifter, $l = 1$ OAM modes are numerically synthesized with three cases of phase shifts: the measured phase shifts, ideal constant phase shifts, and ideal OTTD phase shifts. In each case, $l = 1$ OAM modes are generated at 12, 14, 16, 18, and 20 GHz, respectively, by using the 17-element CAA. Then, all the modes are compared in terms of amplitude profiles, phase front profiles, and spiral spectrum. The numerical results show that high-quality OAM modes are obtained at all the frequencies with the measured phase shifts, and about 99% beam energy is carried by the desired $l = 1$ OAM mode, resulting in high mode purity.

Third, to further demonstrate the feasibility of the proposed phase shifter in applications of broadband OAM multiplexing, the crosstalk, which is caused by the phase error, between $l = \pm 1$ multiplexed OAM modes is numerically investigated through the following steps: 1) $l = \pm 1$ multiplexed OAM modes are synthesized with the previously mentioned three cases of phase shifts. In each case, the synthesis is performed at 12, 14, 16, 18, and 20 GHz, by using the 17-element CAA. 2) For each case, at each frequency, the multiplexed OAM modes are demultiplexed by using a 1×2 Dammann vortex grating-based OAM modes demultiplexing system, and then the crosstalk is quantified. Dammann vortex grating is chosen because it is capable of encoding OAM topological charges in its diffraction orders with high energy efficiency, which can be used to simultaneously multiplex/demultiplex massive OAM modes with independent modulation. Besides, as a 0-π binary-phase grating, Dammann vortex grating is easy to fabricate, making it more practical. 3) The obtained crosstalk of the three cases is compared at each of the frequencies. The numerical results show that with the measured phase shifts, the obtained crosstalk is as small as around -27 dB over the entire bandwidth, while the crosstalk of the ideal OTTD phase shifts increases rapidly with the frequency due to its phase-frequency dependence, and becomes significantly larger starting from 14 GHz.

These measurements and numerical simulation results demonstrate the proposed ECO-BPS is a superior approach to generate highly pure OAM modes for broadband RF-OAM multiplexing.

- **Photonics techniques for optical beam steering**

  Optical beam steering is the essential technique to enable energy-efficient high-speed beam-steered infrared (IR) light communication, attracting the interest of researchers and engineers from the entire world. This work proposes a novel solution to IR beam steering based on a passively field-programmable metasurface.

In Chapter 4, first, a metasurface-based two-dimensional (2D) IR beam-steering system is proposed. And its system configuration method is developed to achieve full coverage for a plane area. The proposed beam-steering system is composed of an arrayed waveguide grating router (AWGR)-based beam-steering module, a liquid-crystal polarization controller, and a metasurface polarization beam splitter. It has two tuning schemes: wavelength tuning and polarization tuning. The polarization tuning is achieved by using the metasurface polarization beam splitter in conjunction with the liquid-crystal polarization controller. The wavelength tuning is enabled by the AWGR-based beam-steering module. With these two tuning schemes, the beam coverage area can be greatly expanded. The proposed system keeps all the advantages of AWGR-based beam-steering approaches. Furthermore, the grating loss existing in SLM-based and grating-based beam-steering approaches is avoided by using the metasurface. Therefore, the proposed system has the scalability to support multiple beams, flexibility to steer the beam, high optical efficiency, and a large coverage area.

Second, to prove the feasibility of the proposed polarization-wavelength-controlled 2D IR beam-steering solution, a passive gap-surface plasmon metasurface is designed to realize the polarization beam splitter due to its advantages of high efficiency, excellent control over the reflected or transmitted light, and low manufacturing cost. The designed device is fabricated in our clean room and then measured under comprehensive 2D incidence at three wavelengths: 1530 nm, 1550 nm, and 1565 nm, corresponding to C-band. In the measurement, an incident direction is described by a polar angle and an azimuthal angle of the spherical coordinate system. The measured angle relations between incident and reflection agree very well with the theory and numerical simulation. The device is measured to have a large incident polar angle range of up to 35° with >50% (-3 dB) energy efficiency. And the measured overall isolation between the two working orthogonal polarization states is 15 ± 5 dB for all the three wavelengths and incident directions. The measurement results prove the reflection characteristics and the good performance of the designed metasurface polarization beam splitter in a broad bandwidth from 1530 nm to 1565 nm (C-band). Moreover, by using a free-space polarizer and a fiber polarization controller, polarization-controlled 2D IR beam-steering is verified by changing the polarization states of incident beams in multiple incident planes (determined by azimuthal angles) and polar angles.

Third, by using the designed metasurface and the same basic parameters as the AWGR-based beam-steering module in Koonen et al. [131]: 51.2 mm focal length, 21% defocusing, and 12-cm spot size, a system example with an f/0.95 lens and a C-band 96-port AWGR (90 ports are used) is designed to achieve full coverage area of 1.2×2.9 m^2 with room height 2.4488 m (equivalent with a beam-steering angle range of $\pm13.8^\circ\times49.8^\circ$). A larger coverage area is obtained with fewer AWGR ports and a smaller wavelength tuning range (only C-band). Since the extra loss introduced by the metasurface is less than 50% according to the measurement results, and the AWGR-based beam-steering module with the same basic parameters has been demonstrated in [131], the feasibility of the designed system can be verified.

Finally, a proof-of-concept experimental setup is built using the fabricated metasurface. Polarization-controlled beam steering experiments are performed, and a 1.2-m 20-Gbps beam-steered IR wireless link is achieved with 4-level pulse amplitude modulation (PAM-4). The obtained results open a new way for utilizing high-efficiency, easy-operating, simple-structure, easy-to-fabrication passive metasurfaces for broad-bandwidth, large-coverage-area, low-cost optical beam steering.

- **Photonics techniques for optical OAM modes multiplexing/demultiplexing**

  Dammann vortex grating-based OAM modes multiplexing/demultiplexing techniques show a practical path toward an OWC capacity of Pbps level due to their capabilities of simultaneously multiplexing/demultiplexing massive OAM beams with independent modulation. This work presents a low-cost and highly efficient way to implement Dammann vortex gratings by taking advantage of the unprecedented metasurface features presented in Chapter 4, such as high efficiency, easy-to-fabrication, compact in size, and free of grating loss.

  In Chapter 5, first, by combining the Dammann vortex grating approach and the metasurface techniques presented in Chapter 4, a metasurface-based 1×2 Dammann vortex grating, which has an intrinsic topological charge of 3, is designed for optical $l=\pm3$ OAM modes multiplexing/demultiplexing. Since a Dammann vortex grating is a 0-π binary-phase grating, the designed grating can be simply implemented by filling the desired grating phase patterns with the designed sub-wavelength metasurface 0 and π phase units. Moreover, by using the developed metasurface phase units to compose corresponding phase patterns, Dammann vortex gratings for multiplexing/demultiplexing other OAM modes can also be easily realized. Such pixel-filling method brings advantages of flexibility, stability, and low cost (one set of phase units and fabrication process for different Dammann vortex gratings).

Second, the designed device is fabricated in our clean room, and then measured at the desired working polarization state and three wavelengths: 1530 nm, 1550 nm, and 1570 nm, covering C-band. The fabricated grating shows diffraction angle relations almost the same as theoretical results. The measured energy efficiency is as high as around 60% for a large incident range of 25° at all three wavelengths. Besides, clear intensity profiles and interference patterns of $l = \pm 3$ OAM modes are observed over a broad bandwidth at a large incident range of 25°. Therefore, the fabricated grating is demonstrated to have high efficiency, broadband operation, and a large incident angle range (at least 25°). The feasibility of the fabricated device for optical $l = \pm 3$ OAM modes multiplexing/demultiplexing is verified.

Finally, with the fabricated grating, a 0.2-m 40-Gbps OAM beam transmission experiment is performed with on-off keying modulation. The obtained results demonstrate metasurface as a highly efficient, flexible, and low-cost approach for Dammann vortex grating implementation, providing a new powerful device for Dammann vortex grating-based optical OAM modes multiplexing/demultiplexing.

6.2 Future outlook

6.2.1 Low-cost ultra-broadband directly modulated laser for indoor RoF system

For optoelectronic devices in RoF systems, in addition to the optical frequency comb source discussed in Chapter 2, directly modulated lasers (DMLs) also play an important role. In an RoF system, intensity-modulation and direct-detection (IM/DD) technique is used to directly modulate RF signals onto optical carriers because the configuration of such technique is simple, leading to the advantages of low cost, low power consumption, compact in size, and convenience to integrate into an optical module. Among IM/DD configurations, the DML-based IM/DD technique, in which DML acts as the coherent light source and the modulator, is highly preferred due to its advantages of low cost, low system complexity, and high energy efficiency, which perfectly match the requirements of the converged fiber-wireless indoor networks, in which a large number of high-speed short-distance optical interconnections are needed. However, the future demand for higher data rates is challenging the existing DML-based IM/DD system, and the main bottleneck is the modulation bandwidth of the DML. Therefore, it is attractive to develop low-cost ultra-broadband DMLs for future indoor networks.

In order to increase the modulation bandwidth, both the damping frequency f_d, which leads to an ultimate limit in the modulation bandwidth, called K-limited bandwidth ($\sqrt{2}f_d$), and the relaxation resonance frequency f_R of DMLs need to be increased [174]. To increase f_d, laser material of high differential gain and low nonlinearity of gain is required. And f_R can be enhanced by decreasing the mode volume to obtain large optical confinement, and by increasing the differential gain. Therefore, a route of improving the modulation bandwidth of DMLs can be seen. In terms of materials, compared to the conventional InGaAsP, the InGaAlAs material system has better electron confinement due to its larger conduction band offset, which leads to an increase in the differential gain [175]. Thus, InGaAlAs is preferred for high-speed DMLs [176–182]. In terms of laser structure, two main approaches are taken: 1) short-cavity structure [176–178] and 2) distributed feedback (DFB)-based or distributed Bragg reflector (DBR)-based coupled-cavity structure [179–185]. With a short active section, the mode volume can be compressed effectively. However, due to the K-limited bandwidth, the modulation bandwidth of the short-cavity lasers is limited to <40 GHz. To overcome this limitation, coupled-cavity structures are introduced. With an additional passive feedback cavity, the active section length can be reduced beyond the limit of the cleaving process, and the optical feedback is increased to reduce the threshold gain. Moreover, detuned loading effect and photon-photon resonance effect can be combined to realize DMLs having ultra-broad modulation bandwidth [182–185].

In [182], III-V-membrane on SiC technology is used to achieve large optical confinement in the active region and small differential gain reduction at a high injection current density, which is enabled by the low-refractive-index and high-thermal-conductivity of SiC. 321.24-Gbps discrete multitone [186] and 239.3-Gbps PAM-4 [187] transmissions over 2-km standard single-mode fiber have been demonstrated with the DML in [182], whose modulation bandwidth is up to 108 GHz. However, the fabrication process of this membrane laser is challenging. To heterogeneously integrate the membrane laser on SiC, a direct bonding process without degrading the crystal quality of the active multiple-quantum-well (MQW) layer is needed. In addition, Zn thermal diffusion and Si ion implantation are needed to form the lateral p–i–n junction after the regrowth of the buried heterostructure. The process complexity could increase the cost and limit the mass production and application of the membrane laser, which is an important challenge to address in the future.

On the other hand, with the DFB+reflection (DFB+R) structure [184, 185], a DML-based IM/DD system with beyond 400 Gbps data rate is demonstrated [183]. 405.1-Gbps, 389-Gbps, and 368.8-Gbps data rates are achieved with 5 km, 10 km, and 15 km standard single-mode fiber transmission, respectively. The DFB+R laser has a conventional buried heterostructure (lower process complexity) and 75-GHz broad modulation bandwidth. To further reduce the cost, the coupled-cavity laser with ridge waveguide structure is an attractive research direction. Nevertheless, both passive feedback structures (such as waveguide and DBR mirror) and active section need to be integrated into a high-speed coupled-cavity DML. Hence, the mature and low-cost active-passive-hybrid-integration technology is essential to the development and large-scale application of the high-speed coupled-cavity DML in the future.

Based on the advanced InP-membrane on silicon technology [188] developed by the Institute of Photonic Integration, Eindhoven University of Technology, and the design and fabrication techniques developed in Chapter 2, low-cost ultra-broadband membrane DMLs with aforementioned coupled-cavity structures are promising to be realized.

6.2.2 Dynamic metasurfaces for optical beam manipulation

It is shown in Chapter 4 and Chapter 5 that metasurfaces can be used as powerful tools for optical beam manipulation, including but not limited to beam steering and OAM modes multiplexing/demultiplexing. However, in this thesis, only passive metasurfaces have been used. Their structures and functions are fixed after fabrication and cannot be reconfigured in any way, which limits their applications in optical beam manipulation. Therefore, dynamic metasurfaces, whose metasurface pixels can be dynamically altered and their light-scattering behaviors can be reconfigured, are worth for future study as they offer promising and ultimate solutions for arbitrary manipulation of optical beams. The realization of dynamic metasurface pixels needs both appropriate subwavelength resonant nanostructures and the broad tunability of their resonant behaviors. Various manipulation methods have been applied to enable dynamic metasurfaces for optical beam steering, including:

- Carrier density modulation [189, 190], which is based on the fact that in a doped semiconductor or conducting oxide, the change of the carrier density results in the variation of the complex refractive index [191]. In [189], a reconfigurable metasurface consisting of gate-tunable graphene-gold resonators is demonstrated. It can be electronically tuned by modulating the charge carrier density of the graphene layer via electrostatic gating in a parallel plate capacitor configuration. For the graphene-gold resonator, a 237° phase modulation range is achieved. And an absolute beam steering efficiency of 1% for reflected light for angles up to 30° is demonstrated by antenna array calculations at 8.5 μm wavelength. In [190], the tunability arises from the carrier density modulation of conducting oxide layers incorporated into metasurface antenna elements. A 180° phase modulation range is obtained for an antenna element, and a period tunable reflective phase grating is proposed for step-by-step one-dimensional beam steering with an angle range of >40° at 1.55 μm wavelength.

- Liquid crystal-based approach [192], in which nano-antennas are integrated into a liquid crystal-based spatial light modulator. By modifying the liquid crystal orientation around the nano-antennas with external electrical signals, the local environment and resonances of nano-antennas can be controlled. In [192], 2π-phase coverage is achieved in 650-675 nm wavelength for the designed TiO_2 nano-antenna. And the one-dimensional active beam steering with >35% efficiency and 11° deflection angle is achieved with the proposed metasurface-based transmissive spatial light modulator.

- Mechanical motion-based approach [193], in which nano-antennas are fabricated on a stretchable polydimethylsiloxane substrate to form a metasurface. The stretching of the substrate changes the lattice constant of the antenna array and enables the tuning of the spatial phase distribution. In [193], a mechanically reconfigurable transmissive metasurface based on Au nanorod antennas (2π-phase coverage) is demonstrated to steer its anomalous refraction from 11.4° to 14.9° at 632.8 nm wavelength.

- Stark effect-based approach [137]. Based on the tunable optical response from the quantum-confined Stark effect [194], which enables the electro-optic modulation of the complex refractive index of MQWs, the amplitude and phase of the reflected light from the III–V MQWs-based nanoresonators can be adjusted by applying a DC electric field across the nanoresonators. In [137], an all-dielectric tunable metasurface based on resonators having a layer stack of MQWs/distributed Bragg reflector/GaAs substrate is proposed, and it is configured as a period tunable reflective phase grating to verify step-by-step one-dimensional beam steering at 917 nm wavelength. The observed beam steering is efficiency-limited because the phase modulation range of the resonator is only from 0° to 70°.

- Phase change material-based approach [136, 138, 195–198]. Phase change material (PCM) exhibits a significant difference in optical properties between the amorphous and crystalline states. Therefore, by controlling the phase transition process through an external thermal, electric, or optical stimulus, the response of a PCM-based resonator can be changed. Based on this feature, PCM is widely considered for dynamic metasurface realization. In [138], an electric heater controlled-beam-steering metasurface based on volatile PCM vanadium dioxide (VO_2) is demonstrated with 44° 2D beam deflection at 100 GHz. Because germanium (Ge)-antimony (Sb)-telluride (Te) alloys (GST alloys) have many desirable properties, such as robust switching over a large number of cycles, high switching speed, low power consumption, large optical contrast between two phases, and non-volatile switching, GST-based dynamic metasurface has attracted a lot of attention [136,197,198]. In [136], up to 40° beam steering of anomalous reflection is numerically verified with limited reflection efficiency at 1550 nm wavelength. And authors in [197] numerically demonstrate beam steering angles of 11° for transmitted waves and 22° for reflected waves in the mid-IR region.

Those pioneering works light up the dawn of achieving arbitrary high-speed beam manipulation by using dynamic metasurfaces. The challenges are worth our efforts in the future. Among the materials discussed above, GST alloys are the most promising ones to be further investigated to create dynamic metasurfaces because of their non-volatile switching feature. In order to achieve arbitrary manipulation of optical beams, each sub-wavelength resonator on the metasurface needs to be configured individually. However, in the optical range, applying an individual, uninterrupted control signal to each resonator is unrealistic due to the huge number and extremely small size of resonators. This makes non-volatile switching essential. Dynamic metasurfaces with non-volatile resonators can be conveniently programmed to achieve desired functions because resonators remain in the desired state after any external stimulus is removed.

Bibliography

[1] Wei Xiang, Kan Zheng, and Xuemin Sherman Shen. *5G mobile communications*. Springer, 2016. (Cited on page 2.)

[2] M Series. Imt vision–framework and overall objectives of the future development of imt for 2020 and beyond. *Recommendation ITU*, 2083:0, 2015. (Cited on pages 2, 3, and 4.)

[3] M Series. Imt traffic estimates for the years 2020 to 2030. *Recommendation ITU*, pages 2083–0, 2015. (Cited on page 3.)

[4] Huawei. Huawei global industry vision (giv) 2025. *White Paper*, 2019. (Cited on page 4.)

[5] M Series. Minimum requirements related to technical performance for imt-2020 radio interface (s). *Report*, pages 2410–0, 2017. (Cited on page 4.)

[6] Mansoor Shafi, Andreas F Molisch, Peter J Smith, Thomas Haustein, Peiying Zhu, Prasan De Silva, Fredrik Tufvesson, Anass Benjebbour, and Gerhard Wunder. 5g: A tutorial overview of standards, trials, challenges, deployment, and practice. *IEEE journal on selected areas in communications*, 35(6):1201–1221, 2017. (Cited on page 4.)

[7] ITU-R. Report of the cpm on operational and regulatory/procedural matters to the world radio communication conference. 2015. (Cited on page 5.)

[8] Yi Wang, Jian Li, Lei Huang, Yao Jing, Andreas Georgakopoulos, and Panagiotis Demestichas. 5g mobile: Spectrum broadening to higher-frequency bands to support high data rates. *IEEE Vehicular technology magazine*, 9(3):39–46, 2014. (Cited on page 5.)

[9] Cihat Seker, Muhammet Tahir Güneser, and Turgut Ozturk. A review of millimeter wave communication for 5g. In *2018 2nd International Symposium on Multidisciplinary Studies and Innovative Technologies (ISMSIT)*, pages 1–5. Ieee, 2018. (Cited on page 5.)

[10] Theodore S Rappaport, George R MacCartney, Mathew K Samimi, and Shu Sun. Wideband millimeter-wave propagation measurements and channel models for future wireless communication system design. *IEEE transactions on Communications*, 63(9):3029–3056, 2015. (Cited on page 5.)

[11] Ahmed M Al-Samman, Tharek Abd Rahman, MHD Hindia, Abdusalama Daho, and Effariza Hanafi. Path loss model for outdoor parking environments at 28 ghz and 38 ghz for 5g wireless networks. *Symmetry*, 10(12):672, 2018. (Cited on page 5.)

[12] Ferdous Hossain, Tan Kim Geok, Tharek Abd Rahman, Mohammad Nour Hindia, Kaharudin Dimyati, Sharif Ahmed, Chih P Tso, and Noor Ziela Abd Rahman. An efficient 3-d ray tracing method: prediction of indoor radio propagation at 28 ghz in 5g network. *Electronics*, 8(3):286, 2019. (Cited on page 5.)

[13] Bruno Suard, Guanghan Xu, Hui Liu, and Thomas Kailath. Uplink channel capacity of space-division-multiple-access schemes. *IEEE Transactions on Information Theory*, 44(4):1468–1476, 1998. (Cited on page 6.)

[14] Saurabh Patel, Malhar Chauhan, and Kinjal Kapadiya. 5g: Future mobile technology-vision 2020. *International Journal of Computer Applications*, 54(17), 2012. (Cited on page 6.)

[15] Erik G Larsson, Ove Edfors, Fredrik Tufvesson, and Thomas L Marzetta. Massive mimo for next generation wireless systems. *IEEE communications magazine*, 52(2):186–195, 2014. (Cited on page 6.)

[16] Akhil Gupta and Rakesh Kumar Jha. A survey of 5g network: Architecture and emerging technologies. *IEEE access*, 3:1206–1232, 2015. (Cited on pages 7 and 8.)

[17] wikipedia. IEEE 802.11a. https://en.wikipedia.org/wiki/IEEE_802.11a-1999, 1999. (Cited on page 8.)

[18] wikipedia. IEEE 802.11n. https://en.wikipedia.org/wiki/IEEE_802.11n-2009, 2009. (Cited on page 8.)

[19] wikipedia. IEEE 802.11ac. https://en.wikipedia.org/wiki/IEEE_802.11ac, 2013. (Cited on page 8.)

[20] wikipedia. IEEE 802.11ad. https://en.wikipedia.org/wiki/IEEE_802.11ad, 2012. (Cited on page 8.)

[21] Boris Bellalta. Ieee 802.11 ax: High-efficiency wlans. *IEEE Wireless Communications*, 23(1):38–46, 2016. (Cited on page 9.)

[22] Fernando Rivasplata. 802.11ax Overview. https://tech-brain.us/?p=451, 2020. (Cited on page 9.)

[23] Ton Koonen. Indoor optical wireless systems: technology, trends, and applications. *Journal of Lightwave Technology*, 36(8):1459–1467, 2017. (Cited on pages 10, 11, 12, and 54.)

[24] Dilukshan Karunatilaka, Fahad Zafar, Vineetha Kalavally, and Rajendran Parthiban. Led based indoor visible light communications: State of the art. *IEEE Communications Surveys & Tutorials*, 17(3):1649–1678, 2015. (Cited on page 10.)

[25] Ton Koonen, Ketemaw Mekonnen, Zizheng Cao, Frans Huijskens, Ngoc Quan Pham, and Eduward Tangdiongga. Ultra-high-capacity wireless communication by means of steered narrow optical beams. *Philosophical Transactions of the Royal Society A*, 378(2169):20190192, 2020. (Cited on pages 10, 12, 53, and 54.)

[26] Hyunchae Chun, Sujan Rajbhandari, Grahame Faulkner, Dobroslav Tsonev, Enyuan Xie, Jonathan James Donald McKendry, Erdan Gu, Martin D Dawson, Dominic C O'Brien, and Harald Haas. Led based wavelength division multiplexed 10 gb/s visible light communications. *Journal of lightwave technology*, 34(13):3047–3052, 2016. (Cited on pages 10 and 54.)

[27] Harald Haas, Liang Yin, Yunlu Wang, and Cheng Chen. What is lifi? *Journal of lightwave technology*, 34(6):1533–1544, 2015. (Cited on pages 10 and 54.)

[28] Ariel Gomez, Kai Shi, Crisanto Quintana, Robert Maher, Grahame Faulkner, Polina Bayvel, Benn C Thomsen, and Dominic O'Brien. Design and demonstration of a 400 gb/s indoor optical wireless communications link. *Journal of Lightwave Technology*, 34(22):5332–5339, 2016. (Cited on pages 10 and 54.)

[29] Zizheng Cao, Longfei Shen, Yuqing Jiao, Xinran Zhao, and Ton Koonen. 200 gbps ook transmission over an indoor optical wireless link enabled by an integrated cascaded aperture optical receiver. In *2017 Optical Fiber Communications Conference and Exhibition (OFC)*, pages 1–3. IEEE, 2017. (Cited on page 10.)

[30] Fausto Gomez-Agis, Sjoerd P van de Heide, Chigo M Okonkwo, Eduward Tangdiongga, and AMJ Koonen. 112 gbit/s transmission in a 2d beam steering awg-based optical wireless communication system. In *2017 European Conference on Optical Communication (ECOC)*, pages 1–3. IEEE, 2017. (Cited on page 10.)

[31] Ariel Gomez, Kai Shi, Crisanto Quintana, Masaki Sato, Grahame Faulkner, Benn C Thomsen, and Dominic O'Brien. Beyond 100-gb/s indoor wide field-of-view optical wireless communications. *IEEE Photonics Technology Letters*, 27(4):367–370, 2014. (Cited on pages 10 and 54.)

[32] David Muirhead, Muhammad Ali Imran, and Kamran Arshad. A survey of the challenges, opportunities and use of multiple antennas in current and future 5g small cell base stations. *IEEE access*, 4:2952–2964, 2016. (Cited on page 11.)

[33] N Serafimovski, R Lacroix, M Perrufel, S Leroux, S Clement, N Kundu, D Chiaroni, G Patwardhan, A Myles, C Jurczak, et al. Light communications for wireless local area networking. *IEEE 5G Tech Focus*, 2, 2018. (Cited on page 11.)

[34] AMJ Koonen and E Tangdiongga. Photonic home area networks. *Journal of Lightwave Technology*, 32(4):591–604, 2013. (Cited on page 12.)

[35] Zizheng Cao, Xuebing Zhang, Gerwin Osnabrugge, Juhao Li, Ivo M Vellekoop, and Antonius MJ Koonen. Reconfigurable beam system for non-line-of-sight free-space optical communication. *Light: Science & Applications*, 8(1):1–9, 2019. (Cited on pages 12, 53, and 54.)

[36] Ton Koonen, Fausto Gomez-Agis, Jiun-Yu Sung, Zizheng Cao, Ketemaw Mekonnen, Frans Huijskens, and Eduward Tangdiongga. Indoor optical/radio wireless communication-demonstration of high-def video streaming using steerable infrared beams. In *2018 International Topical Meeting on Microwave Photonics (MWP)*, pages 1–4. IEEE, 2018. (Cited on page 12.)

[37] AMJ Koonen and M García Larrodé. Radio-over-mmf techniques—part ii: Microwave to millimeter-wave systems. *Journal of lightwave technology*, 26(15):2396–2408, 2008. (Cited on page 12.)

[38] Ton Koonen, Ketemaw Addis Mekonnen, Frans Huijskens, Ngoc-Quan Pham, Zizheng Cao, and Eduward Tangdiongga. Fully passive user localization for beam-steered high-capacity optical wireless communication system. *Journal of Lightwave Technology*, 38(10):2842–2848, 2020. (Cited on pages 12 and 15.)

[39] Yan Shi, Eduward Tangdiongga, AMJ Koonen, Andreas Bluschke, Philipp Rietzsch, Julio Montalvo, Maurice M de Laat, Gerlas N Van Den Hoven, and Bas Huiszoon. Plastic-optical-fiber-based in-home optical networks. *IEEE Communications Magazine*, 52(6):186–193, 2014. (Cited on page 12.)

[40] Christina Lim, Yu Tian, Chathurika Ranaweera, Thas Ampalavanapillai Nirmalathas, Elaine Wong, and Ka-Lun Lee. Evolution of radio-over-fiber technology. *Journal of Lightwave Technology*, 37(6):1647–1656, 2019. (Cited on pages 13 and 21.)

[41] Tara Fortier and Esther Baumann. 20 years of developments in optical frequency comb technology and applications. *Communications Physics*, 2(1):1–16, 2019. (Cited on pages 13 and 14.)

[42] Lars Lundberg, Mikael Mazur, Ali Mirani, Benjamin Foo, Jochen Schröder, Victor Torres-Company, Magnus Karlsson, and Peter A Andrekson. Phase-coherent lightwave communications with frequency combs. *Nature communications*, 11(1):1–7, 2020. (Cited on pages 15, 21, and 22.)

[43] Zizheng Cao, Xinran Zhao, FM Soares, N Tessema, and AMJ Koonen. 38-ghz millimeter wave beam steered fiber wireless systems for 5g indoor coverage: architectures, devices, and links. *IEEE journal of quantum electronics*, 53(1):1–9, 2016. (Cited on page 15.)

[44] Ton Koonen, Ketemaw Mekonnen, Zizheng Cao, Frans Huijskens, Ngoc-Quan Pham, and Eduward Tangdiongga. Optically controlled beam-steering wireless systems. In *Optical Fiber Communication Conference*, pages M1J–1. Optical Society of America, 2020. (Cited on page 15.)

[45] Alison M Yao and Miles J Padgett. Orbital angular momentum: origins, behavior and applications. *Advances in optics and photonics*, 3(2):161–204, 2011. (Cited on page 16.)

[46] Les Allen, Marco W Beijersbergen, RJC Spreeuw, and JP Woerdman. Orbital angular momentum of light and the transformation of laguerre-gaussian laser modes. *Physical review A*, 45(11):8185, 1992. (Cited on page 16.)

[47] Guillermo Federico Quinteiro, DE Reiter, and T Kuhn. Formulation of the twisted-light–matter interaction at the phase singularity: The twisted-light gauge. *Physical Review A*, 91(3):033808, 2015. (Cited on page 16.)

[48] Jian Wang. Advances in communications using optical vortices. *Photonics Research*, 4(5):B14–B28, 2016. (Cited on pages 16 and 80.)

[49] Alan E Willner, Hao Huang, Yan Yan, Yongxiong Ren, Nisar Ahmed, Goudong Xie, Changjing Bao, L Li, Y Cao, Z Zhao, et al. Optical communications using orbital angular momentum beams. *Advances in optics and photonics*, 7(1):66–106, 2015. (Cited on pages 16 and 80.)

[50] Fabrizio Tamburini, Elettra Mari, Anna Sponselli, Bo Thidé, Antonio Bianchini, and Filippo Romanato. Encoding many channels on the same frequency through radio vorticity: first experimental test. *New Journal of Physics*, 14(3):033001, 2012. (Cited on pages 16 and 36.)

[51] Ting Lei, Meng Zhang, Yuru Li, Ping Jia, Gordon Ning Liu, Xiaogeng Xu, Zhaohui Li, Changjun Min, Jiao Lin, Changyuan Yu, et al. Massive individual orbital angular momentum channels for multiplexing enabled by dammann gratings. *Light: Science & Applications*, 4(3):e257–e257, 2015. (Cited on pages 16, 80, 81, and 83.)

[52] Heyun Tan, Junhong Deng, Ruizhe Zhao, Xiong Wu, Guixin Li, Lingling Huang, Jie Liu, and Xinlun Cai. A free-space orbital angular momentum multiplexing communication system based on a metasurface. *Laser & Photonics Reviews*, 13(6):1800278, 2019. (Cited on pages 16, 56, and 81.)

[53] Wenchi Cheng, Hailin Zhang, Liping Liang, Haiyue Jing, and Zan Li. Orbital-angular-momentum embedded massive mimo: Achieving multiplicative spectrum-efficiency for mmwave communications. *IEEE Access*, 6:2732–2745, 2017. (Cited on page 16.)

[54] Yifei Yuan, Yajun Zhao, Baiqing Zong, and Sergio Parolari. Potential key technologies for 6g mobile communications. *Science China Information Sciences*, 63:1–19, 2020. (Cited on page 16.)

[55] Anutusha Dogra, Rakesh Kumar Jha, and Shubha Jain. A survey on beyond 5g network with the advent of 6g: Architecture and emerging technologies. *IEEE Access*, 9:67512–67547, 2020. (Cited on page 16.)

[56] Wenchi Cheng, Wei Zhang, Haiyue Jing, Shanghua Gao, and Hailin Zhang. Orbital angular momentum for wireless communications. *IEEE Wireless Communications*, 26(1):100–107, 2018. (Cited on page 16.)

[57] wikipedia. 5G NR frequency bands. `https://en.wikipedia.org/wiki/5G_NR_frequency_bands`, 2021. (Cited on page 22.)

[58] Nathalie Picqué and Theodor W Hänsch. Frequency comb spectroscopy. *Nature Photonics*, 13(3):146–157, 2019. (Cited on page 22.)

[59] Pablo Marin-Palomo, Juned N Kemal, Maxim Karpov, Arne Kordts, Joerg Pfeifle, Martin HP Pfeiffer, Philipp Trocha, Stefan Wolf, Victor Brasch, Miles H Anderson, et al. Microresonator-based solitons for massively parallel coherent optical communications. *Nature*, 546(7657):274–279, 2017. (Cited on page 22.)

[60] BJ Bloom, TL Nicholson, JR Williams, SL Campbell, M Bishof, X Zhang, W Zhang, SL Bromley, and J Ye. An optical lattice clock with accuracy and stability at the 10- 18 level. *Nature*, 506(7486):71–75, 2014. (Cited on page 22.)

[61] Andrew J Metcalf, Hyoung-Jun Kim, Daniel E Leaird, Jose A Jaramillo-Villegas, Keith A McKinzie, Vikrant Lal, Amir Hosseini, Gloria E Hoefler, Fred Kish, and Andrew M Weiner. Integrated line-by-line optical pulse shaper for high-fidelity and rapidly reconfigurable rf-filtering. *Optics Express*, 24(21):23925–23940, 2016. (Cited on page 22.)

[62] Callum Deakin and Zhixin Liu. Dual frequency comb assisted analog-to-digital conversion. *Optics Letters*, 45(1):173–176, 2020. (Cited on page 22.)

[63] Zhechao Wang, Kasper Van Gasse, Valentina Moskalenko, Sylwester Latkowski, Erwin Bente, Bart Kuyken, and Gunther Roelkens. A iii-v-on-si ultra-dense comb laser. *Light: Science & Applications*, 6(5):e16260–e16260, 2017. (Cited on page 22.)

[64] GKM Hasanuzzaman, Atsushi Kanno, Pham Tien Dat, and Stavros Iezekiel. W-band radio-over-fiber link based on self-oscillating optical frequency comb generator. In *Optical Fiber Communication Conference*, pages W1F–6. Optical Society of America, 2018. (Cited on page 22.)

[65] GKM Hasanuzzaman, Haymen Shams, Cyril C Renaud, John Mitchell, Alwyn J Seeds, and Stavros Iezekiel. Tunable thz signal generation and radio-over-fiber link based on an optoelectronic oscillator-driven optical frequency comb. *Journal of Lightwave Technology*, 38(19):5240–5247, 2019. (Cited on page 22.)

[66] GKM Hasanuzzaman, Atsushi Kanno, Pham Tien Dat, and Stavros Iezekiel. Self-oscillating optical frequency comb: Application to low phase noise millimeter wave generation and radio-over-fiber link. *Journal of Lightwave Technology*, 36(19):4535–4542, 2018. (Cited on page 22.)

[67] Zhixin Liu, Selina Farwell, Mike Wale, David J Richardson, and Radan Slavík. Inp-based optical comb-locked tunable transmitter. In *Optical Fiber Communication Conference*, pages Tu2K–2. Optical Society of America, 2016. (Cited on pages 23 and 31.)

[68] E Gehrig and O Hess. Dynamic amplitude-phase coupling in quantum-dot lasers. *Applied Physics Letters*, 86(20):203116, 2005. (Cited on page 23.)

[69] Dietmar W Reschner, Edeltraud Gehrig, and Ortwin Hess. Pulse amplification and spatio-spectral hole-burning in inhomogeneously broadened quantum-dot semiconductor optical amplifiers. *IEEE journal of quantum electronics*, 45(1):21–33, 2008. (Cited on page 23.)

[70] Ortwin Hess and Edeltraud Gehrig. *Photonics of quantum-dot nanomaterials and devices: theory and modelling*. World Scientific, 2011. (Cited on page 23.)

[71] Edik U Rafailov, Maria Ana Cataluna, and Wilson Sibbett. Mode-locked quantum-dot lasers. *Nature photonics*, 1(7):395–401, 2007. (Cited on page 23.)

[72] Mark G Thompson, Alastair R Rae, Mo Xia, Richard V Penty, and Ian H White. Ingaas quantum-dot mode-locked laser diodes. *IEEE Journal of Selected Topics in Quantum Electronics*, 15(3):661–672, 2009. (Cited on pages 23, 27, and 28.)

[73] Guillermo Carpintero, Mark G Thompson, Richard V Penty, and Ian H White. Low noise performance of passively mode-locked 10-ghz quantum-dot laser diode. *IEEE Photonics Technology Letters*, 21(6):389–391, 2009. (Cited on page 23.)

[74] Siming Chen, Wei Li, Jiang Wu, Qi Jiang, Mingchu Tang, Samuel Shutts, Stella N Elliott, Angela Sobiesierski, Alwyn J Seeds, Ian Ross, et al. Electrically pumped continuous-wave iii–v quantum dot lasers on silicon. *Nature Photonics*, 10(5):307–311, 2016. (Cited on pages 23 and 25.)

[75] Mengya Liao, Siming Chen, Zhixin Liu, Yi Wang, Lalitha Ponnampalam, Zichuan Zhou, Jiang Wu, Mingchu Tang, Samuel Shutts, Zizhuo Liu, et al. Low-noise 1.3 μm inas/gaas quantum dot laser monolithically grown on silicon. *Photonics Research*, 6(11):1062–1066, 2018. (Cited on page 23.)

[76] Taojie Zhou, Mingchu Tang, Guohong Xiang, Boyuan Xiang, Suikong Hark, Mickael Martin, Thierry Baron, Shujie Pan, Jae-Seong Park, Zizhuo Liu, et al. Continuous-wave quantum dot photonic crystal lasers grown on on-axis si (001). *Nature communications*, 11(1):1–7, 2020. (Cited on page 23.)

[77] Zizhuo Liu, Constanze Hantschmann, Mingchu Tang, Ying Lu, Jae-Seong Park, Mengya Liao, Shujie Pan, Ana Sanchez, Richard Beanland, Mickael Martin, et al. Origin of defect tolerance in inas/gaas quantum dot lasers grown on silicon. *Journal of Lightwave Technology*, 38(2):240–248, 2019. (Cited on page 23.)

[78] Fabien Kéfélian, Shane O'Donoghue, Maria Teresa Todaro, John G McInerney, and Guillaume Huyet. Rf linewidth in monolithic passively mode-locked semiconductor laser. *IEEE Photonics Technology Letters*, 20(16):1405–1407, 2008. (Cited on page 23.)

[79] Edik U Rafailov, Maria Ana Cataluna, Wilson Sibbett, ND Il'Inskaya, Yu M Zadiranov, AE Zhukov, VM Ustinov, Daniil A Livshits, AR Kovsh, and

NN Ledentsov. High-power picosecond and femtosecond pulse generation from a two-section mode-locked quantum-dot laser. *Applied Physics Letters*, 87(8):081107, 2005. (Cited on page 23.)

[80] MG Thompson, A Rae, RL Sellin, C Marinelli, RV Penty, IH White, AR Kovsh, SS Mikhrin, DA Livshits, and IL Krestnikov. Subpicosecond high-power mode locking using flared waveguide monolithic quantum-dot lasers. *Applied Physics Letters*, 88(13):133119, 2006. (Cited on page 23.)

[81] Maria Teresa Todaro, Jean-Philippe Tourrenc, Stephen P Hegarty, Carmel Kelleher, Brian Corbett, Guillaume Huyet, and John G McInerney. Simultaneous achievement of narrow pulse width and low pulse-to-pulse timing jitter in 1.3 μm passively mode-locked quantum-dot lasers. *Optics letters*, 31(21):3107–3109, 2006. (Cited on page 23.)

[82] Songtao Liu, Justin C Norman, Daehwan Jung, MJ Kennedy, Arthur C Gossard, and John E Bowers. Monolithic 9 ghz passively mode locked quantum dot lasers directly grown on on-axis (001) si. *Applied Physics Letters*, 113(4):041108, 2018. (Cited on page 23.)

[83] Dominik Auth, Songtao Liu, Justin Norman, John Edward Bowers, and Stefan Breuer. Passively mode-locked semiconductor quantum dot on silicon laser with 400 hz rf line width. *Optics express*, 27(19):27256–27266, 2019. (Cited on page 23.)

[84] Songtao Liu, Xinru Wu, Daehwan Jung, Justin C Norman, MJ Kennedy, Hon K Tsang, Arthur C Gossard, and John E Bowers. High-channel-count 20 ghz passively mode-locked quantum dot laser directly grown on si with 4.1 tbit/s transmission capacity. *Optica*, 6(2):128–134, 2019. (Cited on pages 23 and 33.)

[85] Guocheng Liu, Zhenguo Lu, Jiaren Liu, Youxin Mao, Martin Vachon, Chunying Song, Pedro Barrios, and Philip J Poole. Passively mode-locked quantum dash laser with an aggregate 5.376 tbit/s pam-4 transmission capacity. *Optics express*, 28(4):4587–4593, 2020. (Cited on pages 23 and 33.)

[86] Vidak Vujicic, Cosimo Calo, Regan Watts, Francois Lelarge, Colm Browning, Kamel Merghem, Anthony Martinez, Abderrahim Ramdane, and

Liam P Barry. Quantum dash mode-locked lasers for data centre applications. *IEEE Journal of selected topics in quantum electronics*, 21(6):53–60, 2015. (Cited on page 23.)

[87] Juned N Kemal, Pablo Marin-Palomo, Vivek Panapakkam, Philipp Trocha, Stefan Wolf, Kamel Merghem, François Lelarge, Abderrahim Ramdane, Sebastian Randel, Wolfgang Freude, et al. Coherent wdm transmission using quantum-dash mode-locked laser diodes as multi-wavelength source and local oscillator. *Optics express*, 27(22):31164–31175, 2019. (Cited on page 23.)

[88] ZG Lu, JR Liu, CY Song, J Weber, Y Mao, SD Chang, HP Ding, PJ Poole, PJ Barrios, D Poitras, et al. High performance inas/inp quantum dot 34.462-ghz c-band coherent comb laser module. *Optics express*, 26(2):2160–2167, 2018. (Cited on page 23.)

[89] Y Arakawa and Hiroyuki Sakaki. Multidimensional quantum well laser and temperature dependence of its threshold current. *Applied physics letters*, 40(11):939–941, 1982. (Cited on page 23.)

[90] Kenichi Nishi, Keizo Takemasa, Mitsuru Sugawara, and Yasuhiko Arakawa. Development of quantum dot lasers for data-com and silicon photonics applications. *IEEE Journal of Selected Topics in Quantum Electronics*, 23(6):1–7, 2017. (Cited on pages 23 and 25.)

[91] Maria Ana Cataluna, Edik U Rafailov, AD McRobbie, Wilson Sibbett, Daniil A Livshits, and AR Kovsh. Stable mode-locked operation up to 80/spl deg/c from an ingaas quantum-dot laser. *IEEE photonics technology letters*, 18(14):1500–1502, 2006. (Cited on page 23.)

[92] JK Mee, MT Crowley, N Patel, D Murrell, R Raghunathan, A Aboketaf, A Elshaari, SF Preble, P Ampadu, and LF Lester. A passively mode-locked quantum-dot laser operating over a broad temperature range. *Applied Physics Letters*, 101(7):071112, 2012. (Cited on page 23.)

[93] M Laemmlin, G Fiol, C Meuer, M Kuntz, F Hopfer, AR Kovsh, NN Ledentsov, and D Bimberg. Distortion-free optical amplification of 20-80 ghz modelocked laser pulses at 1.3 μm using quantum dots. *Electronics Letters*, 42(12):697–699, 2006. (Cited on page 23.)

[94] K Nishi, T Kageyama, M Yamaguchi, Y Maeda, K Takemasa, T Yamamoto, M Sugawara, and Y Arakawa. Molecular beam epitaxial growths of high-optical-gain inas quantum dots on gaas for long-wavelength emission. *Journal of crystal growth*, 378:459–462, 2013. (Cited on page 25.)

[95] KA Williams, MG Thompson, and IH White. Long-wavelength monolithic mode-locked diode lasers. *New Journal of Physics*, 6(1):179, 2004. (Cited on page 27.)

[96] J O'Gorman, AFJ Levi, T Tanbun-Ek, and RA Logan. Saturable absorption in intracavity loss modulated quantum well lasers. *Applied physics letters*, 59(1):16–18, 1991. (Cited on page 29.)

[97] Jesse K Mee, Mark Thomas Crowley, David Murrell, Ravi Raghunathan, and Luke F Lester. Temperature performance of monolithic passively mode-locked quantum dot lasers: experiments and analytical modeling. *IEEE Journal of Selected Topics in Quantum Electronics*, 19(4):1101110–1101110, 2013. (Cited on page 30.)

[98] F Klopf, S Deubert, JP Reithmaier, and A Forchel. Correlation between the gain profile and the temperature-induced shift in wavelength of quantum-dot lasers. *Applied Physics Letters*, 81(2):217–219, 2002. (Cited on page 31.)

[99] LH Li, M Rossetti, A Fiore, L Occhi, and C Velez. Wide emission spectrum from superluminescent diodes with chirped quantum dot multilayers. *Electronics letters*, 41(1):41–43, 2005. (Cited on page 32.)

[100] KJ Zhou, Q Jiang, ZY Zhang, SM Chen, HY Liu, ZH Lu, K Kennedy, SJ Matcher, and RA Hogg. Quantum dot selective area intermixing for broadband light sources. *Optics Express*, 20(24):26950–26957, 2012. (Cited on page 32.)

[101] Siming Chen, Wei Li, Ziyang Zhang, David Childs, Kejia Zhou, Jonathan Orchard, Ken Kennedy, Maxime Hugues, Edmund Clarke, Ian Ross, et al. Gaas-based superluminescent light-emitting diodes with 290-nm emission bandwidth by using hybrid quantum well/quantum dot structures. *Nanoscale research letters*, 10(1):1–8, 2015. (Cited on page 32.)

[102] Jian Wang, Jeng-Yuan Yang, Irfan M Fazal, Nisar Ahmed, Yan Yan, Hao Huang, Yongxiong Ren, Yang Yue, Samuel Dolinar, Moshe Tur, et al. Terabit free-space data transmission employing orbital angular momentum

multiplexing. *Nature photonics*, 6(7):488–496, 2012. (Cited on pages 36 and 80.)

[103] Alan E Willner, Yongxiong Ren, Guodong Xie, Yan Yan, Long Li, Zhe Zhao, Jian Wang, Moshe Tur, Andreas F Molisch, and Solyman Ashrafi. Recent advances in high-capacity free-space optical and radio-frequency communications using orbital angular momentum multiplexing. *Philosophical Transactions of the Royal Society A: Mathematical, Physical and Engineering Sciences*, 375(2087):20150439, 2017. (Cited on page 36.)

[104] Xinlu Gao, Shanguo Huang, Yongfeng Wei, Wensheng Zhai, Wenjing Xu, Shan Yin, Jing Zhou, and Wanyi Gu. An orbital angular momentum radio communication system optimized by intensity controlled masks effectively: Theoretical design and experimental verification. *Applied Physics Letters*, 105(24):241109, 2014. (Cited on page 36.)

[105] GA Turnbull, DA Robertson, GM Smith, L Allen, and MJ Padgett. The generation of free-space laguerre-gaussian modes at millimetre-wave frequencies by use of a spiral phaseplate. *Optics communications*, 127(4-6):183–188, 1996. (Cited on page 36.)

[106] Siavoush Mohaghegh Mohammadi, Lars KS Daldorff, Jan ES Bergman, Roger L Karlsson, Bo Thidé, Kamyar Forozesh, Tobia D Carozzi, and Brett Isham. Orbital angular momentum in radio—a system study. *IEEE transactions on Antennas and Propagation*, 58(2):565–572, 2009. (Cited on page 36.)

[107] Zizheng Cao, F Li, ACF Reniers, CW Oh, HPA van den Boom, E Tangdiongga, and AMJ Koonen. Spatial filtering in a broadband in-home ofdm radio-over-fiber network. *IEEE Photonics Technology Letters*, 26(6):575–578, 2014. (Cited on page 36.)

[108] Xinlu Gao, Shanguo Huang, Jing Zhou, Yongfeng Wei, Chao Gao, Xukai Zhang, and Wanyi Gu. Generating, multiplexing/demultiplexing and receiving the orbital angular momentum of radio frequency signals using an optical true time delay unit. *Journal of Optics*, 15(10):105401, 2013. (Cited on page 36.)

[109] Xinlu Gao, Shanguo Huang, Yunlong Song, Shangyuan Li, Yongfeng Wei, Jing Zhou, Xiaoping Zheng, Hanyi Zhang, and Wanyi Gu. Generating

the orbital angular momentum of radio frequency signals using optical-true-time-delay unit based on optical spectrum processor. *Optics letters*, 39(9):2652–2655, 2014. (Cited on page 36.)

[110] Xinlu Gao, Mingyang Zhao, Mutong Xie, Mingzheng Lei, Xiyao Song, Ke Bi, Zhennan Zheng, and Shanguo Huang. 2d optically controlled radio frequency orbital angular momentum beam steering system based on a dual-parallel mach–zehnder modulator. *Optics letters*, 44(2):255–258, 2019. (Cited on page 37.)

[111] Mutong Xie, Mingyang Zhao, Mingzheng Lei, Yongle Wu, Yuanan Liu, Xinlu Gao, and Shanguo Huang. Anti-dispersion phase-tunable microwave mixer based on a dual-drive dual-parallel mach-zehnder modulator. *Optics express*, 26(1):454–462, 2018. (Cited on page 37.)

[112] Yamei Zhang and Shilong Pan. Broadband microwave signal processing enabled by polarization-based photonic microwave phase shifters. *IEEE Journal of Quantum Electronics*, 54(4):1–12, 2018. (Cited on page 37.)

[113] Yamei Zhang and Shilong Pan. Frequency-multiplying microwave photonic phase shifter for independent multichannel phase shifting. *Optics letters*, 41(6):1261–1264, 2016. (Cited on page 37.)

[114] Shilong Pan and Yamei Zhang. Tunable and wideband microwave photonic phase shifter based on a single-sideband polarization modulator and a polarizer. *Optics Letters*, 37(21):4483–4485, 2012. (Cited on page 37.)

[115] Xudong Wang, Tong Niu, Erwin Hoi Wing Chan, Xinhuan Feng, Bai-ou Guan, and Jianping Yao. Photonics-based wideband microwave phase shifter. *IEEE Photonics Journal*, 9(3):1–10, 2017. (Cited on page 37.)

[116] Z Cao, Q Wang, N Tessema, X Parareda, HPA van den Boom, E Tangdiongga, and AMJ Koonen. Electrically-controlled optical phase shifter for broadband radio orbital angular momentum mode generation. In *2014 The European Conference on Optical Communication (ECOC)*, pages 1–3. IEEE, 2014. (Cited on page 37.)

[117] Ignacio Moreno, Jeffrey A Davis, Don M Cottrell, N Zhang, and X-C Yuan. Encoding generalized phase functions on dammann gratings. *Optics letters*, 35(10):1536–1538, 2010. (Cited on page 37.)

[118] Meint Smit, Xaveer Leijtens, EAJM Bente, JJGM Van der Tol, HPMM Ambrosius, David Robbins, Mike Wale, Norbert Grote, and Martin Schell. Generic foundry model for inp-based photonics. *IET optoelectronics*, 5(5):187–194, 2011. (Cited on page 38.)

[119] Z Cao, N Tessema, S Latkowski, X Zhao, Z Chen, V Moskalenko, KA Williams, HPA Van Der Boom, E Tangdiongga, and AMJ Koonen. Integrated remotely tunable optical delay line for millimeter-wave beam steering fabricated in an inp generic foundry. *Optics letters*, 40(17):3930–3933, 2015. (Cited on page 41.)

[120] Joseph W Goodman. Introduction to fourier optics. 3rd. *Roberts and Company Publishers*, 2005. (Cited on page 43.)

[121] Torner Lluis, JP Torres, and S Carrasco. Digital spiral imaging. *Opt. Express*, 13:873–881, 2005. (Cited on page 47.)

[122] NCAT. Growth In The Internet of Things. `https://www.ncta.com/chart/growth-in-the-internet-of-things`, 2021. (Cited on page 53.)

[123] Cisco. 802.11ac: The fifth generation of wi-fi. 2018. (Cited on page 53.)

[124] A Gomez, Crisanto Quintana, Grahame Faulkner, and Dominic O'Brien. Point-to-multipoint holographic beamsteering techniques for indoor optical wireless communications. In *Broadband Access Communication Technologies X*, volume 9772, page 97720Q. International Society for Optics and Photonics, 2016. (Cited on page 54.)

[125] Ke Wang, Ampalavanapillai Nirmalathas, Christina Lim, Kamal Alameh, and Efstratios Skafidas. Full-duplex gigabit indoor optical wireless communication system with cap modulation. *IEEE Photonics Technology Letters*, 28(7):790–793, 2016. (Cited on page 54.)

[126] Ton Koonen, Joanne Oh, Ketemaw Mekonnen, Zizheng Cao, and Eduward Tangdiongga. Ultra-high capacity indoor optical wireless communication using 2d-steered pencil beams. *Journal of Lightwave Technology*, 34(20):4802–4809, 2016. (Cited on page 55.)

[127] Trevor Chan, Evgeny Myslivets, and Joseph E Ford. 2-dimensional beamsteering using dispersive deflectors and wavelength tuning. *Optics Express*, 16(19):14617–14628, 2008. (Cited on page 55.)

[128] Ke Wang, Zeshi Yuan, Elaine Wong, Kamal Alameh, Hongtao Li, Kandeepan Sithamparanathan, and Efstratios Skafidas. Experimental demonstration of indoor infrared optical wireless communications with a silicon photonic integrated circuit. *Journal of Lightwave Technology*, 37(2):619–626, 2018. (Cited on page 55.)

[129] Karel Van Acoleyen, Wim Bogaerts, and Roel Baets. Two-dimensional dispersive off-chip beam scanner fabricated on silicon-on-insulator. *IEEE photonics technology letters*, 23(17):1270–1272, 2011. (Cited on page 55.)

[130] T. Koonen, A. Khalid, J. Oh, F. Gomez-Agis, and E. Tangdiongga. High-capacity optical wireless communication using 2-dimensional ir beam steering. In *2017 Opto-Electronics and Communications Conference (OECC) and Photonics Global Conference (PGC)*, pages 1–4, 2017. (Cited on pages 55, 56, 59, and 61.)

[131] Ton Koonen, Fausto Gomez-Agis, Frans Huijskens, Ketemaw Addis Mekonnen, Zizheng Cao, and Eduward Tangdiongga. High-capacity optical wireless communication using two-dimensional ir beam steering. *Journal of Lightwave Technology*, 36(19):4486–4493, 2018. (Cited on pages 55, 56, 58, 73, 74, and 102.)

[132] Nanfang Yu and Federico Capasso. Flat optics with designer metasurfaces. *Nature materials*, 13(2):139–150, 2014. (Cited on page 55.)

[133] Arash Nemati, Qian Wang, Minghui Hong, and Jinghua Teng. Tunable and reconfigurable metasurfaces and metadevices. *Opto-Electronic Advances*, 1(5):180009, 2018. (Cited on page 55.)

[134] Hou-Tong Chen, Antoinette J Taylor, and Nanfang Yu. A review of metasurfaces: physics and applications. *Reports on progress in physics*, 79(7):076401, 2016. (Cited on page 55.)

[135] Amr M Shaltout, Vladimir M Shalaev, and Mark L Brongersma. Spatiotemporal light control with active metasurfaces. *Science*, 364(6441), 2019. (Cited on page 55.)

[136] Cheng Hung Chu, Ming Lun Tseng, Jie Chen, Pin Chieh Wu, Yi-Hao Chen, Hsiang-Chu Wang, Ting-Yu Chen, Wen Ting Hsieh, Hui Jun Wu, Greg Sun, et al. Active dielectric metasurface based on phase-change medium.

Laser & Photonics Reviews, 10(6):986–994, 2016. (Cited on pages 55 and 107.)

[137] Pin Chieh Wu, Ragip A Pala, Ghazaleh Kafaie Shirmanesh, Wen-Hui Cheng, Ruzan Sokhoyan, Meir Grajower, Muhammad Z Alam, Duhyun Lee, and Harry A Atwater. Dynamic beam steering with all-dielectric electro-optic iii–v multiple-quantum-well metasurfaces. *Nature communications*, 10(1):1–9, 2019. (Cited on pages 55, 106, and 107.)

[138] Mohammed Reza M Hashemi, Shang-Hua Yang, Tongyu Wang, Nelson Sepúlveda, and Mona Jarrahi. Electronically-controlled beam-steering through vanadium dioxide metasurfaces. *Scientific reports*, 6:35439, 2016. (Cited on pages 55 and 107.)

[139] Qian Ma, Guo Dong Bai, Hong Bo Jing, Cheng Yang, Lianlin Li, and Tie Jun Cui. Smart metasurface with self-adaptively reprogrammable functions. *Light: Science & Applications*, 8(1):1–12, 2019. (Cited on page 55.)

[140] Fei Ding, Rucha Deshpande, and Sergey I Bozhevolnyi. Bifunctional gap-plasmon metasurfaces for visible light: polarization-controlled unidirectional surface plasmon excitation and beam steering at normal incidence. *Light: Science & Applications*, 7(4):17178–17178, 2018. (Cited on pages 55 and 56.)

[141] Fei Ding, Yuanqing Yang, Rucha A Deshpande, and Sergey I Bozhevolnyi. A review of gap-surface plasmon metasurfaces: fundamentals and applications. *Nanophotonics*, 7(6):1129–1156, 2018. (Cited on page 56.)

[142] Shulin Sun, Kuang-Yu Yang, Chih-Ming Wang, Ta-Ko Juan, Wei Ting Chen, Chun Yen Liao, Qiong He, Shiyi Xiao, Wen-Ting Kung, Guang-Yu Guo, et al. High-efficiency broadband anomalous reflection by gradient meta-surfaces. *Nano letters*, 12(12):6223–6229, 2012. (Cited on page 56.)

[143] Anders Pors, Michael G Nielsen, René Lynge Eriksen, and Sergey I Bozhevolnyi. Broadband focusing flat mirrors based on plasmonic gradient metasurfaces. *Nano letters*, 13(2):829–834, 2013. (Cited on page 56.)

[144] Yonghwi Kim, Pin Chieh Wu, Ruzan Sokhoyan, Kelly Mauser, Rebecca Glaudell, Ghazaleh Kafaie Shirmanesh, and Harry A Atwater. Phase modulation with electrically tunable vanadium dioxide phase-change metasurfaces. *Nano letters*, 19(6):3961–3968, 2019. (Cited on page 56.)

[145] Yuval Yifat, Michal Eitan, Zeev Iluz, Yael Hanein, Amir Boag, and Jacob Scheuer. Highly efficient and broadband wide-angle holography using patch-dipole nanoantenna reflectarrays. *Nano letters*, 14(5):2485–2490, 2014. (Cited on page 56.)

[146] Anders Pors, Ole Albrektsen, Ilya P Radko, and Sergey I Bozhevolnyi. Gap plasmon-based metasurfaces for total control of reflected light. *Scientific reports*, 3(1):1–6, 2013. (Cited on page 56.)

[147] Anders Pors, Michael G Nielsen, and Sergey I Bozhevolnyi. Plasmonic metagratings for simultaneous determination of stokes parameters. *Optica*, 2(8):716–723, 2015. (Cited on page 56.)

[148] Guowen Ding, Ke Chen, Xinyao Luo, Junming Zhao, Tian Jiang, and Yijun Feng. Dual-helicity decoupled coding metasurface for independent spin-to-orbital angular momentum conversion. *Physical Review Applied*, 11(4):044043, 2019. (Cited on page 56.)

[149] Shiwei Tang, Tong Cai, Guang-Ming Wang, Jian-Gang Liang, Xike Li, and Jiancheng Yu. High-efficiency dual-modes vortex beam generator with polarization-dependent transmission and reflection properties. *Scientific reports*, 8(1):1–10, 2018. (Cited on page 56.)

[150] Jesper Jung, Thomas Søndergaard, and Sergey I Bozhevolnyi. Gap plasmon-polariton nanoresonators: Scattering enhancement and launching of surface plasmon polaritons. *Physical Review B*, 79(3):035401, 2009. (Cited on page 62.)

[151] Nanfang Yu, Patrice Genevet, Mikhail A Kats, Francesco Aieta, Jean-Philippe Tetienne, Federico Capasso, and Zeno Gaburro. Light propagation with phase discontinuities: generalized laws of reflection and refraction. *science*, 334(6054):333–337, 2011. (Cited on pages 64 and 80.)

[152] Xiyue Zhang, Qi Li, Feifei Liu, Meng Qiu, Shulin Sun, Qiong He, and Lei Zhou. Controlling angular dispersions in optical metasurfaces. *Light: Science & Applications*, 9(1):1–12, 2020. (Cited on page 72.)

[153] Etienne Brasselet, Mangirdas Malinauskas, Albertas Žukauskas, and Saulius Juodkazis. Photopolymerized microscopic vortex beam generators: Precise delivery of optical orbital angular momentum. *Applied Physics Letters*, 97(21):211108, 2010. (Cited on page 80.)

[154] Xuewen Wang, Zhongquan Nie, Yao Liang, Jian Wang, Tao Li, and Baohua Jia. Recent advances on optical vortex generation. *Nanophotonics*, 7(9):1533–1556, 2018. (Cited on page 80.)

[155] Katie E Chong, Isabelle Staude, Anthony James, Jason Dominguez, Sheng Liu, Salvatore Campione, Ganapathi S Subramania, Ting S Luk, Manuel Decker, Dragomir N Neshev, et al. Polarization-independent silicon metadevices for efficient optical wavefront control. *Nano letters*, 15(8):5369–5374, 2015. (Cited on page 80.)

[156] Davit Hakobyan, Hernando Magallanes, Gediminas Seniutinas, Saulius Juodkazis, and Etienne Brasselet. Tailoring orbital angular momentum of light in the visible domain with metallic metasurfaces. *Advanced Optical Materials*, 4(2):306–312, 2016. (Cited on page 80.)

[157] Robert Charles Devlin, Antonio Ambrosio, Daniel Wintz, Stefano Luigi Oscurato, Alexander Yutong Zhu, Mohammadreza Khorasaninejad, Jaewon Oh, Pasqualino Maddalena, and Federico Capasso. Spin-to-orbital angular momentum conversion in dielectric metasurfaces. *Optics express*, 25(1):377–393, 2017. (Cited on page 80.)

[158] Xuewen Wang, Aleksandr A Kuchmizhak, Etienne Brasselet, and Saulius Juodkazis. Dielectric geometric phase optical elements fabricated by femtosecond direct laser writing in photoresists. *Applied Physics Letters*, 110(18):181101, 2017. (Cited on page 80.)

[159] Yuanmu Yang, Wenyi Wang, Parikshit Moitra, Ivan I Kravchenko, Dayrl P Briggs, and Jason Valentine. Dielectric meta-reflectarray for broadband linear polarization conversion and optical vortex generation. *Nano letters*, 14(3):1394–1399, 2014. (Cited on page 80.)

[160] Kun Huang, Hong Liu, Sara Restuccia, Muhammad Q Mehmood, Sheng-Tao Mei, Daniel Giovannini, Aaron Danner, Miles J Padgett, Jing-Hua Teng, and Cheng-Wei Qiu. Spiniform phase-encoded metagratings entangling arbitrary rational-order orbital angular momentum. *Light: Science & Applications*, 7(3):17156–17156, 2018. (Cited on page 80.)

[161] Alan Zhan, Shane Colburn, Rahul Trivedi, Taylor K Fryett, Christopher M Dodson, and Arka Majumdar. Low-contrast dielectric metasurface optics. *ACS Photonics*, 3(2):209–214, 2016. (Cited on page 80.)

[162] Changjun Min, Jinpeng Liu, Ting Lei, Guangyuan Si, Zhenwei Xie, Jiao Lin, Luping Du, and Xiaocong Yuan. Plasmonic nano-slits assisted polarization selective detour phase meta-hologram. *Laser & Photonics Reviews*, 10(6):978–985, 2016. (Cited on page 80.)

[163] Andrea Rubano, Filippo Cardano, Bruno Piccirillo, and Lorenzo Marrucci. Q-plate technology: a progress review. *JOSA B*, 36(5):D70–D87, 2019. (Cited on page 80.)

[164] Nenad Bozinovic, Yang Yue, Yongxiong Ren, Moshe Tur, Poul Kristensen, Hao Huang, Alan E Willner, and Siddharth Ramachandran. Terabit-scale orbital angular momentum mode division multiplexing in fibers. *science*, 340(6140):1545–1548, 2013. (Cited on page 80.)

[165] Hao Huang, Guodong Xie, Yan Yan, Nisar Ahmed, Yongxiong Ren, Yang Yue, Dvora Rogawski, Moshe J Willner, Baris I Erkmen, Kevin M Birnbaum, et al. 100 tbit/s free-space data link enabled by three-dimensional multiplexing of orbital angular momentum, polarization, and wavelength. *Optics letters*, 39(2):197–200, 2014. (Cited on pages 80 and 83.)

[166] N Zhang, XC Yuan, and RE Burge. Extending the detection range of optical vortices by dammann vortex gratings. *Optics letters*, 35(20):3495–3497, 2010. (Cited on pages 80, 81, and 83.)

[167] Zhongxi Wang, N Zhang, and X-C Yuan. High-volume optical vortex multiplexing and de-multiplexing for free-space optical communication. *Optics express*, 19(2):482–492, 2011. (Cited on page 80.)

[168] H Dammann and K Görtler. High-efficiency in-line multiple imaging by means of multiple phase holograms. *Optics communications*, 3(5):312–315, 1971. (Cited on pages 80 and 83.)

[169] H Dammann and E Klotz. Coherent optical generation and inspection of two-dimensional periodic structures. *Optica Acta: International Journal of Optics*, 24(4):505–515, 1977. (Cited on page 80.)

[170] Ignacio Moreno, Jeffrey A Davis, B Melvin L Pascoguin, Mark J Mitry, and Don M Cottrell. Vortex sensing diffraction gratings. *Optics letters*, 34(19):2927–2929, 2009. (Cited on page 81.)

[171] Changhe Zhou and Liren Liu. Numerical study of dammann array illuminators. *Applied optics*, 34(26):5961–5969, 1995. (Cited on pages 83 and 88.)

[172] Richard M Kerber, Jamie M Fitzgerald, Doris E Reiter, Sang Soon Oh, and Ortwin Hess. Reading the orbital angular momentum of light using plasmonic nanoantennas. *ACS Photonics*, 4(4):891–896, 2017. (Cited on page 95.)

[173] RM Kerber, JM Fitzgerald, SS Oh, DE Reiter, and O Hess. Orbital angular momentum dichroism in nanoantennas. *Communications Physics*, 1(1):1–7, 2018. (Cited on page 95.)

[174] Jianou Huang, Chao Li, Rongguo Lu, Lianyan Li, and Zizheng Cao. Beyond the 100 gbaud directly modulated laser for short reach applications. *Journal of Semiconductors*, 42(4):041306, 2021. (Cited on page 104.)

[175] I Vurgaftman, J R Meyer, and L R Ram-Mohan. Band parameters for iii–v compound semiconductors and their alloys. *Journal of applied physics*, 89(11):5815–5875, 2001. (Cited on page 104.)

[176] Takashi Tadokoro, Wataru Kobayashi, Takeshi Fujisawa, Takayuki Yamanaka, and Fumiyoshi Kano. 43 gb/s 1.3 μm dfb laser for 40 km transmission. *Journal of lightwave technology*, 30(15):2520–2524, 2012. (Cited on page 104.)

[177] Wataru Kobayashi, Toshio Ito, Takayuki Yamanaka, Takeshi Fujisawa, Yasuo Shibata, Takeshi Kurosaki, Masaki Kohtoku, Takashi Tadokoro, and Hiroaki Sanjoh. 50-gb/s direct modulation of a 1.3-μm ingaalas-based dfb laser with a ridge waveguide structure. *IEEE Journal of Selected Topics in Quantum Electronics*, 19(4):1500908–1500908, 2013. (Cited on page 104.)

[178] Manabu Matsuda, Ayahito Uetake, Takasi Simoyama, Shigekazu Okumura, Kazumasa Takabayashi, Mitsuru Ekawa, and Tsuyoshi Yamamoto. 1.3-μm-wavelength algainas multiple-quantum-well semi-insulating buried-heterostructure distributed-reflector laser arrays on semi-insulating inp substrate. *IEEE Journal of Selected Topics in Quantum Electronics*, 21(6):241–247, 2015. (Cited on page 104.)

[179] Shigeru Mieda, Nobuhide Yokota, Wataru Kobayashi, and Hiroshi Yasaka. Ultra-wide-bandwidth optically controlled dfb laser with external cavity. *IEEE Journal of Quantum Electronics*, 52(6):1–7, 2016. (Cited on page 104.)

[180] Yasuhiro Matsui, Richard Schatz, Thang Pham, William A Ling, Glen Carey, Henry M Daghighian, David Adams, Tsurugi Sudo, and Charles Roxlo. 55 ghz bandwidth distributed reflector laser. *Journal of lightwave technology*, 35(3):397–403, 2017. (Cited on page 104.)

[181] Gonghai Liu, Gongyuan Zhao, Junqiang Sun, Dingshan Gao, Qiaoyin Lu, and Weihua Guo. Experimental demonstration of dfb lasers with active distributed reflector. *Optics express*, 26(23):29784–29795, 2018. (Cited on page 104.)

[182] Suguru Yamaoka, Nikolaos-Panteleimon Diamantopoulos, Hidetaka Nishi, Ryo Nakao, Takuro Fujii, Koji Takeda, Tatsurou Hiraki, Takuma Tsurugaya, Shigeru Kanazawa, Hiromasa Tanobe, et al. Directly modulated membrane lasers with 108 ghz bandwidth on a high-thermal-conductivity silicon carbide substrate. *Nature Photonics*, pages 1–8, 2020. (Cited on page 104.)

[183] Di Che, Yasuhiro Matsui, Xi Chen, Richard Schatz, and Patrick Iannone. 400-gb/s direct modulation using a dfb+r laser. *Optics Letters*, 45(12):3337–3339, 2020. (Cited on pages 104 and 105.)

[184] Yasuhiro Matsui, Richard Schatz, Di Che, Ferdous Khan, Martin Kwakernaak, and Tsurugi Sudo. Isolator-free >67-ghz bandwidth dfb+r laser with suppressed chirp. In *Optical Fiber Communication Conference*, page Th4A.1. Optical Society of America, 2020. (Cited on pages 104 and 105.)

[185] Yasuhiro Matsui, Richard Schatz, Di Che, Ferdous Khan, Martin Kwakernaak, and Tsurugi Sudo. Low-chirp isolator-free 65-ghz-bandwidth directly modulated lasers. *Nature Photonics*, 15(1):59–63, 2021. (Cited on pages 104 and 105.)

[186] Nikolaos-Panteleimon Diamantopoulos, Hiroshi Yamazaki, Suguru Yamaoka, Munehiko Nagatani, Hidetaka Nishi, Hiromasa Tanobe, Ryo Nakao, Takuro Fujii, Koji Takeda, Takaaki Kakitsuka, et al. Net 321.24-gb/s imdd transmission based on a >100-ghz bandwidth directly-modulated laser. In *Optical Fiber Communication Conference*, page Th4C.1. Optical Society of America, 2020. (Cited on page 104.)

[187] Suguru Yamaoka, Nikolaos-Panteleimon Diamantopoulos, Hidetaka Nishi, Ryo Nakao, Takuro Fujii, Koji Takeda, Tatsurou Hiraki, Shigeru Kanazawa, Hiromasa Tanobe, Takaaki Kakitsuka, et al. 239.3-gbit/s net rate pam-4 transmission using directly modulated membrane lasers on high-thermal-conductivity sic. In *45th European Conference on Optical Communication (ECOC 2019)*, pages 1–4. IET, 2019. (Cited on page 104.)

[188] Jos JGM van der Tol, Yuqing Jiao, Jorn P Van Engelen, Vadim Pogoretskiy, Amir Abbas Kashi, and Kevin Williams. Inp membrane on silicon (imos) photonics. *IEEE Journal of Quantum Electronics*, 56(1):1–7, 2019. (Cited on page 105.)

[189] Michelle C Sherrott, Philip WC Hon, Katherine T Fountaine, Juan C Garcia, Samuel M Ponti, Victor W Brar, Luke A Sweatlock, and Harry A Atwater. Experimental demonstration of> 230 phase modulation in gate-tunable graphene–gold reconfigurable mid-infrared metasurfaces. *Nano letters*, 17(5):3027–3034, 2017. (Cited on page 106.)

[190] Yao-Wei Huang, Ho Wai Howard Lee, Ruzan Sokhoyan, Ragip A Pala, Krishnan Thyagarajan, Seunghoon Han, Din Ping Tsai, and Harry A Atwater. Gate-tunable conducting oxide metasurfaces. *Nano letters*, 16(9):5319–5325, 2016. (Cited on page 106.)

[191] Eyal Feigenbaum, Kenneth Diest, and Harry A Atwater. Unity-order index change in transparent conducting oxides at visible frequencies. *Nano letters*, 10(6):2111–2116, 2010. (Cited on page 106.)

[192] Shi-Qiang Li, Xuewu Xu, Rasna Maruthiyodan Veetil, Vytautas Valuckas, Ramón Paniagua-Domínguez, and Arseniy I Kuznetsov. Phase-only transmissive spatial light modulator based on tunable dielectric metasurface. *Science*, 364(6445):1087–1090, 2019. (Cited on page 106.)

[193] Ho-Seok Ee and Ritesh Agarwal. Tunable metasurface and flat optical zoom lens on a stretchable substrate. *Nano letters*, 16(4):2818–2823, 2016. (Cited on page 106.)

[194] Yu-Hsuan Kuo, Yong Kyu Lee, Yangsi Ge, Shen Ren, Jonathan E Roth, Theodore I Kamins, David AB Miller, and James S Harris. Strong quantum-confined stark effect in germanium quantum-well structures on silicon. *Nature*, 437(7063):1334–1336, 2005. (Cited on page 106.)

[195] Fei Ding, Yuanqing Yang, and Sergey I Bozhevolnyi. Dynamic metasurfaces using phase-change chalcogenides. *Advanced Optical Materials*, 7(14):1801709, 2019. (Cited on page 107.)

[196] Sajjad Abdollahramezani, Omid Hemmatyar, Hossein Taghinejad, Alex Krasnok, Yashar Kiarashinejad, Mohammadreza Zandehshahvar, Andrea Alù, and Ali Adibi. Tunable nanophotonics enabled by chalcogenide phase-change materials. *Nanophotonics*, 9(5):1189–1241, 2020. (Cited on page 107.)

[197] Tun Cao, Guangzhao Zheng, Shuai Wang, and Chenwei Wei. Ultrafast beam steering using gradient au-ge 2 sb 2 te 5-au plasmonic resonators. *Optics express*, 23(14):18029–18039, 2015. (Cited on page 107.)

[198] Yifei Wang, Patrick Landreman, David Schoen, Kye Okabe, Ann Marshall, Umberto Celano, H-S Philip Wong, Junghyun Park, and Mark L Brongersma. Electrical tuning of phase-change antennas and metasurfaces. *Nature Nanotechnology*, 16(6):667–672, 2021. (Cited on page 107.)

Acronyms

1G	First Generation
2G	Second Generation
3G	Third Generation
4G	Fourth Generation
5G	Fifth Generation
6G	Sixth Generation
2D	Two Dimensional
3D	Three Dimensional
AMP	Amplifier
AMPS	Advanced Mobile Phone Service
APD	Avalanche Photodiode
AWG	Arbitrary Waveform Generator
AWGR	Arrayed Waveguide Grating Router
BDMA	Beam Division Multiple Access
BER	Bit-error-ratio
BERT	Bit-error-ratio Tester
BS-ILC	Beam-steered Infrared Light Communication
CAA	Circular Antenna Array
CCC	Center Communication Controller
CCD	Charge-coupled Device
CDMA	Code Division Multiple Access
CDMA2000	Code Division Multiple Access 2000
CW	Continuous-wave
DBR	Distributed Bragg Reflector
DC	Direct Current
DL	Download Link
DFB	Distributed Feedback

DFB+R	Distributed Feedback+Reflection
DML	Directly Modulated Laser
DPO	Digital Phosphor Oscilloscope
DWDM	Dense Wavelength-division Multiplexing
EA	Electrical Amplifier
EBL	Electron Beam Lithography
ECL	External Cavity Laser
ECO-BPS	Electrically-controlled Optical Broadband Phase Shifter
EDFA	Erbium-Doped Fiber Amplifier
EDGE	Enhanced Data Rate for GSM Evolution
eMBB	Enhanced Mobile Broadband
EM	Electromagnetic
ES1	First Excited State
EVDO	Evolution-Data Optimized
FDMA	Frequency Division Multiple Access
FDTD	Finite-difference Time-domain
FBMC	Filter Band Multicarrier
GPRS	General Packet Radio Service
GS	Ground State
GSM	Global Systems for Mobil Communications
GSPM	Gap-surface Plasmon Metasurface
GST	Germanium (Ge)-antimony (Sb)-telluride (Te)
HSDPA	High Speed Downlink Packet Access
HSUPA	High Speed Uplink Packet Access
IM/DD	Intensity-modulation and Direct-detection
IMT	International Mobile Telecommunications
IoT	Internet-of-Things
IQ-MOD	In-phase/quadrature Modulator
IR	Infrared
KPI	Key Performance Indicator
LCPC	Liquid-crystal Polarization Controller
LED	Light-Emitting Diodes
Li-Fi	Light Fidelity
LTE	Long Term Evolution
LTEA	Long Term Evolution Advanced
MAC	Medium Access Control
MD	mobile device
MEMS	Micro-electrical Mechanical System
MIMO	Multiple-Input Multiple-Output

MLL	Mode-locked Laser
mMTC	Massive Machine Type Communications
MQW	Multiple-quantum-well
MU-MIMO	Multi-user Multiple-Input Multiple-Output
MW	Microwave Signal
MZ-a	Mach-Zehnder Modulator-a
MZ-b	Mach-Zehnder Modulator-b
MZ-c	Mach-Zehnder Modulator-c
MZM	Mach-Zehnder Modulator
ND	Neutral-density
OAM	Orbital Angular Momentum
OBTB	Optical Back-to-back
OFDMA	Orthogonal Frequency Division Multiple Access
OOK	On-off Keying
OSNR	Optical Signal-to-noise Ratio
OTF	Optical Tunable Filter
OTTD	Optical True-Time Delay
OWC	Optical Wireless Communication
OXC	Optical Crossconnect
PAM	Pulse Amplitude Modulation
PC	Polarization Controller
PCM	Phase Change Material
PD	Photodiode
PECVD	Plasma-enhanced Chemical Vapor Deposition
PIN	p-i-n Diode
PL	Photoluminescence
PML	Perfectly Matched Layer
P-MZM	Parallel Mach-Zehnder Modulator
POF	Plastic Optical fiber
PRA	Pencil-radiating Antenna
PS-in	Phase Shifter-in
PS-out	Phase Shifter-out
QD	Quantum Dot
RBW	Resolution Bandwidth
RF	Radio Frequency
RF-OAM	Radio-frequency Orbital Angular Momentum
RG	Residential Gateway
RoF	Radio-over-fiber
RIN	Relative Intensity Noise

SA	Saturable Absorber
SAM	Spin Angular Momentum
SC-FDMA	Single Carier Frequency Division Multiple Access
SDMA	Spatial Division Multiple Access
SEM	Scanning Electron Microscope
SLM	Spatial Light Modulator
SMF	Single-mode fiber
SOFDMA	Scalable Orthogonal Frequency Division Multiple Access
SPP	Spiral Phase Plate
SU-MIMO	Single-user Multiple-Input Multiple-Output
TDMA	Time Division Multiple Access
TEM	Transmission Electron Microscopy
TE	Transverse Electric
TIA	Transimpedance Amplifier
TLS	Tunable Laser Source
TM	Transverse Magnetic
UHD	Ultra-high-definition
UL	Upload Link
UMTS	Universal Mobile Telecommunications Systems
URLLC	Ultra-reliable and Low Latency Communications
VAN	Vector Network Analyzer
VBW	Video Bandwidth
VLC	Visible Light Communication
VR	Virtual Reality
WCDMA	Wideband Code Division Multiple Access
Wi-Fi	Wireless Fidelity
WIMAX	Worldwide Interoperability for Microwave Access
WLAN	Wireless Local Area Network
WRC	World Radio Communication

Acknowledgments

On September 14, 2017, I left my homeland and started to pursue a Ph.D. degree at Eindhoven University of Technology (TU/e). Now the end of this journey is close. It's been a long road getting from there to here. After going through all the confusion, challenges, efforts, and success, I would like to write my sincerest thanks at the end of my book, to everyone who lit up this road.

My first promoter Prof. Ton Koonen and co-promoter Dr. Zizheng Cao offered me the opportunity to start Ph.D. research. Here is my sincerest appreciation for their kindly supports. The positive encouragement and patient guidance from Prof. Koonen gave me confidence and motivated me in my research. Dr. Zizheng Cao is not only my daily supervisor but also my friend. He gives me constant support in both work and life. We also share happiness and sorrows. I also highly appreciate the contributions of the doctoral committee. Thanks to all the committee members Prof.dr. H. Liu (University College London), Prof.dr. O. Hess (Imperial College London), Prof.dr.ir. P.G.M. Baltus, Dr. J.J.G.M. van der Tol, Dr. A. González Curto, and the reserved member Dr. R. Stabile for their valuable suggestions/comments for improving this thesis. I would like to thank China Scholarship Council for providing financial support to my doctoral life.

I have spent a considerable amount of time doing nano-fabrication in the cleanroom of TU/e. The help, training, guidance, and suggestions from cleanroom technicians Erik Jan Geluk, Tjibbe de Vries, Barry E. Smalbrugge, Patrick Bax, and René van Veldhoven made my process run smoothly. Here is my sincere gratitude for their contributions. During my fabrication process, I frequently discussed the encountered process problems with my colleague and friend Yu Lei. Our discussions inspired me with creative ideas and solutions.

I want to express my appreciation to Dr. Chao Li, Dr. Mingyang Zhao, and Dr. Lei Zhu, from whom I gained huge knowledge about optical device measurement and transmission experiments. During their visit to TU/e as visiting scholars, we spent a lot of time in the laboratory and obtained fruitful research results. I also would like to thank Dr. Siming Chen and Shujie Pan, who are outstanding researchers from University College London. From them, I gained a lot of knowledge on semiconductor lasers. Our joint research on quantum dot mode-locked frequency comb produced nice results.

My sincere gratitude goes to all the members of Electro-Optical Communication (ECO) group. It's my honor to work with these brilliant colleagues. I would like to express my special appreciation to Mrs. José Hakkens, the secretary of our ECO group. She has provided me with countless help during my study.

During these years in Eindhoven, there has been a lot of happy moments spent with my friends. I would like to thank Ye Tian, Dr. Xuebing Zhang, Xinran Zhao, Liuyan Chen, Xinyang Lu, Dr. Wang Miao, Lu Huang, Dr. Chenhui Li, Dr. Teng Li, Dr. Yu Zhao, Dr. Bin Chen, Dr. Yi Lei, Dr. Zizheng Cao, Dr. Fulong Yan, Dr. Fu Wang, Dr. Bitao Pan, Dr. Xiaotao Guo, Shaojuan Zhang, Yu Lei, Pan Gao and many others, not only for your accompany but also for your help in both work and life. The happy times we spent playing, working, and traveling will be a precious part of my life.

The COVID-19 has cast a shadow over my life for the past two years, which caused troubles in managing my Ph.D. progress. My sincerest gratitude to my promoters, doctoral committee members, colleagues, and friends. Your kind support lifted me out of depression.

The last lines are my unique and deepest gratitude to my loving parents and girlfriend. The unconditional love and support from my parents are always core power for me to move forward. The warmest love and accompany from my girlfriend Fan Yang (and her lovely cats) paint my world colorful in years gone by.

JIANOU HUANG
Eindhoven, February 2022

Curriculum Vitae

Jianou Huang started working towards the Ph.D. degree at the Technische Universiteit Eindhoven (Eindhoven University of Technology, TU/e) in September 2017. He received his B. Eng. degree in Communication Engineering from Beijing University of Posts and Telecommunications in Beijing, China (2014). He received his M. Eng. degree in Information and Communication Engineering from Beijing University of Posts and Telecommunications in Beijing, China (2017). During his master's study, he has been working for one year in millimeter-wave phase shifter design from the Institute of Microelectronics, Chinese Academy of Sciences, Beijing, China. He has also been working for three months (as a visiting student) in microwave orbital angular momentum modes multiplexing/demultiplexing system from Institute for Photonic Integration, Eindhoven University of Technology, Eindhoven, The Netherlands. He is currently pursuing a Ph.D. degree with the Electro-Optical Communications Group, TU/e. His research interests include optoelectronic devices, microwave photonics, optical metasurfaces, and optical wireless communication.

List of Publications

JIANOU HUANG has the following publications:

Journal papers

- **J. Huang**, C. Li, Y. Lei, L. Yang, Y. Xiang, A. Curto, Z. Li, L. Guo, Z. Cao, Y. Hao, and A. M. J. Koonen, "A 20-Gbps Beam-Steered Infrared Wireless Link Enabled by a Passively Field-Programmable Metasurface", Wiley Laser & Photonics Reviews, 15 (1), pp. 2000266 (2021).

- **J. Huang**, Z. Cao, X. Zhao, X. Zhang, Y. Liu, Y. Xiang, G. Gerini, A.M.J. Koonen, "Optical generation/detection of broadband microwave orbital angular momentum modes", IEEE Journal of Lightwave Technology, 38 (6), pp. 1202-1209 (2020).

- S. Pan+, **J. Huang+**, Z. Zhou, Z. Liu, L. Ponnampalam, Z. Liu, M. Tang, M. Lo, Z. Cao, K. Nishi, K. Takemasa, M. Sugawara, R. Penty, I. White, A. Seeds, H. Liu, and S. Chen, "Quantum dot mode-locked frequency comb with ultra-stable 25.5 GHz spacing between 20°C and 120°C", Photonics Research, 8 (12), pp. 1937-1942 (2020). (Co-firstauthor)

- **J. Huang**, C. Li, R. Lu, L. Li, and Z. Cao, "Beyond the 100 Gbaud directly modulated laser for short reach applications", IOP Journal of Semiconductors, 42 (4), pp. 041306 (2021).

- H. Zheng, K. Wu, B. Chen, **J. Huang**, Y. Lei, C. Li, A. Balatsoukas-Stimming, Z. Cao, and A.M.J Koonen, "Experimental demonstration of 9.6 Gbit/s polar coded infrared light communication system", IEEE Photonics Technology Letters, 32 (24), pp. 1539-1542 (2020).

Conference contributions

- **J. Huang**, Q. Wang, Z. Li and L. Yang, "Novel method for millimeter wave phase shifter design using loaded transmission line", 2016 Asia-Pacific Microwave Conference (APMC), pp. 1-4 (2016).

- L. Yang, Q. Wang, W. Wei and **J. Huang**, "Resource Scheduling for Content Downloading Network with D2D Support", 2016 IEEE 84th Vehicular Technology Conference (VTC-Fall), pp. 1-5 (2016).

Patents

- Switch-type microstrip phase shifter and the corresponding phase shift module, 201510854451.6, PCT/CN2015/095983, Zhiqiang Li, **Jianou Huang**, Haiying Zhang.